Photo-responsive Liquid Crystal Block Copolymers

by

Michael Thomas Petr

Bachelor of Science in Chemical Engineering

Iowa State University of Science and Technology, Ames, Iowa, 2003

Doctor of Philosophy in Chemical Engineering

at the

MASSACHUSETTS INSTITUTE OF TECHNOLOGY

June, 2012

Author: _____
Chemical Engineering
March 22, 2012

Certified by: _____
Paula T. Hammond, Professor
Thesis Supervisor

Accepted by: _____
Professor William M. Dean
Chairman, Departmental Committee on Graduate Students

Photo-responsive Liquid Crystal Block Copolymers

by

Michael Thomas Petr

Submitted to the Department of Chemical Engineering on March 22, 2012 in partial fulfillment

of the requirements for the degree of

Doctor of Philosophy in Chemical Engineering

Abstract

Photo-responsive liquid crystal polymers (LCP) which contain azobenzene moieties have gained interest for their ability to change properties by merely irradiating them with the correct wavelength of light in the appropriate temperature range. Furthermore, they have been crosslinked for elasticity and to translate this property change into photo-mechanical actuation, such as contraction, expansion, bending, or oscillation. However, a major drawback and hindrance to their actual use as actuators has been their need for elevated temperatures and their slow responses at room temperature.

The work described in this thesis addresses this problem, and its solution has an impact on the field of functional elastomers in general. To produce a fast photo-response at room temperature, a new photo-responsive azobenzene nematic side chain (SC) LC polysiloxane was developed, characterized, and demonstrated to respond significantly, and reversibly from 0-50°C, which is the ambient temperature range in which we live, through its photo-induced nematic to isotropic transition. In particular, its nematic phase almost totally disappeared in 35 s, and its modulus decreased up to 35% in about 10 s. To turn this photo-response into photo-actuation, polystyrene (PS) end blocks were added to the poly(vinylmethylsiloxane) (PVMS) to produce PS-b-PVMS-b-PS, which is important in and of itself because the PVMS has a very low T_g and a functionalizable backbone and the PS end blocks make the material a thermoplastic elastomer. After attachment of the azobenzene LC, the resulting photo-responsive thermoplastic elastomer reversibly contracted 3.3% against 25.7 kPa of stress in about 6 s.

Thesis Supervisor: Paula T. Hammond
Title: Executive Officer, Chemical Engineering
David H. Koch Professor in Engineering
Associate Editor, ACS Nano

Acknowledgements

My time here at MIT and in Boston has been extremely enjoyable and fulfilling, and I will look back on it with fond memories. The research was fun and interesting, yes, but it is mostly because of all the people that I have had the privilege of knowing, working with, hanging out with, and making friends with. It is to all these people that have helped me along the way, that I would like say thank you.

There were a number of faculty and staff that have facilitated my research and my education throughout the years. First and foremost, I would like to thank Professor Paula Hammond, who has been everything I could I have hoped for in an advisor and more. We all know about her excellent research, but it is her positive, friendly attitude and her ethical research habits that set her apart. Second, I would like to thank Professors Brad Olsen, Alan Hatton, and Tim Swager on my Thesis Committee, who have given me numerous useful suggestions and feedback about my research. Third, I would like to thank Professors Brad Olsen and George Stephanopoulos who made my semester as a TA very satisfying. Fourth, I would like to thank the many staff members of both the Chemical Engineering Department and the Institute for Soldier Nanotechnologies (ISN), especially Steve Kooi, Bill DiNatale, Donna Johnson, Maureen Caulfield, Marlisha McDaniels, Christine Preston, Suzanne Maguire, and Katie Lewis. Finally, I would like to thank all my teachers and advisors before MIT, especially Mr. Oberley, Mr. Van Sickle, Ms. Raglin, Mrs. Ferraro, Dr. Andy Hillier, Dr. Alessandro Butté, and Dr. Francis Gadala-Maria.

Along with the faculty and staff, there have been numerous students and postdocs that I have been fortunate enough to work with and to call my friends. First, I would like to thank Eric Verploegen, who left me with a fun project and ensured that I had the skills to continue it.

Second, I would like to thank Bati Katzman, who was my faithful and cheerful UROP for over a year. Third, I would like to thank all those who have helped me with experiments, especially Matt Helgeson, Johannes Soulages, Sarah Bates, Shuang Liu, and Bill DiNatale. Third, I would like to thank all the past and present members of the Hammond group and the ISN, especially Amanda Engler, Zhiyong Poon, Josh Moskowitz, Jason Kovacs, Becky Ladewski, Kevin Huang, Anita Shukla, Kevin Krogman, Jung-Ah Lee, Ryan Waletzko, Xiaoyong Zhao, Dan Bonner, Wei Li, Grinia Nogueira, Abby Oelker, Megan O'Grady, Steven Castleberry, Kittipong Saetia, Caroline Chopko, Jason Cox, Ryan Mozlin, Derek Schipper, and John Goods.

There have also been some important people outside of academics. First, I would like to thank all the kids from UP and POSTUP, which quickly became my weekly vacation from the stresses of grad student life, especially Craig Bonnoit, Ankur Moitra, Matt Johnston, Julio Nanni, Drew Potter, Zenzi Brooks, Obi Ohia, Alan Benson, Matt Edwards, Guner Celik, Robin Chisnell, Charles Lin, Jamie Teherani, Ronen Mukamel, Dillon Gardner, and Matt Walker. Second, I would like to thank the Young Adult Group at St. Clements, which has been my Boston family, especially, Mike Procanik, Shane Coombs, Nicole Lavery, Lori Holt, Sean Holt, Becca Hofmann, Marcus Ng, Christine Nguyen, Dominik Rabiej, Peter Spilka, Rosa Spilka, Joe Papp, Emilie Berzin, Joey Goerge, Andrew Finn, Jennifer Hofmann, Geoff King, Paul Fathallah, Sebastian Tong, Brandon Hingel, John Keck, Chris Pham, Kara Waxman, Keeley Wray, Justin Quattrini, and Andrea Quattrini.

To finish, my family deserves a great deal of credit. First, I would like to thank my parents Don and Kathy, who were truly my first teachers and who have supported me and my education throughout my entire life. Second, I would like to thank my brother Brian, who has been a good companion at home and has always helped me in whatever way I needed. Third, I

would like to thank my in-laws the Gomezes, Titus, Adele, Simon, Michelynne, Valentine, Alwyn, Ryan, and Clare, who have welcomed me into their family. Most importantly, I would like to thank my beautiful wife Geraldine for all her love and support throughout my Ph.D. I enjoy research, but she makes me happy.

Table of Contents

Abstract 3

Acknowledgements 4

List of Figures 9

List of Tables 13

1. Introduction 14

    1.1. Liquid Crystals 14

    1.2. Block Copolymers 17

    1.3. Liquid Crystal Polymers (LCP) 20

    1.4. Photo-responsive Liquid Crystal Polymers 21

    1.5. Summary of Relevant Previous Research 22

    1.6. Motivation for Thesis 23

    1.7. Overview of Thesis Goals and Research 24

2. Synthetic Methods 24

    2.1. Synthetic Scheme 24

    2.2. LC Synthesis 28

    2.3. PVMS Synthesis (5) 36

    2.4. PS-PVMS-PS Triblock Copolymer (7) Synthesis 37

    2.5. LC Attachment 45

3. Photo-responsive LCP Characterization 50

3.1. Instrumentation 50
3.2. SCLCP properties and characterization. 50
3.3. Photo-responsive characterization 58
4. Oscillatory Shear Rheometry of LCP 65
4.1. Experimental 65
4.2. Oscillatory Shear Rheometry Conditions 66
4.3. Linear Viscoelastic Strain Regime Determination 67
4.4. Thermal and Temporal Characterization 70
4.5. UV Modulus Switching 78
5. Photo-responsive Liquid Crystal Triblock Copolymer Characterization 84
5.1. Instrumentation 84
5.2. Material Design 84
5.3. PS-PVMS-PS TBCP Characterization 86
5.4. Liquid Crystal Triblock Copolymer Characterization 90
5.5. Photo-responsive Thermoplastic Elastomer Actuation 95
6. Conclusion 99
6.1. Summary of Thesis Contributions 99
6.2. Suggested Future Work 99
6.3. References 100

List of Figures

Figure 1-1. Schematic of a calamitic LC. a) is an isotropic liquid, b) is a nematic LC, and c) is a smectic LC.[8] 14

Figure 1-2. POM experimental apparatus.[10] 16

Figure 1-3. Schematic of a block copolymer and its possible ordered or disordered morphologies.[11] 18

Figure 1-4. Range of block copolymer morphologies. a) is a qualitative schematic, and b) is a semi-quantitative plot of the morphologies in the XN and volume fraction space.[13] .. 19

Figure 2-1. Synthesis of new photo-responsive SCLCP. 26

Figure 2-2. LC attachment to PS-PVMS-PS TBCP. 27

Figure 2-3. ^{1}H NMR spectrum for 1. 30

Figure 2-4. ^{1}H NMR spectrum for 2. 32

Figure 2-5. ^{1}H NMR spectrum for 3. 34

Figure 2-6. ^{1}H NMR spectrum for 4. 35

Figure 2-7. ^{1}H NMR of PVMS (5). 37

Figure 2-8. PS-PVMS-PS synthetic scheme. 40

Figure 2-9. MW traces from the GPC of the PS-PVMS-PS synthetic steps. 43

Figure 2-10. ^{1}H NMR sprectrum of the PS-PVMS-PS TBCP. 44

Figure 2-11. ^{1}H NMR spectrum for 6. 46

Figure 2-12. ^{1}H NMR spectrum for 8. 48

Figure 2-13. MW traces from the GPC of the LC attachment to the PS-PVMS-PS TBCP. 49

Figure 3-1. Differential Scanning Calorimetry (DSC) at 10 °C/min with 2 cycles on SCLCP 1 week after annealing. 52

Figure 3-2. Small Angle X-ray Scattering (SAXS) diffractogram of crystalline and nematic samples of SCLCP 53

Figure 3-3. Gaussian model of the LCP. Gray is carbon, white is hydrogen, red is oxygen, blue is nitrogen, and blue-gray is silicon. The model is actually a very similar analog of the LCP because there is merely an Si-O single pond as opposed to a polymeric Si-O.... 54

Figure 3-4. Medium Angle X-ray Scattering (MAXS) diffractogram of nematic SCLCP. 55

Figure 3-5. Polarizing Optical Microscopy (POM) image of SCLCP at a magnification of x50 showing a Schlieren texture with 2- and 3-point disclinations. 56

Figure 3-6 Real part of the complex ellipsometric ratio (ρ) fit with the parameters in Table 3-1.57

Figure 3-7. UV-Visible absorbance spectrum. 58

Figure 3-8. *Trans* to *cis* conformation change resulting in the nematic to isotropic phase change. 59

Figure 3-9. Medium Angle X-ray Scattering (MAXS) diffractogram of nematic SCLCP with UV off and UV on..... 60

Figure 3-10. Polarizing Optical Microscopy (POM) at a magnification of x50 of SCLCP with UV irradiation. The first picture was taken before the UV light was turned on, and it shows a nematic Schlieren texture with 2-, 3-, and 4-point disclinations. The next pictures are from 5-30 s and show the nematic phase disappearing, and the last picture is at 35 s and shows the nematic phase almost completely gone. 63

Figure 3-11. Integrated color intensity from Polarizing Optical Microscopy (POM) images. The first portion has a rate of 1.0×10^7 intensity/s and a linear r^2 of 0.9995, and the second portion has an exponential time constant of 4.6 s and an r^2 of 0.998..... 64

Figure 4-1. Schematic of rheometry experimental apparatus. 66

Figure 4-2. Amplitude sweeps with both UV off and UV on at 10 rad/s and a) 50ºC, b) 25ºC,† c) 5ºC, and d) 0ºC. In a), the G" values for UV off are covered by those for UV on because they are very close. 68

Figure 4-3. Lissajous Plots for both UV off and UV on at 10 rad/s and a) 50ºC, b) 25ºC, c) 5ºC, and d) 0ºC. The elliptic forms in all of the plots are evidence that the material is in the LVE strain regime. 70

Figure 4-4. Temperature sweeps with both UV off and UV on at 5°C/min, 10 rad/s, and 1% commanded strain a) from 80ºC to -5ºC and b) zoomed in from 25ºC to -5ºC. 72

Figure 4-5. Frequency sweeps with both UV off and UV on in the LVE strain regime at a) 50ºC, b) 25ºC, c) 5ºC, and d) 0ºC. Both G' and G" in a) and b) were fit individually with the power law in Equation 4-1, the parameters for which are in Table 4-1. 74

Figure 4-6. Time-temperature superposition of frequency sweeps shifted by eye to 25°C. Each of the four temperatures has a different symbol. 76

Figure 4-7. Shift factors from time-temperature superposition of frequency sweeps fit with the WLF equation in Equation 4-2. 77

Figure 4-8. Time sweeps with UV modulus switching in the LVE strain regime at 10 rad/s and a) 60ºC, b) 50ºC, c) 25ºC, d) 5ºC, e) 0ºC, and f) -5ºC. The UV light was off at 0 seconds and successively switched on and and off again. Blue arrows indicate when the UV light was turned on, and black arrows indicated when the UV light was turned back off. 79

Figure 4-9. Stretched exponential a) τ and b) n parameter values from fitting of moduli cycles in UV switching experiments using . τ_{on} and n_{on} correspond to the modulii drops when

the UV light was turned on, and τ_{off} and n_{off} correspond to the moduli recoveries when the UV light was turned back off. The points have been connected to aid the eye. 82

Figure 4-10. Average τ's calculated from stretched exponential fitting of moduli cycles in UV switching experiments. 83

Figure 5-1. Schematic of aligned LC domains that stretch the polymer backbone and contraction of the backbone in response to UV light due to disruption of the LC phase. 86

Figure 5-2. TEM images of the PS-PVMS-PS TBCP lamellar morphology. The dark regions are PVMS, and the light regions are PS. Also, the 100 nm scale is marked, and the large curved lines are the edge of the carbon support. 87

Figure 5-3. Small Angle X-ray Scattering (SAXS) diffactorgram of PS-PVMS-PS TBCP. The large first peak corresponds to the 27.5 nm lamellar spacing, and the other marked peaks are 2nd and 3rd reflections. 88

Figure 5-4. Differential Scanning Calorimetry (DSC) at 10°C/min of PS-PVMS-PS. The cooling cycle has been shifted up 0.3 W/g for viewing convenience. 89

Figure 5-5. Dynamic Mechanical Analysis (DMA) at 3 °C/min, 10 Hz, and 0.1% strain amplitude of a 18.7x8.8x0.6 mm annealed strip of TBCP. 90

Figure 5-6. Transmission Electron Microscopy (TEM) images of the LC-TBCP spherical morphology. The dark regions are LC-PVMS, and the light regions are PS. Also, the 100 nm scale is marked, and the large curved lines are the edge of the carbon support. 91

Figure 5-7. Small Angle X-ray Scattering (SAXS) diffactorgram of the LC-BCP. The large peak corresponds to the 40.6 nm spherical spacing. 92

Figure 5-8. Differential Scanning Calorimetry (DSC) at 10°C/min of LC-TBCP. The cooling cycle has been shifted up 0.35 W/g for viewing convenience. 93
Figure 5-9. Polarized Optical Microscopy (POM) images of the LC-TBCP at a magnification of x10 at a) 100°C and b) 120°C. 94
Figure 5-10. Dynamic Mechanical Analysis (DMA) at 3 °C/min, 10 Hz, and 0.1% strain amplitude of a 10.8x7.6x1.7 mm annealed strip of LC-TBCP. 95
Figure 5-11. UV contraction of a stretched 11.6x6.8x0.0629 mm strip of LC-TBCP against a 11 mN force supplied by the DMA instrument. Blue arrows indicate times when the UV light was switched on, and black arrows indicate times when the UV light was switched off. The UV on switches were fit with lag time followed by a stretched exponential producing average τ_{lag}, τ, n, τ_{avg} , and contraction percent values of 3.9 s, 2.1 s, 1.14, 2.0 s, and 3.3%, respecitively. 97
Figure 5-12. Picture of LC-TBCP after use in photo-contraction experiments. 98

List of Tables

Table 2-1. MW and PDI of all the steps in the PS-PVMS-PS polymerization. [a] denotes GPC data, and [b] denotes ^{1}H NMR data. 44
Table 2-2. MW and PDI of the LC attachment to the PS-PVMS-PS TBCP. [a] denotes GPC data, and [b] denotes ^{1}H NMR data. 49
Table 3-1. Fit parameters from ellipsometry data. 57
Table 4-1. G' and G" power law fit parameters for 50°C and 25°C. 75
Table 4-2. WLF parameters at 25°C from fitting of shift factors in Fig. 5 and WLF parameters translated to T_g. 77

Introduction

1.1. Liquid Crystals

Liquid crystals (LC) are molecules with order in 1 or 2 dimensions but not 0, like a liquid, or 3, like a solid. Therefore, they are a state of matter between a liquid and a crystalline solid with varying amounts of order. To gain this order, they tend to have a high aspect ratio, such as calamitic, or rod-like, LC's, which is the type in this work. Figure 0-1 shows a schematic of a calamitic LC. The molecules are long and rod-like, so they tend to line up in the liquid state to reduce free volume. At high enough temperatures, the material is a regular isotropic liquid, as in Figure 0-1a. At a given temperature, the isotropization temperature (T_{iso}), clearing temperature (T_{cl}), or nematic to isotropic transition temperature (T_{NI}), the molecules start generally to line up in a particular direction, the director ($\vec{n}$), but they have no positional order, as in Figure 0-1b. At a lower given temperature, the smectic to isotropic transition temperature (T_{Sm}), smectic to nematic transition temperature (T_{SmN}), or T_{iso}, the molecules line up even more, plus they stack in lamellae with a characteristic spacing that is the length of the LC, as in Figure 0-1c. LC's can exhibit any or all of these phases as well as a host of others.[1-7]

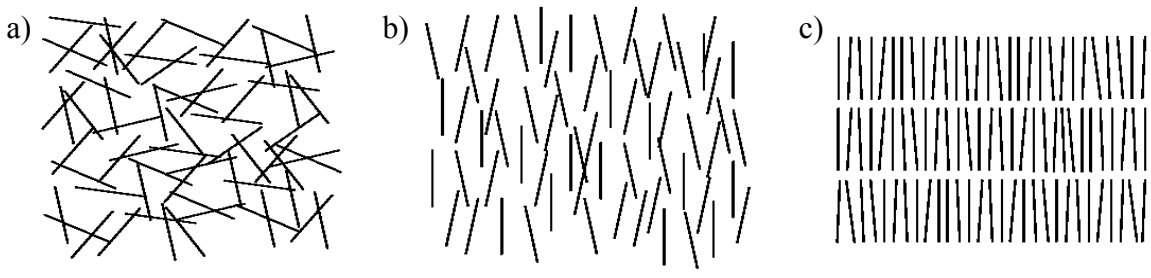

Figure 0-1. Schematic of a calamitic LC. a) is an isotropic liquid, b) is a nematic LC, and c) is a smectic LC.[8]

When it comes to LC's, there is a quantitative measure of order, the order parameter (S). It is defined as the average of the 2nd Legendre polynomial of each individual LC's deviation from the local LC director, shown in Equation 0-1.

$$S = \left\langle \frac{3\cos^2 \theta - 1}{2} \right\rangle \qquad 0\text{-}1$$

where θ is the angle between each individual LC molecule and the local order director in the material. 0 signifies no order, such as in an isotropic liquid, and 1 signifies perfect order, as in a crystalline solid. Most nematic LC's have S values between 0.3 and 0.8, and most smectic LC's have order parameters around 0.9.[3]

There is another property that is important to the characterization of LC's, and that is birefringence. Birefringence (Δn) is the difference between the directionally dependent refractive indices (n) in a material. In LC's, birefringence arises from the differences in properties between the parallel and perpendicular directions with respect to $\vec{n}$ within the LC phase. In particular, birefringence is useful in Polarized Optical Microscopy (POM), where the sample of interest is flanked by perpendicular polarizers within the light path of the microscope, as shown in Figure 0-2. Linearly polarized light leaves the first polarizer, passes through the sample, and either passes through the second polarizer to be seen, or is blocked by the second polarizer. If the sample is isotropic, such as a liquid or an isotropic crystal, the light that passes remains linearly polarized and is, therefore, blocked by the second perpendicular polarizer. If, however, the sample is birefringent, such as an LC with its $\vec{n}$ away from the optical axis, the linearly polarized light that enters the sample splits into a wave parallel to the polarization (ordinary) and perpendicular to the polarization (extraordinary) and then recombines outside the sample to produce circularly polarized light at an angle different that the original polarization. This

circularly polarized light can then pass through the second polarizer to be seen. In fact, it shows up as brightly colored, and the color depends on the thickness and the birefringence of the sample.[9]

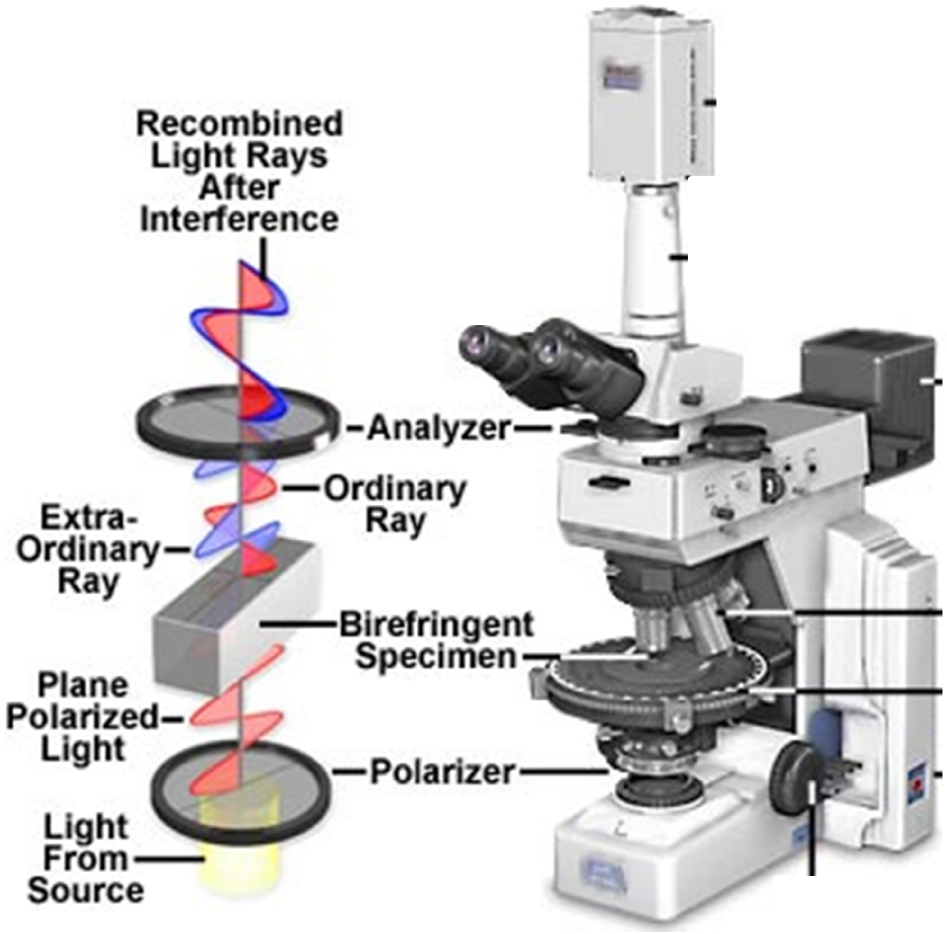

Figure 0-2. POM experimental apparatus.[10]

Furthermore, the image itself has significance. There are many patterns that can be formed, but the most common is the Schlieren texture, which has streaks of color intertwined with streaks of black. The streaks of color are from the birefringent LC phase, and the streaks of black are from where either the LC's $\vec{n}$ is parallel to the optical axis or the isotropic

discontinuities between the domains of LC with differing $\vec{n}$'s. These domains of differing $\vec{n}$ meet at points (disclinations), and, at the disclinations, different numbers of domains can meet. For a nematic LC, any number of domains can meet at a disclinations, but, for a smectic phase, four domains must meet at each disclination.

1.2. Block Copolymers

Block copolymers are polymers in which two or more different polymers are chemically linked. In general, polymers do not dissolve in one another, unless they are chemically very similar because the entropic driving force is mitigated by the lower amount of rotational and translational freedom in the polymers; therefore, mixtures of polymers tend to phase segregate. However, in the case of block copolymer, macroscopic phase segregation is impossible because the two polymers are linked. Phase segregation still does occur but on the length scale of the polymer, which is on the order of 50 nm as shown in Figure 0-3, because the different polymer segments cannot move any farther away due to their chemical connection. As with most other condensed phases, this ordered block copolymer morphology can be disordered by heating through the order-disorder transition temperature (T_{ODT}) whereby the polymers gain enough energy to dissolve into one another. This process is reversible and is dependent upon the chemistry of the two polymers as well as their molecular weights.[11-14]

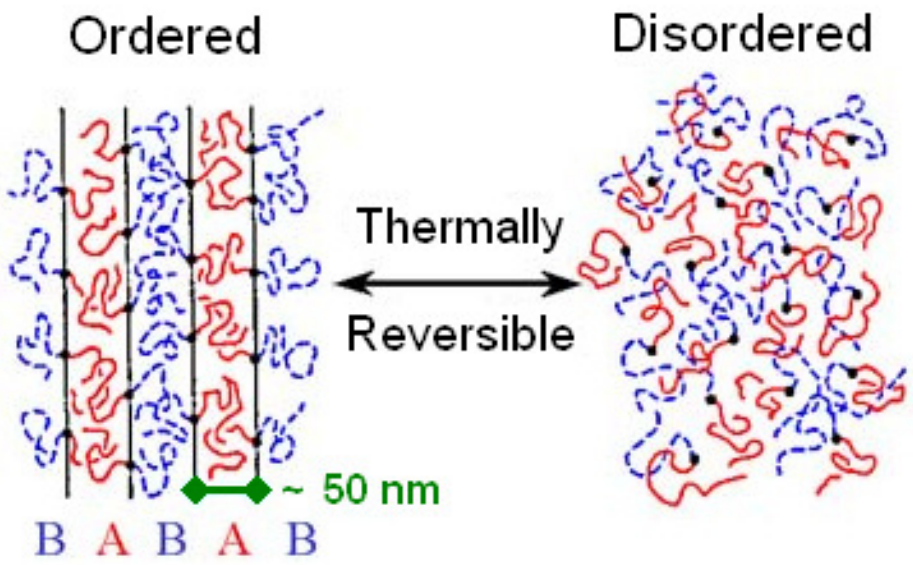

Figure 0-3. Schematic of a block copolymer and its possible ordered or disordered morphologies.[11]

Not only does the polymers' chemistries and molecular weights affect the order-disorder transition, but they also affect the morphology of the ordered phase. Figure 0-4 shows the possible block copolymer morphologies and outlines these effects. Qualitatively in Figure 0-4a, there is a yellow block and a red block in the copolymer. Starting at the left, there is a little yellow and the rest red, which forms yellow body-centered cubic (BCC) spheres in a red matrix. More yellow forms yellow hexagonally packed cylinders (HEX) in a red matrix. A little more yellow forms a yellow bicontinuous gyroidal phase still in a red matrix. Finally, when the amounts of the two blocks are roughly equal, a lamellar phase forms. As Figure 0-4a continues to the right, more yellow is added and all the morphologies reverse with red in a yellow matrix. Quantitatively, the conditions under which these various morphologies form have been studied, and Figure 0-4b summarizes the findings. It plots the regions where each morphology forms against XN, which is the thermodynamic driving force for phase separation, and f_A, which is the relative volume fraction of the two blocks. X is the Flory-Huggins interaction parameter, which

is a measure of how chemically dissimilar the two polymers are, and it decreases with temperature. N is the degree of polymerization of the block copolymer; the longer the polymers, the larger driving force they have for phase separation. Last but not least, the effect of f_A is the most intuitive because it follows from the qualitative observations in Figure 0-4a. If the amount of the two polymers are equal, they will form a lamellar phase; otherwise, the smaller polymer will order within a matrix of the larger one.[11-14]

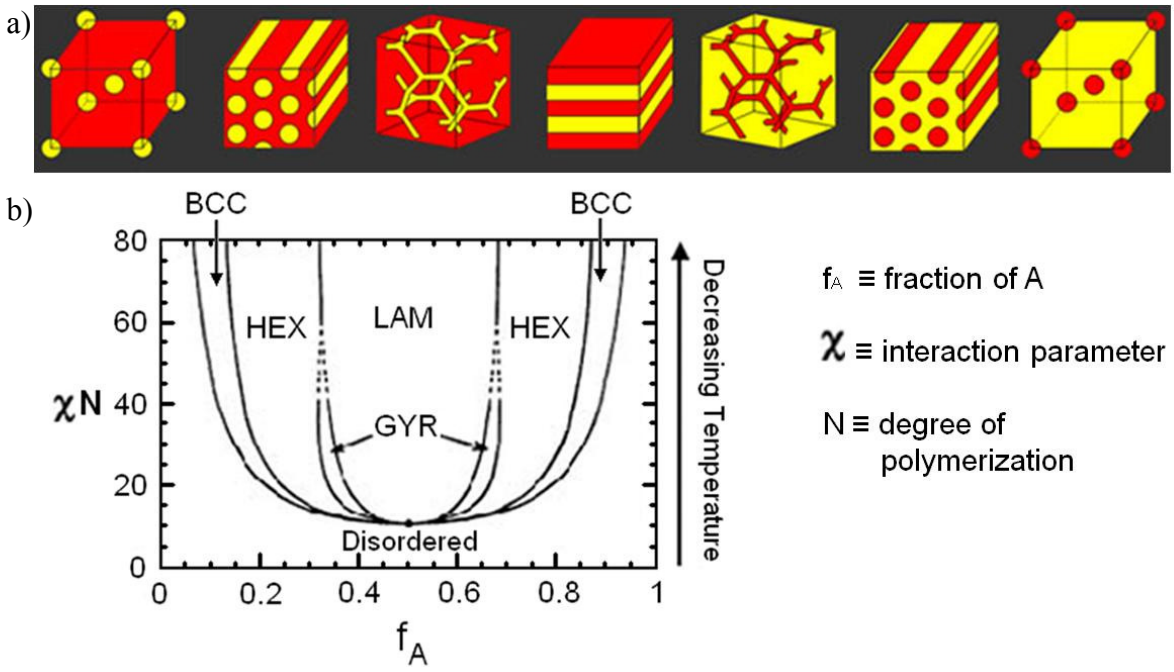

Figure 0-4. Range of block copolymer morphologies. a) is a qualitative schematic, and b) is a semi-quantitative plot of the morphologies in the XN and volume fraction space.[13]

One important application of block copolymers is in the production of thermoplastic elastomers. Elastomers are soft crosslinked materials which can reversibly experience large strains. Classically, they are chemically crosslinked low T_g polymers, such as natural rubber, but there are other possibilities. In particular, an ABA triblock copolymer (TBCP) can form an

elastomer, if the A block is hard, ie. its T_g is well above room temperature, and the B block is soft, ie. its T_g is well below room temperature. In such a material, the B block is soft as normal, and the A blocks act as physical crosslinks to tie the material together. Still, if it is heated past the A block's T_g, then the whole material can soften and be reformed, thus producing a thermoplastic elastomer.[11-14]

1.3. Liquid Crystal Polymers (LCP)

Liquid crystal polymers (LCP) are the combination of liquid crystals and polymers to produce new materials with the properties of LC's and the benefits of polymer systems. Because of their unique advantages, they have been studied for decades, and a number of important aspects have arisen. When designing a side chain liquid crystalline polymer (SCLCP), there are three main structural components to consider: the LC side group, the polymeric backbone, and the linker group or functional group by which the two are attached to one another. The polymer can be from any number of backbone categories, including vinyl,[15-17] methacrylate,[15, 18-22] a strained cycloalkene product of Ring Opening Metathesis Polymerization (ROMP),[23-25] or even a dendrimer.[26] In particular, low glass transition temperature (T_g) polysiloxane backbones are important because they are flexible and do not constrain the ordering of the attached LC's; when functionalized with LC's, they are generally not glassy at room temperature, enabling the exhibition of LC phases at ambient conditions.[27-48] The LC can also be selected to exhibit numerous phases, with the most common being smectic [16, 18-23, 25, 49-51] or nematic [25, 52-55] with a high [18, 19, 23-25, 56] or low [17, 52, 57] isotropization temperature (T_{iso}). Finally, the LC can be attached "end-on" [15, 16, 18, 19, 21-24, 50, 51] or "side-on" [17, 53-55, 58, 59] with respect to the unit director of the LC.

1.4. Photo-responsive Liquid Crystal Polymers

More recently, photo-responsive SCLCP's have gained interest for their ability to change properties by merely irradiating them with the correct wavelength of light in the appropriate temperature range.[30, 43, 47, 52-54, 60-86] Photo-responsive materials can be formed from a variety of classes of molecules, including LCP's,[52, 54, 61, 63-65, 76, 79, 82-85, 87-101] low molecular weight LC's, polymers,[77, 102-110] chromophore doped polymers,[111] chromophore doped LC's,[112, 113] and chromophore doped LCP's,[104, 114-117] and they can be photo-responsive through a variety of chromophores, including derivatives of azobenzene,[52, 54, 61, 63-65, 76, 77, 79, 82-85, 87-101, 103, 105-107, 109-112, 114-118] spiropyran,[104, 113, 118, 119] fulgide,[112, 113, 118] diarylethene,[113] thioindigo,[112] and cinnamic acid.[108, 119-121]

Of particular interest are photo-responsive azobenzene LCPs, which are the most common of this class of materials.[52, 54, 61, 63-65, 76, 79, 82-85, 87-101] The azobenzene moiety is a robust, reliable, and reversible chromophore that is well understood, and can be used as part of the LC moiety of an LCP. The azobenzene LC provides the photo-responsive behavior, and the polymer provides structure and mechanical stability. They are of particular interest for applications in which a quick response or actuation [30, 47, 61, 63, 66, 70-73, 75, 76, 85, 86] is necessary, such as artificial muscles,[53, 54] photomechanical cantilevers,[65, 76, 80, 83] photomechanical oscillators,[84] and even robotics.[82]

Azobenzene SCLCP's are responsive to UV light by means of a *trans* to *cis* isomerization of the azobenzene moiety. The azobenzene starts in its thermodynamically stable *trans* conformation; then, absorption of a UV photon promotes an electron from the HOMO π-orbital to the LUMO π*-orbital, which switches the azobenzene to its *cis* conformation. In its *trans* conformation, azobenzene is straight and extended, and able to pack effectively with its

neighbors to form an LC phase; however, in its *cis* conformation, the azobenzene takes on a bent configuration and is no longer able to pack sufficiently to form an LC phase leading to the formation of an isotropic phase. This process is reversible and can be catalyzed by higher wavelengths of light as well as thermal energy because the *trans* conformation is thermodynamically favored.[122] Historically, this nematic formation has been the process used to study the phase change kinetics, and the nematic domains grow linearly with time when subject to a large enough temperature quench.[123-126] On the other hand, there have been few kinetic studies on the nematic to isotropic transition, though one simulation did predict a linear decrease in the order parameter with respect to time.[127]

1.5. Summary of Relevant Previous Research

By the process described above, quick, reversible, and large responses have been achieved in photo-responsive SCLCP's. This observation is notable in that rapid responses in the bulk have, thus far, only been achieved at elevated temperatures. For example, the nematic side-on azobenzene polymethacrylate made by Li required 25 minutes of irradiation at 2.3 mW/cm^2 and room temperature for an 80.5 nm film [52] or a couple of minutes of irradiation at 100 mW/cm^2 and 70ºC for a 20 μm film [54] for a complete response because the T_g of the polymer backbone was 60°C. A photo-responsive smectic end-on azobenzene polysiloxane system was made by Verploegen; however, in that case, the transitions were only observed at or above 100°C. This is because, although the T_g of the polymer was very low, the T_{iso} of the smectic phase was 126°C.[82] Below 100°C, the smectic phase was too viscous for a fast response. In fact, these two examples illustrate the importance of the T_g of the polymer backbone and the T_{iso} of the LC because they define the temperature range in which the bulk photo-responsive SCLCP

can be used. The T_g defines the absolute lower limit, and the T_{iso} defines the upper limit as well as a potential lower limit whereby, if it is too far below the T_{iso}, the LC becomes too viscous for a quick response.

There have been two approaches to circumvent this problem to obtain room temperature, rapid, and reversible photo-responses. The first is replacement of the azobenzene pendant group with a dissolved azobenzene chromophore. This technique has been used to prepare crosslinked nematic azobenzene polysiloxane thin films with response times ranging from milliseconds to seconds, depending on the UV irradiation intensity used.[114,115] A second approach involves complex alignment, mounting, and movement of the azobenzene LCP in conjunction with a high-powered polarized UV source. Using this method, thin films and cantilevers of aligned crosslinked nematic azobenzene polyacrylates have shown very fast response rates, although they require relatively large UV intensities[93,83,84]. However, these solutions are not practical under all circumstances. For example, in the first technique, the azobenzene moiety is no longer chemically linked, therefore requiring specific processing needs, and it cannot be used under conditions that interfere or change this processing. In the second technique, the T_g limitation was overcome by the use of a strong polarized UV laser and a complicated irradiation geometry and procedure.

1.6. Motivation for Thesis

As alluded to above, for photo-responsive LCP's to be generally useful, particularly as actuators, they need to be robust, rapid, and reversibly photo-responsive at room temperature because that is where most actuators are needed. There have been a limited number of solutions that solve this problem under certain conditions, but, for the field to move forward, there must be

a more general solution. For a robust material with a bulk response, an azobenzene LCP with a low T_g and a low T_{iso} is needed. This thesis describes such a material (during its course another material with such properties was also produced by another group [94]) as well as another improvement over current materials, which was to replace the chemical crosslinks of the current materials with the physical crosslinks of a TBCP thermoplastic elastomer. Therefore, the material is even easier to process.

1.7. Overview of Thesis Goals and Research

This thesis describes the synthesis and subsequent characterization of three new materials: a room temperature photo-responsive LCP, a polystyrene-b-poly(vinylmethylsiloxane)-b-polystyrene (PS-PVMS-PS) TBCP, and their combination, a room temperature photo-responsive LC-TBCP thermoplastic elastomer. The first material is the functional part, and it was used to fully characterize the photo-responsive behavior. The second material is useful because it is a thermoplastic elastomer with a very low T_g soft block and an easily functionalizable backbone, and the third material is the final photo-responsive elastomer.

2. Synthetic Methods

2.1. Synthetic Scheme

The procedure used to synthesize the new SCLCP, shown in Figure 2-1, uses the mesogen synthesis described by Li[52] and the PVMS backbone and side chain attachment approach of hydrosilylation described previously by Verploegen.[46] The PVMS backbone is a siloxane with a glass transition temperature approaching -100°C in its non-functionalized form. It was chosen to enable a low glass transition even after the attachment of polymer side chains.

The LC has its point of attachment at the center of the mesogen core so that its LC unit director falls parallel, rather than perpendicular, to the polymer main chain, yielding a so called "side-on" SCLCP. This side-on arrangement creates polymer systems whose chain conformations are highly responsive to the arrangement of the LC mesogens [17, 53-55, 58, 59] and was specifically chosen for this work to induce a stronger rheological response to mesogen isotropization as compared to the end-on side chain LC functionalization studied in the earlier polysiloxane based system.[82] After this response was thoroughly characterized, another material, which was identical except with polystyrene (PS) blocks on the ends of the polymer, was synthesized in order to make the material an elastomer. The TBCP proved difficult to make, so its synthesis is described in detail in Section 2.4. Once the polymer was made, however, the attachment reaction, shown in Figure 2-2, was analogous to that in Figure 2-1.

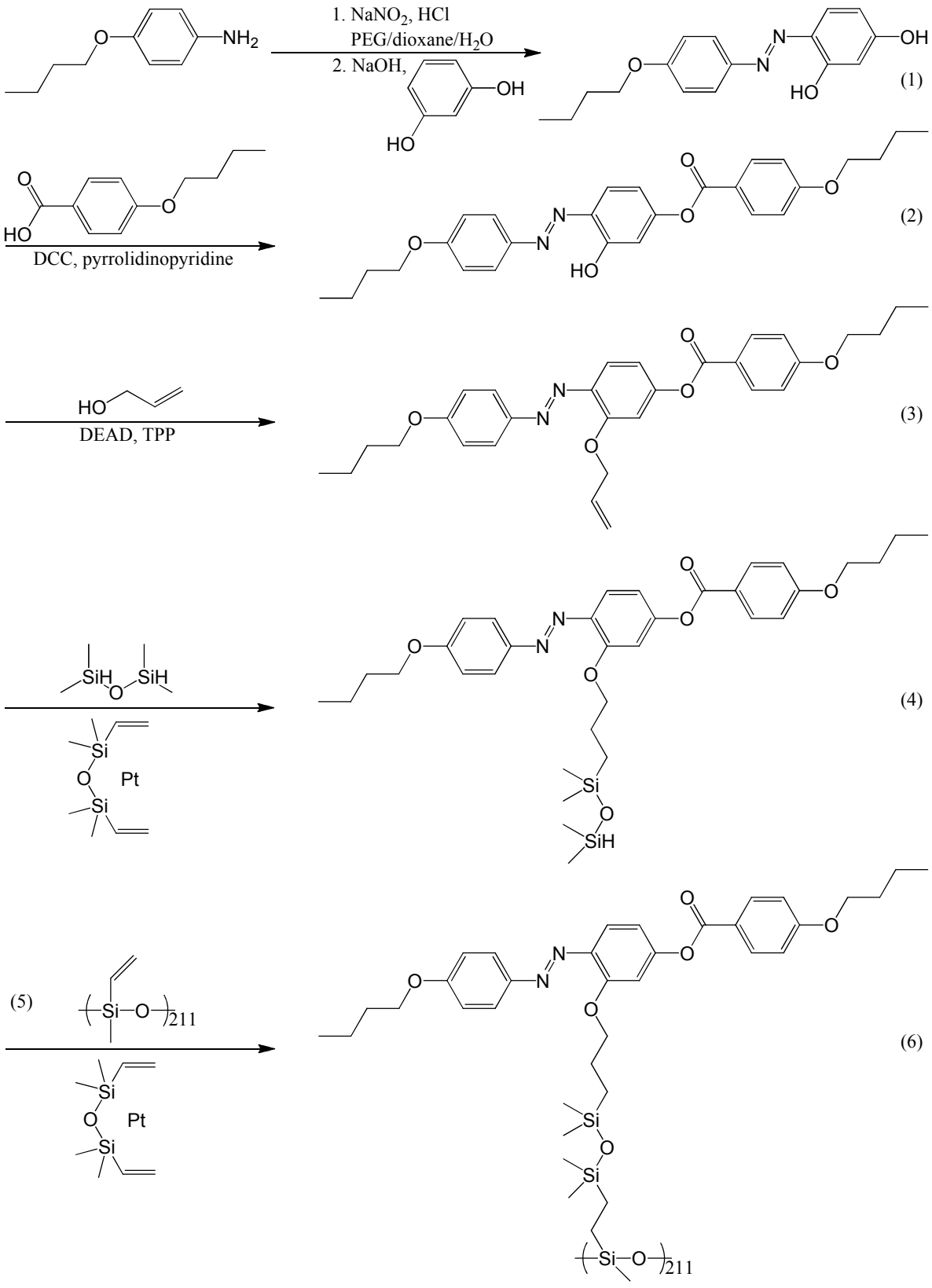

Figure 2-1. Synthesis of new photo-responsive SCLCP.

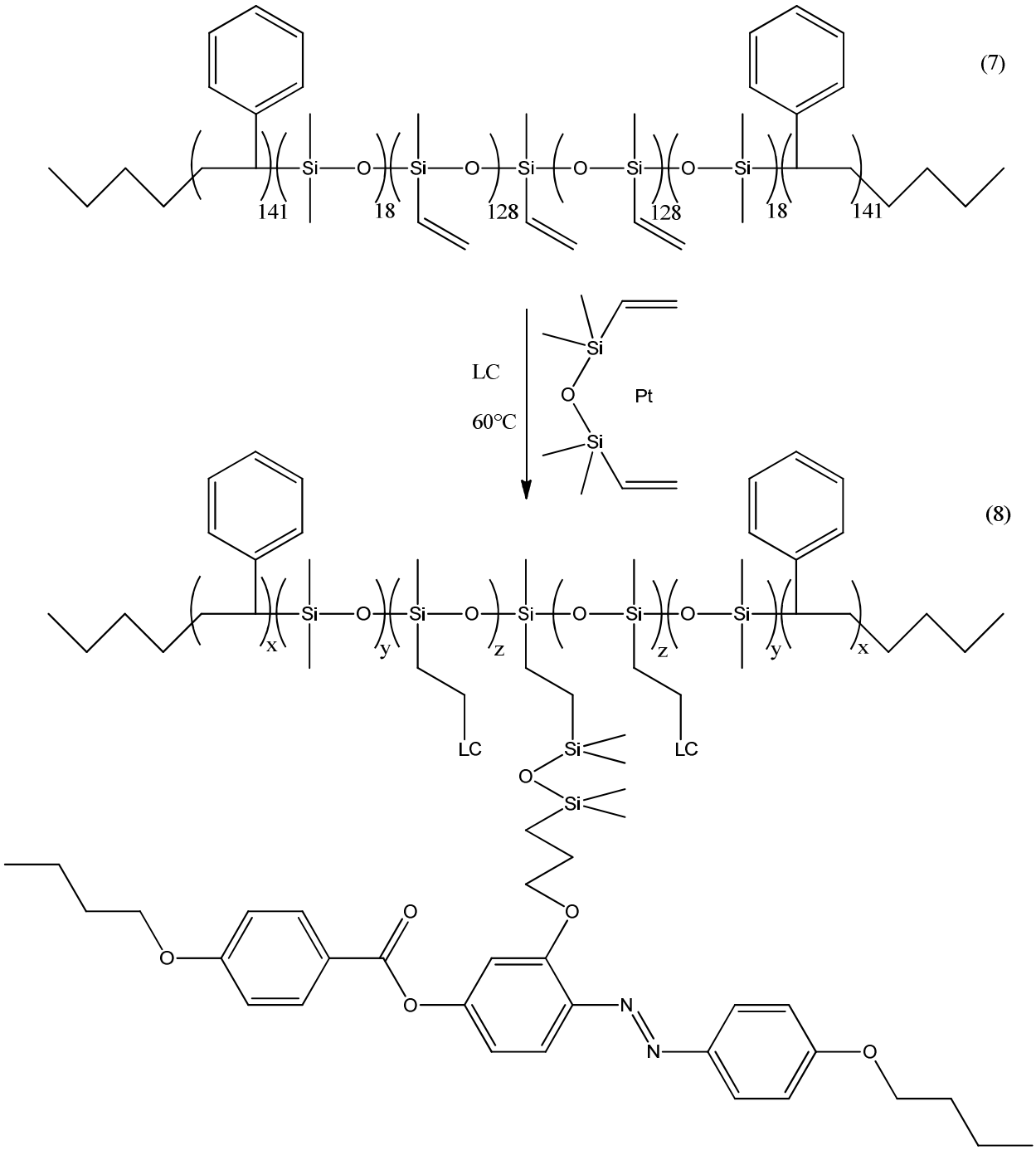

Figure 2-2. LC attachment to PS-PVMS-PS TBCP.

2.2. LC Synthesis

Materials

All the reagents were purchased from Sigma-Aldrich and used without purification.

Instrumentation

^{1}H NMR on a Bruker AVANCE-400 was used to determine molecular structure and degree of conversion for the LC synthesis.

Synthesis of 4-butoxy-2',4'-dihydroxyazobenzene (1)[52]

90 mL of PEG200, 45 mL of 1,4-dioxane, and 15 mL of water were mixed and cooled to 0°C with in an ice bath, and 5.3 mL of concentrated hydrochloric acid and 5.005 g of 4-butoxyaniline were added to this solution. Next, 2.320 g of $NaNO_2$ was dissolved in 10 mL of water and then added dropwise to the 4-butoxyaniline solution. The solution was stirred for 1 hour at 0-10°C. Meanwhile, another portion of 90 mL of PEG200, 45 mL of 1,4-dioxane, and 15 mL of water were mixed and, to it, was added 10.015 g of resorcinol and 1.403 g of NaOH. This solution was heated to 60°C to dissolve all of the solids, cooled to 22°C, and then added to the first solution. Everything was stirred for 15 minutes at 10-20°C, and, after 15 minutes, 350 mL of water was added. HCl was added until the pH was about 5, and the dark red precipitate was filtered, washed with water, and dried in a vacuum oven with P_2O_5 to obtain 7.821 g of crude **1** for a conversion of 90%. ^{1}H NMR data is shown in Figure 2-3.

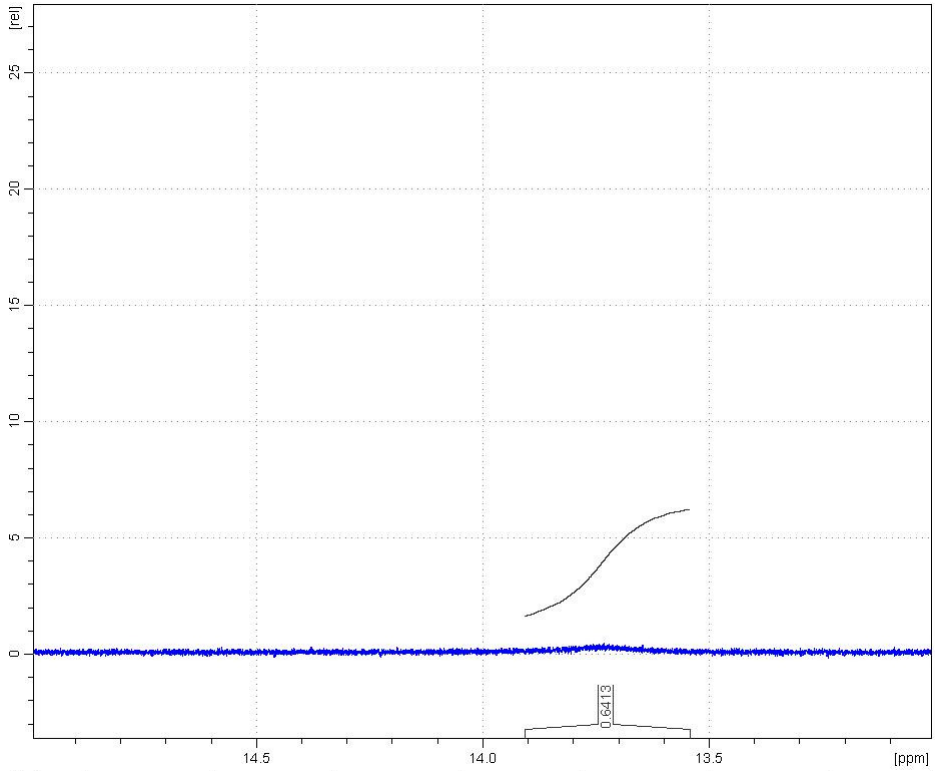
[rel]
25
20
15
10
5
0
0.6413
14.5
14.0
13.5
[ppm]

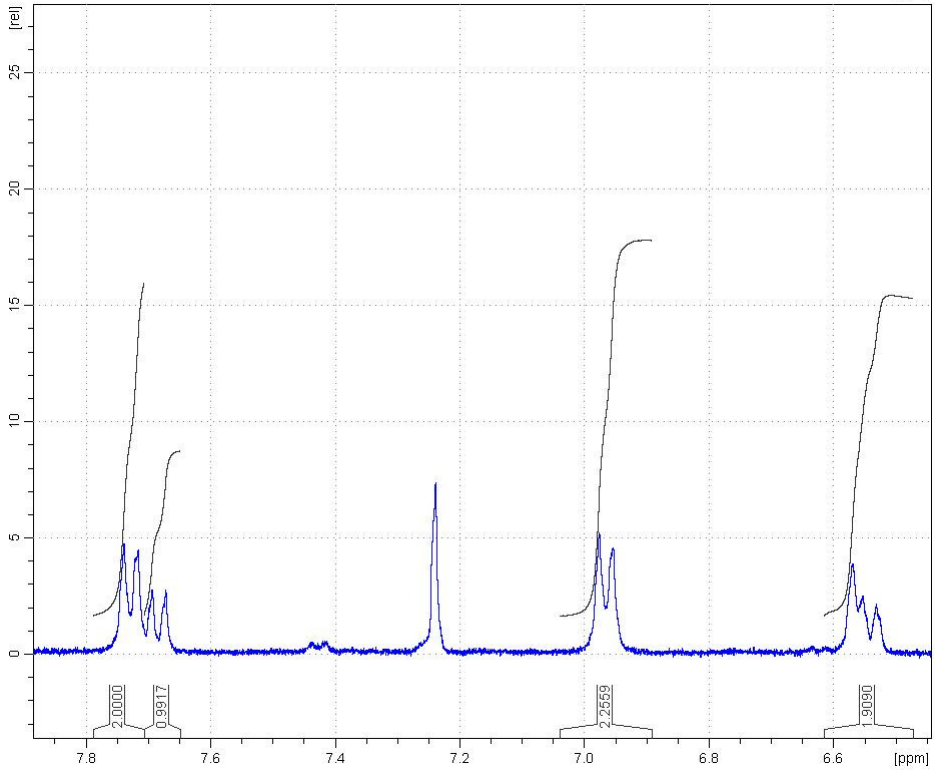
[rel]
25
20
15
10
5
0
2.0000
0.9917
2.2559
1.9090
7.8
7.6
7.4
7.2
7.0
6.8
6.6
[ppm]

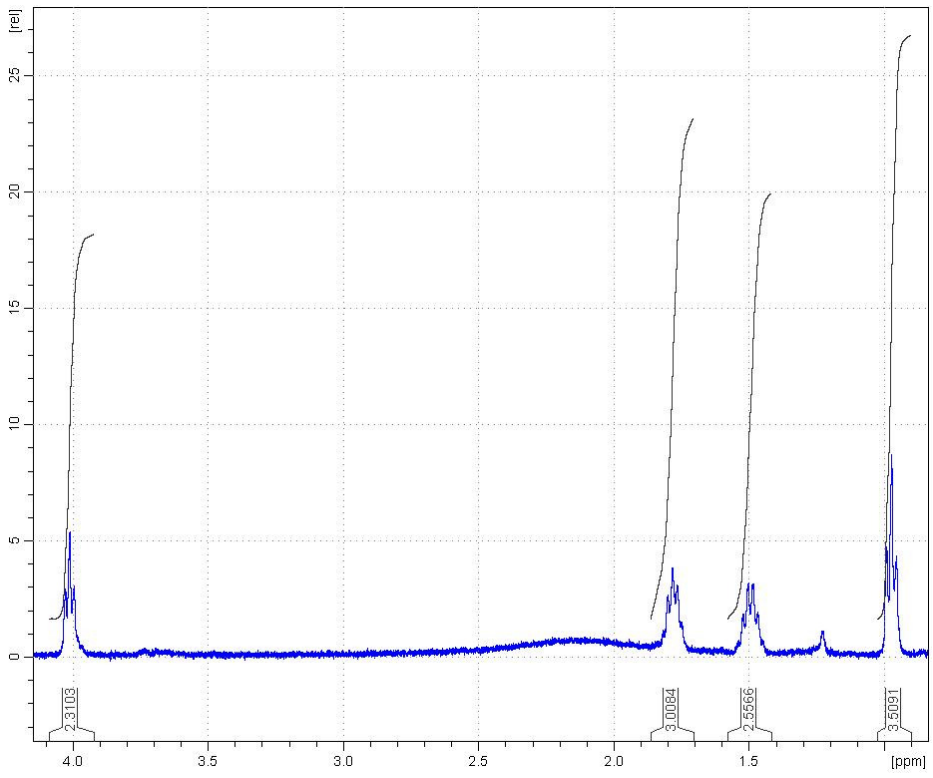

Figure 2-3. ^{1}H NMR spectrum for **1**.

Synthesis of 4-butoxy-2'-hydroxy-4'-(4-butoxybenzyloxy)-azobenzene (2)[52]

To 150 mL of dichloromethane was added 6.873 g of crude **1**, 3.638 g of diisopropylcarbodiimide, 0.444 g of 4-pyrrolidinopyridine, and 4.683 g of 4-butoxybenzoic acid, and the solution was stirred overnight at room temperature. Next, the solution was filtered and shaken successively with 150 mL of water, 150 mL 5% v/v acetic acid, and 150 mL of water. After removal of the dichloromethane, the crude **2** was recrystallized twice in 1:4 v/v toluene:ethanol from 80°C to -40°C, and then it was filtered, washed with more 1:4 v/v toluene:ethanol, removed, and dried to obtain 6.320 g of red **2** for a conversion of 57%. ^{1}H NMR data is shown in Figure 2-4.

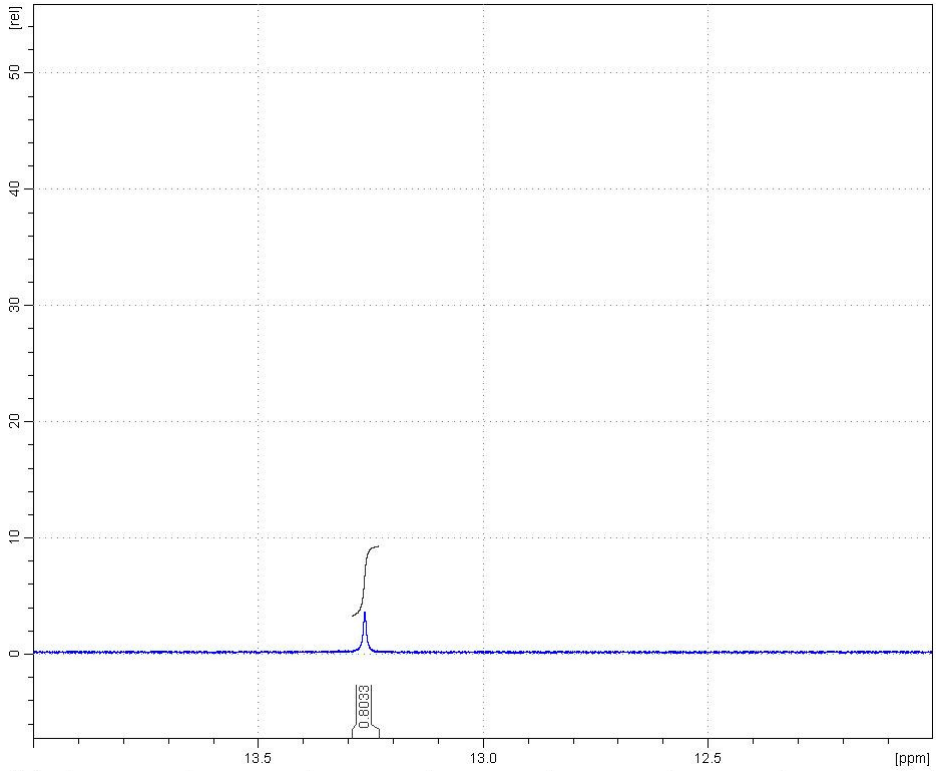
[rel]
50
40
30
20
10
0
0.8033
13.5
13.0
12.5
[ppm]

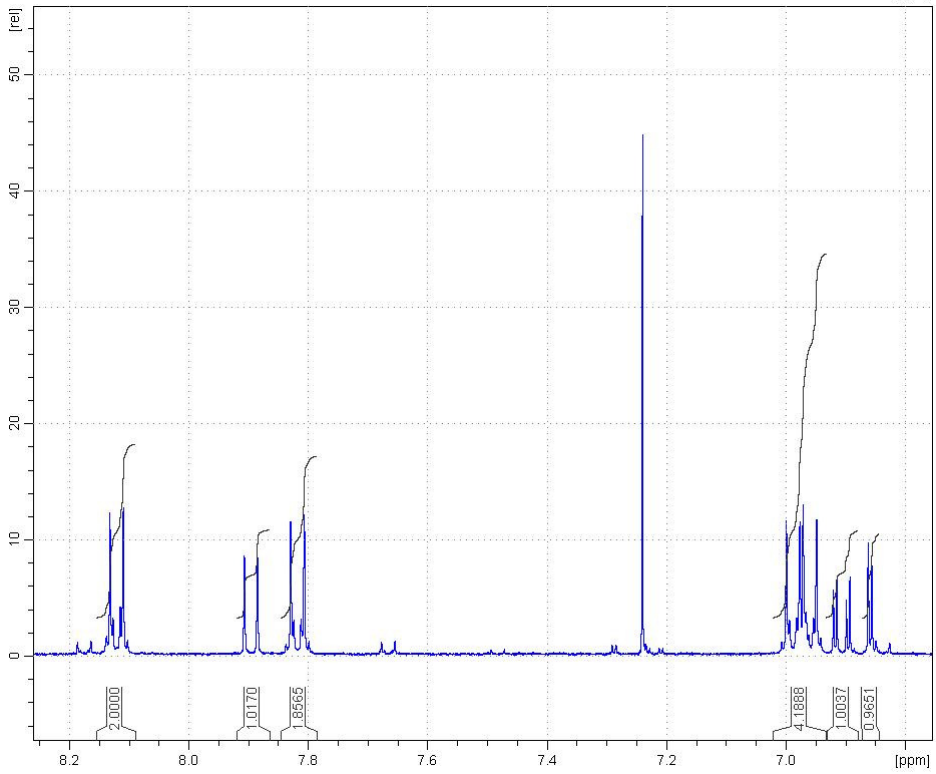
[rel]
50
40
30
20
10
0
2.0000
1.0170
1.8565
4.1888
1.0037
0.9651
8.2
8.0
7.8
7.6
7.4
7.2
7.0
[ppm]

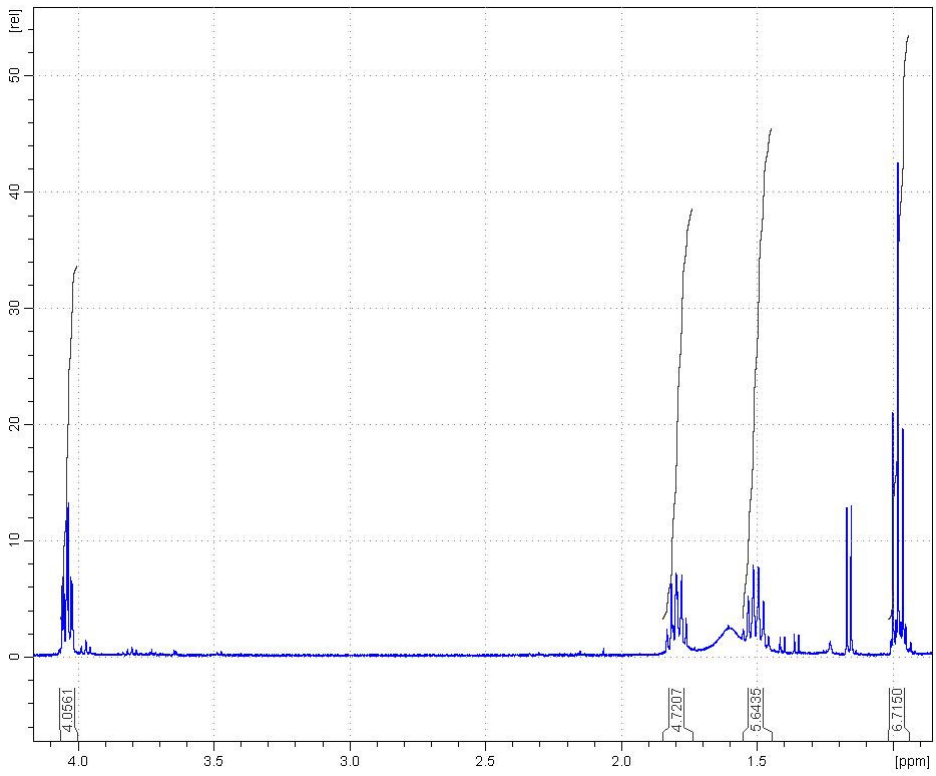

Figure 2-4. ^{1}H NMR spectrum for **2**.

Synthesis of 4-butoxy-2'-allyloxy-4'-(4-butoxybenzyloxy)-azobenzene (3)

This synthesis is similar to that reported previously [52] but with allyl alcohol in place of 4-hydroxybutyl methacrylate. To 100 mL of dichloromethane was added 6.320 g of **2**, and the solution was cooled in an ice bath. Next, 1.001 g allyl alcohol and 5.402 g triphenylphosphine was added, and then 3.541 g of 40 wt% DEAD in toluene was added dropwise. The solution was stirred overnight in the ice bath, and then the dichloromethane was removed. The orange **3** was separated with 1:9 v/v ethyl acetate:hexane on a silica gel column and recrystallization in ethanol from 60°C to room temperature to obtain 5.060 g of **3** for a conversion of 74%. ^{1}H NMR (Figure 2-5): δ 6.8-8.2 (m, 11H, Ar), 6.10 (m, -O-CH_2-C*H*=CH_2), 5.47 (t, -O-CH_2-CH=CH_2(Z), 5.34 (q, -O-CH_2-CH=CH_2(E)), 4.74 (d, O-CH_2-CH=CH_2), 4.65 (br. s, O-CH_2-CH=CH_2).

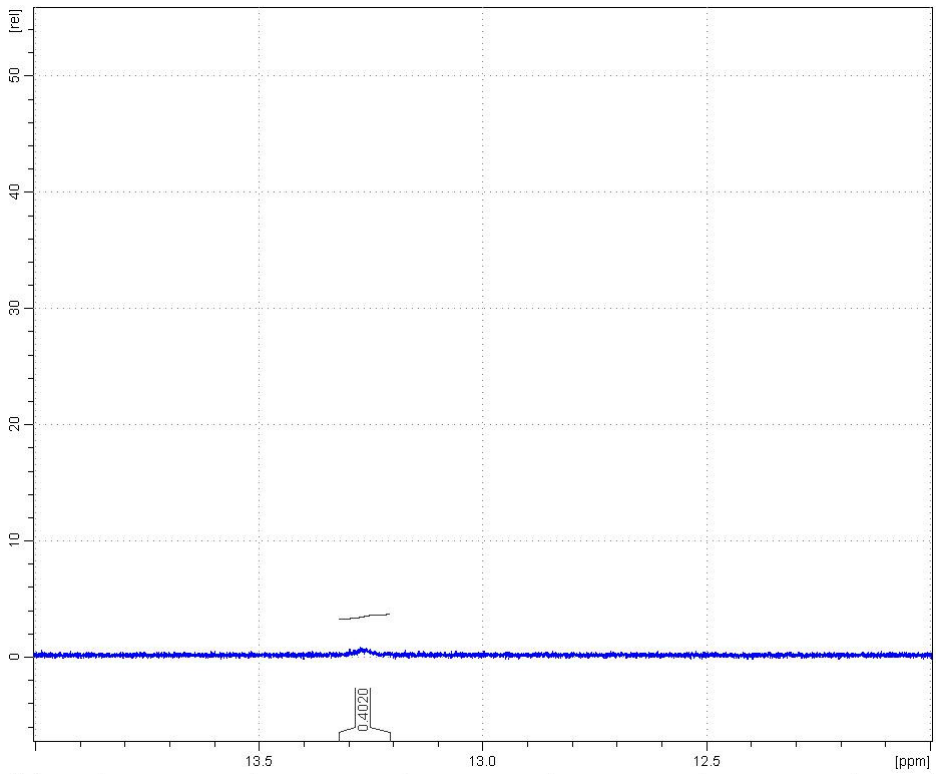
[rel]
50
40
30
20
10
0
0.4020
13.5
13.0
12.5
[ppm]

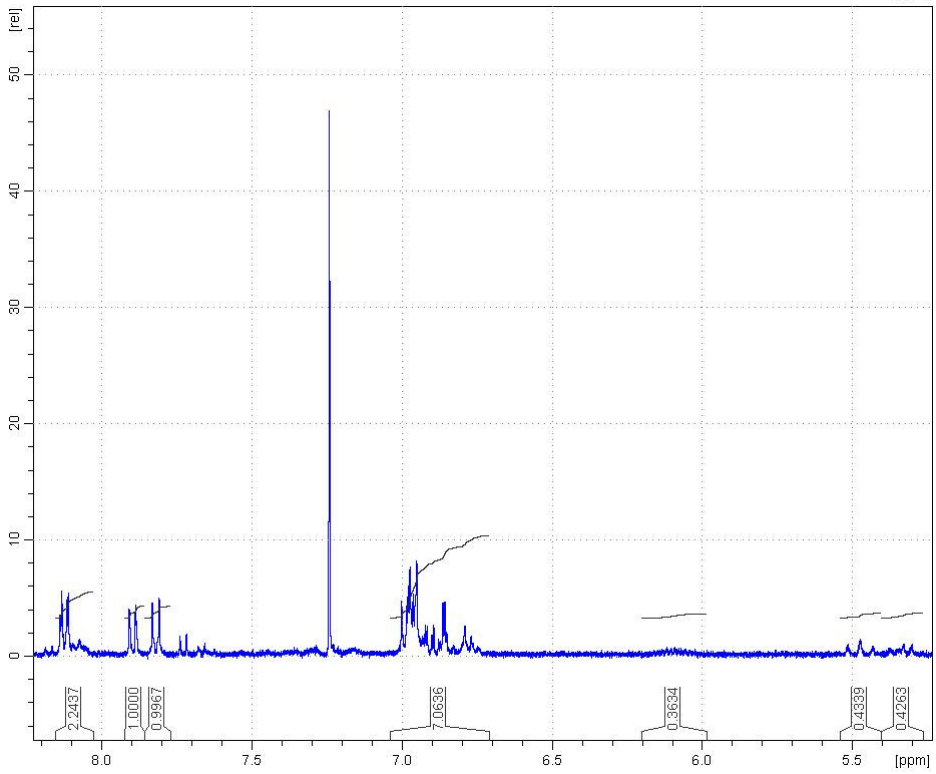
[rel]
50
40
30
20
10
0
2.2437
1.0000
0.9967
7.0636
0.3634
0.4339
0.4263
8.0
7.5
7.0
6.5
6.0
5.5
[ppm]

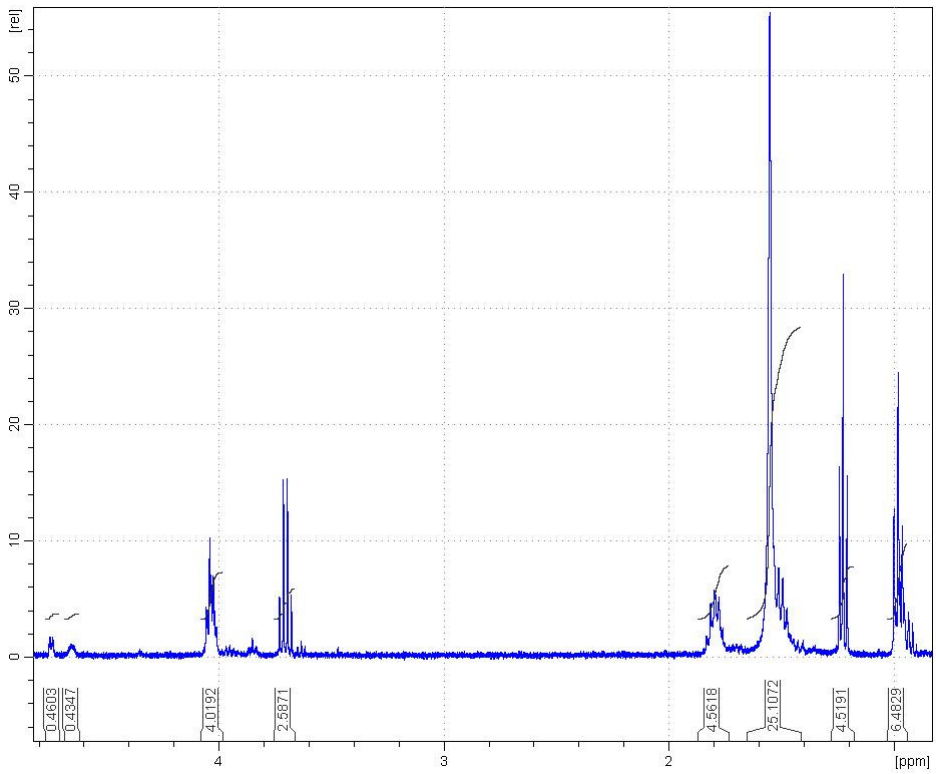

Figure 2-5. ^{1}H NMR spectrum for **3**.

Synthesis of 4-butoxy-2'-(3-(1,1,3,3-tetramethyldisiloxanyl)propoxy)-4'-(4-butoxybenzyloxy)-azobenzene (4)

This synthesis is similar to that reported previously.[46] 13.468 g of 1,1,3,3-tetramethyldisiloxane and 25 mL of toluene was mixed at room temperature. A second solution with 5.060 g of **3**, 25 mL of toluene, and 10 drops of Pt(0)-1,3-divinyl-1,1,3,3-tetramethyldisiloxane complex solution in xylene (Pt ~2%) was mixed. This solution was added dropwise to the first solution to obtain a red solution and then stirred overnight at 60°C under N_2. The orange **4** was separated with 1:9 v/v ethyl acetate:hexane on a silica gel column to obtain 1.922 g for a conversion of 30%. ^{1}H NMR (Figure 2-6): δ 6.8-8.2 (m, 11H, Ar), 4.73-4.62 (m, -Si$(CH_3)_2$-O-Si*H*$(CH_3)_2$), 0.0-0.3 (m, -Si*$(CH_3)_2$*-O-SiH*$(CH_3)_2$*).

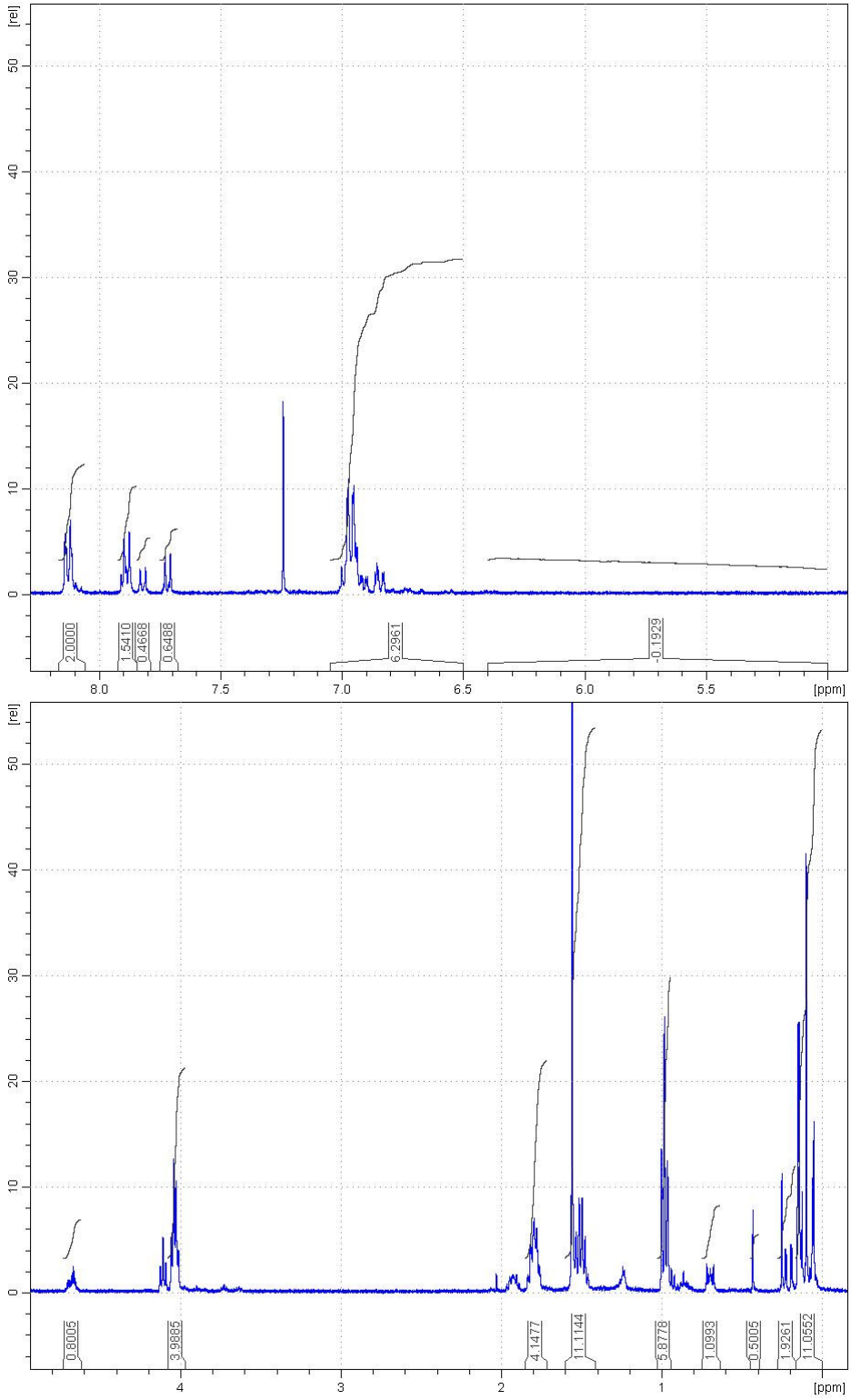

Figure 2-6. ^{1}H NMR spectrum for **4**.

2.3. PVMS Synthesis (5)

Materials

1,3,5-Trivinyl-1,3,5-trimethylcyclotrisiloxane (V_3) and 1,4-bis(hydroxydimethylsilyl)benzene were purchased from Gelest, Inc., and all other reagents were purchased from Sigma-Aldrich. No purification was performed on any of the reagents or solvents, except for the tetrahydrofuran (THF) polymerization solvent, which was taken from an Innovative Technologies, Inc., solvent purification system and dried with sodium (Na).

Instrumentation

Anionic polymerization in an Innovative Technologies, Inc. glovebox was used to make poly(vinylmethylsiloxane) (PVMS), and Gel Permeation Chromatography (GPC) with a Waters 717plus Autosampler running THF as the mobile phase was used to determine the molecular weight (MW) and the polydispersity index (PDI) of the PVMS. ^{1}H NMR on a Bruker AVANCE-400 was used to determine molecular structure and degree of conversion for the LC synthesis and attachment.

Procedure[46]

In the glovebox, to 50 mL of THF dried with Na was added .0077 g of 1,4-bis(hydroxydimethylsilyl)benzene and 7 drops (.04mL) of butyllithium (bu-Li), and the solution was stirred for 40 minutes at room temperature. 1 mL of 1,3,5-trivinyl-1,3,5-trimethylcyclotrisiloxane (V_3) was added and stirred overnight at room temperature. A sample was removed, filtered, and run on the GPC, which measured the Mn as 18,000 g/mol and PDI as 1.18. ^{1}H NMR was also run on the sample to produce Figure 2-7.

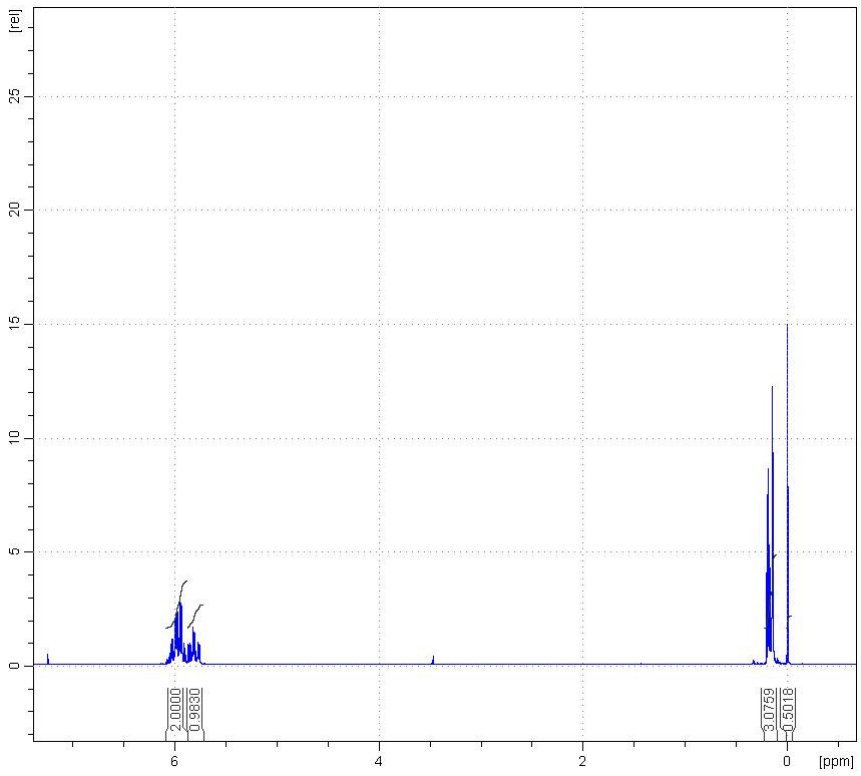

Figure 2-7. ^{1}H NMR of PVMS (**5**).

2.4. PS-PVMS-PS Triblock Copolymer (7) Synthesis

Materials

Hexamethylcyclotrisiloxane (D_3) and 1,3,5-Trivinyl-1,3,5-trimethylcyclotrisiloxane (V_3) were purchased from Gelest, Inc., and all other reagents were purchased from Sigma-Aldrich. Styrene was dried overnight with CaH_2 under N_2 and then vacuum distilled at 35°C. D_3 was dissolved in cyclohexane and dried overnight with CaH_2 under N_2. Then the cyclohexane was remove by vacuum, and the D_3 was vacuum distilled at 80°C. V_3 was dried overnight with CaH_2 under N_2, vacuum distilled at 50°C, and then degassed with 3 freeze-pump-thaw cycles. Dichloromethylvinylsilane was dried overnight with CaH_2 under N_2 and then distilled at 90°C.

Finally, tetrahydrofuran (THF) was taken from an Innovative Technologies, Inc., solvent purification system, dried with Na, and degassed with 3 freeze-pump-thaw cycles.

Instrumentation

Anionic polymerization in an Innovative Technologies, Inc. glovebox equipped with a Julabo FT 900 immersion cooler in a stirring heptanes bath was used to make PS-PVMS-PS. Gel Permeation Chromatography (GPC) with a Waters 717plus Autosampler running THF as the mobile phase was used to determine the molecular weight (MW) and the polydispersity index (PDI) of each block in the copolymer, and ^{1}H NMR on a Bruker AVANCE-400 was used to determine the ratio between PS, PDMS, and PVMS in the final polymer.

Procedure

The PS-PVMS-PS synthetic scheme is shown in Figure 2-8. In the glovebox, a flamed 50 mL round flask, glass stopper, and stir bar were washed three times with ~1 mL of sec-butyllithium (sec-bu-Li) and four times with ~20 mL of THF. Next, ~30 mL of THF were added to the flask, which was then immersed in the heptane bath at -60°C for 1 hour. To start the polymerization, 0.05 mL of sec-bu-Li was added to the cold, stirring solution, and then 1 mL of styrene was added quickly, after which the solution turned orange. After 1 hour, a solution of 0.0222 g D_3 and 0.2 mL THF was added. 4 hours later the solution was still light orange, so it was removed from the heptane bath causing it to turn clear in 1 hour. Next, 1 mL of V_3 was added, and 2 hours later, 85 μL of 0.0500 g/mL dichloromethylvinylsilane in THF solution was added and stirred overnight. About half the THF in the resulting solution was removed with rotary evaporation, and the resulting concentrated polymer solution was precipitated in 100 mL of stirring methanol, filtered, re-dissolved in about 20 mL of THF, precipitated in 100 mL of

stirring methanol, filtered, and then dried with rotary evaporation at 60°C for 30 minutes. 1.32 g of white powder **7** was produced.

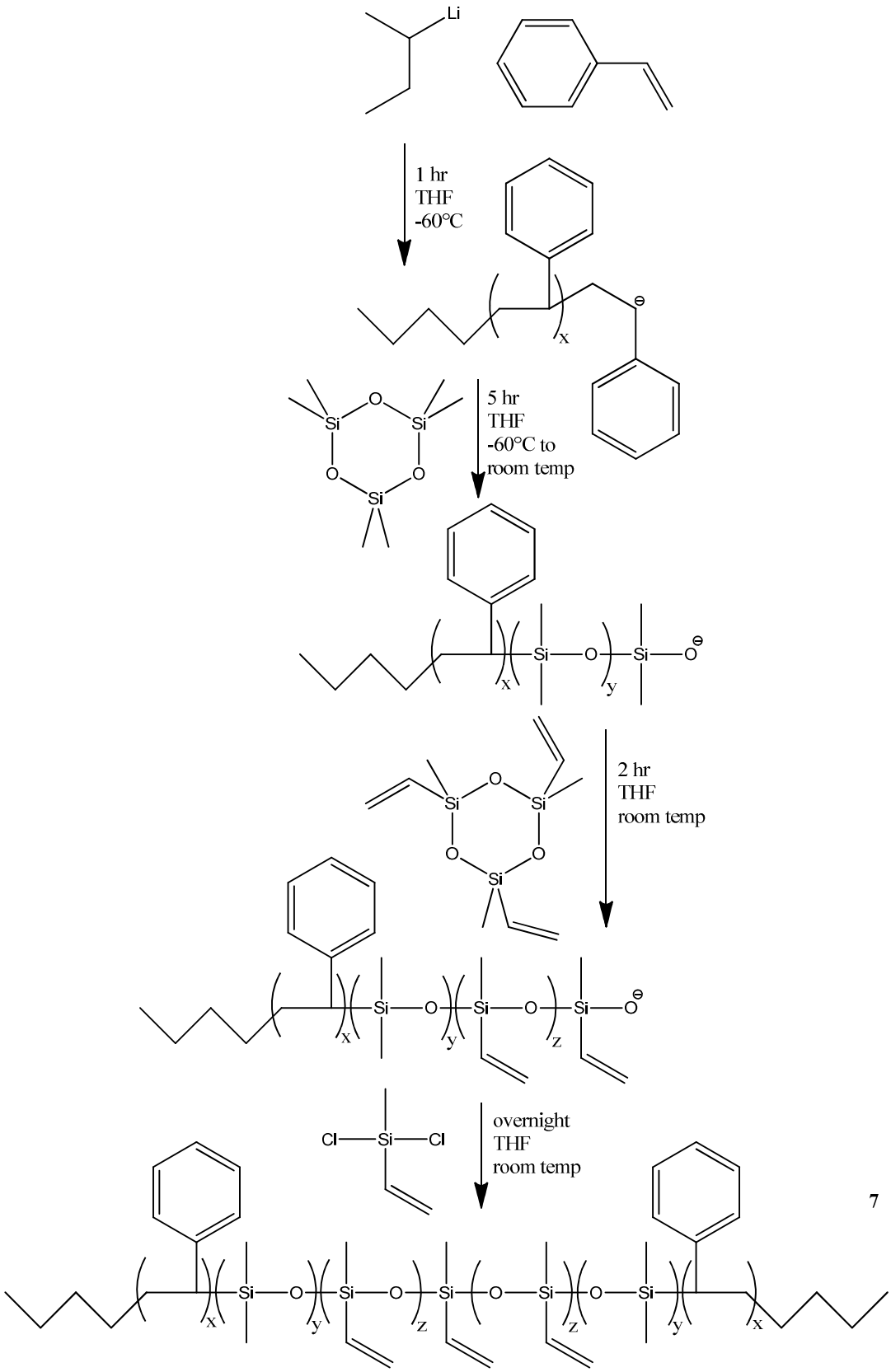

Figure 2-8. PS-PVMS-PS synthetic scheme.

Results and Discussion

Anionic polymerization in THF at -60°C proved to be a simple way to make the PS-PVMS-PS TBCP. Actually, it is PS-PDMS-PVMS-PDMS-PS, but the PDMS blocks are small and compatible with the PVMS, which is why it is referred to as just PS-PVMS-PS. The D_3 is added to cap the PS so that the polystyryl anion does react with any of the vinyl groups of the V_3 monomer. Having 4 steps does make it difficult to keep the polymers alive, but it is still a "one pot" synthesis that takes only day, disregarding the monomer and solvent purification.

After each step in the polymerization, a 0.1 mL samples was removed and terminated in methanol for analysis with the GPC. Figure 2-9 shows the MW traces from the GPC calibrated with PS standards for all the steps in the polymerization, and Table 2-1 lists the corresponding number average MW's (Mn), peak MW's (Mp), PDI's. The PS in the first step has the desired MW of 15,000 g/mol with a small PDI. The PDMS from the second step is quite small and seems to have had little effect on the polymer. The PS-PVMS from the third step has the desired MW around 30,000 g/mol still with a small PDI, most likely due to termination by the addition of dichloromethylvinylsilane because, if the PVMS remained alive for longer than a few hours, it would back-bite itself and significantly lower its MW and raise its PDI.[128] The PS-PVMS-PS from the final step has a MW lower than the desired MW and a PDI higher than that from the other steps due to imperfect coupling followed by back-biting. Its MW trace in Figure 2-9 shows a Mp near 60,000 g/mol but also a shoulder around 30,000 g/mol, and this shoulder is excess uncoupled PS-PVMS. Furthermore, this uncoupled PS-PVMS has moved to a lower MW suggesting that it remained and back-bit itself until the polymerization was terminated. Nonetheless, most of the polymer in the mixture is PS-PVMS-PS TBCP, which is sufficient to produce a thermoplastic elastomer.

To gain more accurate MW data for the PDMS and PVMS, ^{1}H NMR was used in conjunction with GPC. The MW for the PS from the first step is accurate because the GPC was calibrated with PS standards; however, there is error associated with using those same standards for the rest of the block copolymers. Therefore, the final PS-PVMS-PS was analyzed with ^{1}H NMR, as shown in Figure 2-10, and the molar ratio between PS and PDMS and between PS and PVMS in conjunction with the PS MW from the GPC was used to calculate their Mn's, respectively. For the PS-PVMS-PS, all was assumed to be coupled; otherwise, the uncoupled polymer would have back-bit itself and been removed with the precipitation steps. The results of these calculations are also in Table 2-1, and they show good agreement with the target PS-PVMS ratio and MW's.

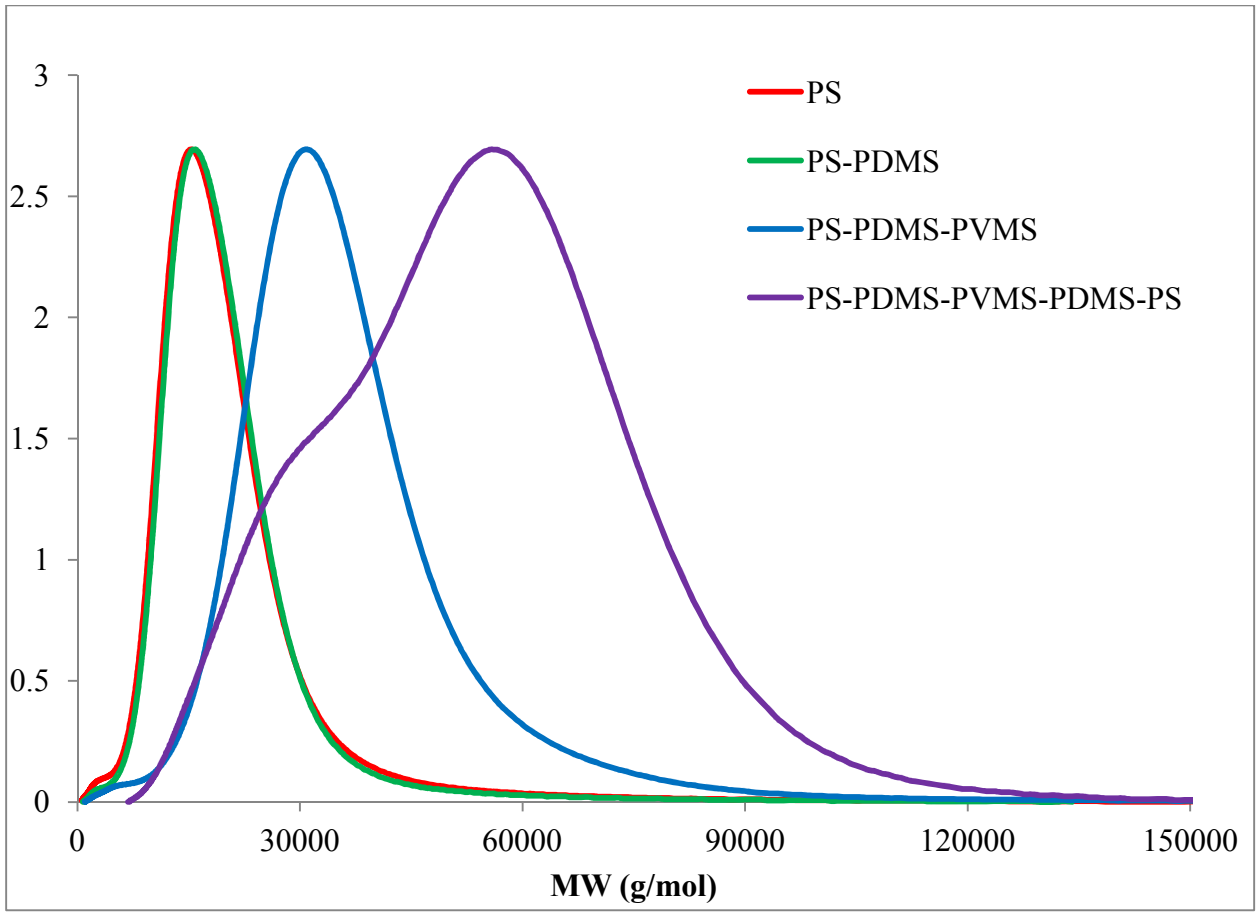

Figure 2-9. MW traces from the GPC of the PS-PVMS-PS synthetic steps.

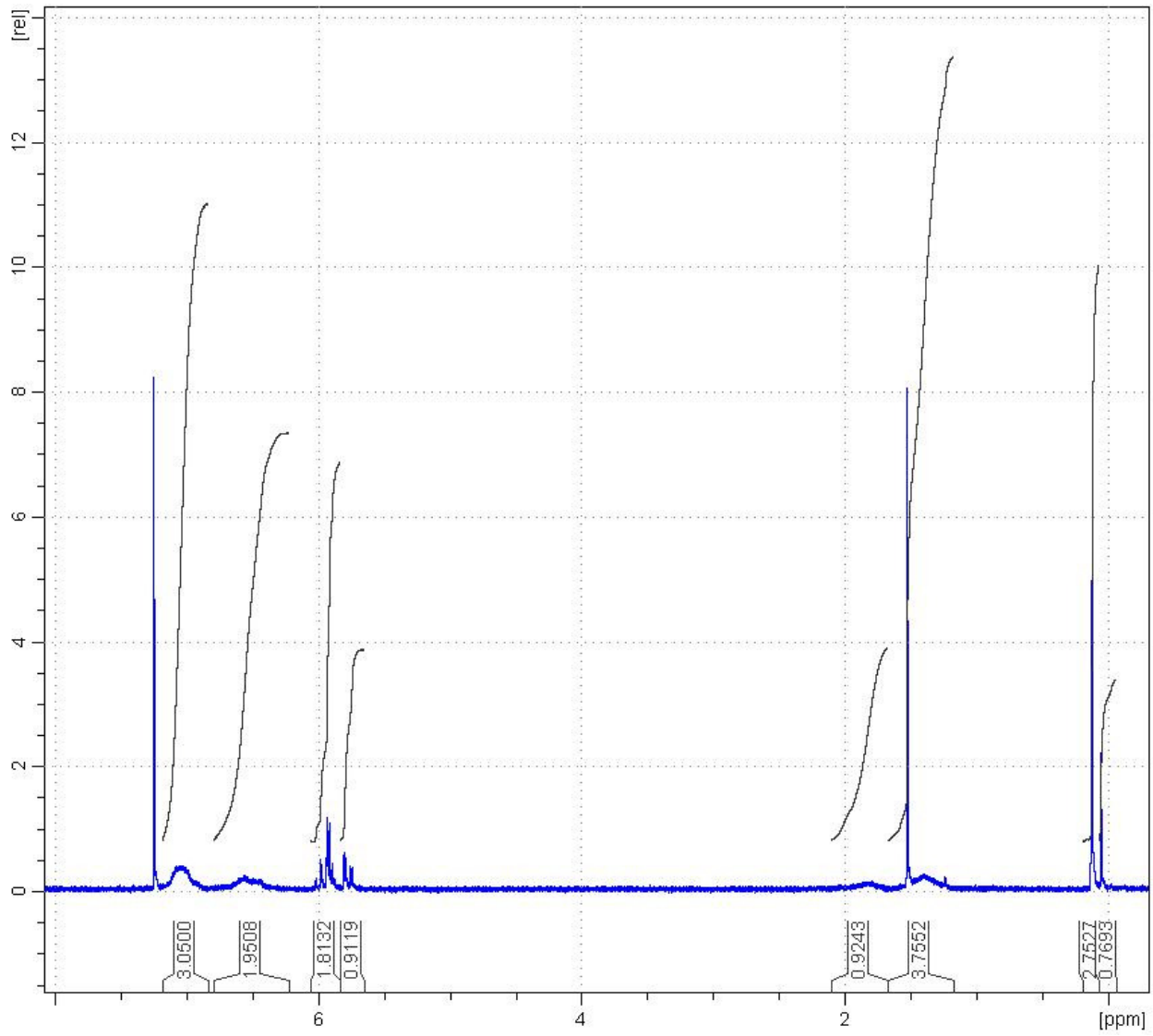

Figure 2-10. ^{1}H NMR sprectrum of the PS-PVMS-PS TBCP.

Table 2-1. MW and PDI of all the steps in the PS-PVMS-PS polymerization. [a] denotes GPC data, and [b] denotes ^{1}H NMR data.

Polymer	Mn [a] (10^3 g/mol)	Mp [a] (10^3 g/mol)	PDI [a]	PS ratio [b]	Mn [b] (10^3 g/mol)
PS	14.7	15.3	1.15	1.00	14.7
PS-PDMS	15.0	15.8	1.14	0.13	16.0
PS-PDMS-PVMS	28.0	30.9	1.14	0.91	27.1
$(PS\text{-}PDMS\text{-}PVMS)_2$	35.4	56.0	1.29	0.91	54.2

2.5. LC Attachment

Instrumentation

^{1}H NMR on a Bruker AVANCE-400 was used to determine molecular structure and degree of conversion for the LC attachment.

Attachment to PVMS[46]

8 mL of toluene was added to 1.922 g of **4**. A second solution was made by adding 3 mL of toluene and 10 drops of Pt(0)-1,3-divinyl-1,1,3,3-tetramethyldisiloxane complex solution in xylene (Pt ~2%) to .134 g of **5**. This solution was added dropwise to the first solution and then stirred overnight at 60°C under N_2. The solution was precipitated in 100 mL of methanol, and the resulting dark brown oil was filtered out. ^{1}H NMR confirmed the complete disappearance of the vinyl peak for an attachment of 100%. ^{1}H NMR (Figure 2-11): δ 8.12 (d, -O_2C-Ar$H_2$$H_2$-O-bu), 7.90 (d, -$N_2$-Ar$H$$H_2$-$O_2$C), 7.82 (d, bu-O-Ar$H_2$$H_2$-$N_2$(Z to spacer)), 7.06-6.64 (m, bu-O-Ar$H_2$$H_2$-$N_2$- bu-O-Ar$H_2$$H_2$-$N_2$(E to spacer) -$N_2$-Ar$H$$H_2$-$O_2$C- -$O_2$C-Ar$H_2$$H_2$-O-bu), 4.04 (td, -O-C$H_2$$CH_2CH_2CH_3$), 4.15-3.67 (br. t, -O-C$H_2$$CH_2CH_2$-Si-), 1.96-1.56 (br. m, -O-CH_2C$H_2$$CH_2$-Si-), 1.80 (p, -O-$CH_2CH_2$$CH_2CH_3$), 1.50 (sex, -O-$CH_2CH_2CH_2$$CH_3$), 1.23, (t, -O-$CH_2CH_2CH_2$-Si-,), 0.98 (t, -O-$CH_2CH_2CH_2CH_3$), 0.94-0.32 (br. m, -O-Si-$(CH_3)_2$-CH_2CH_2-Si(CH_3)-O-), 0.17--0.07 (br. m, -Si(CH_3)).

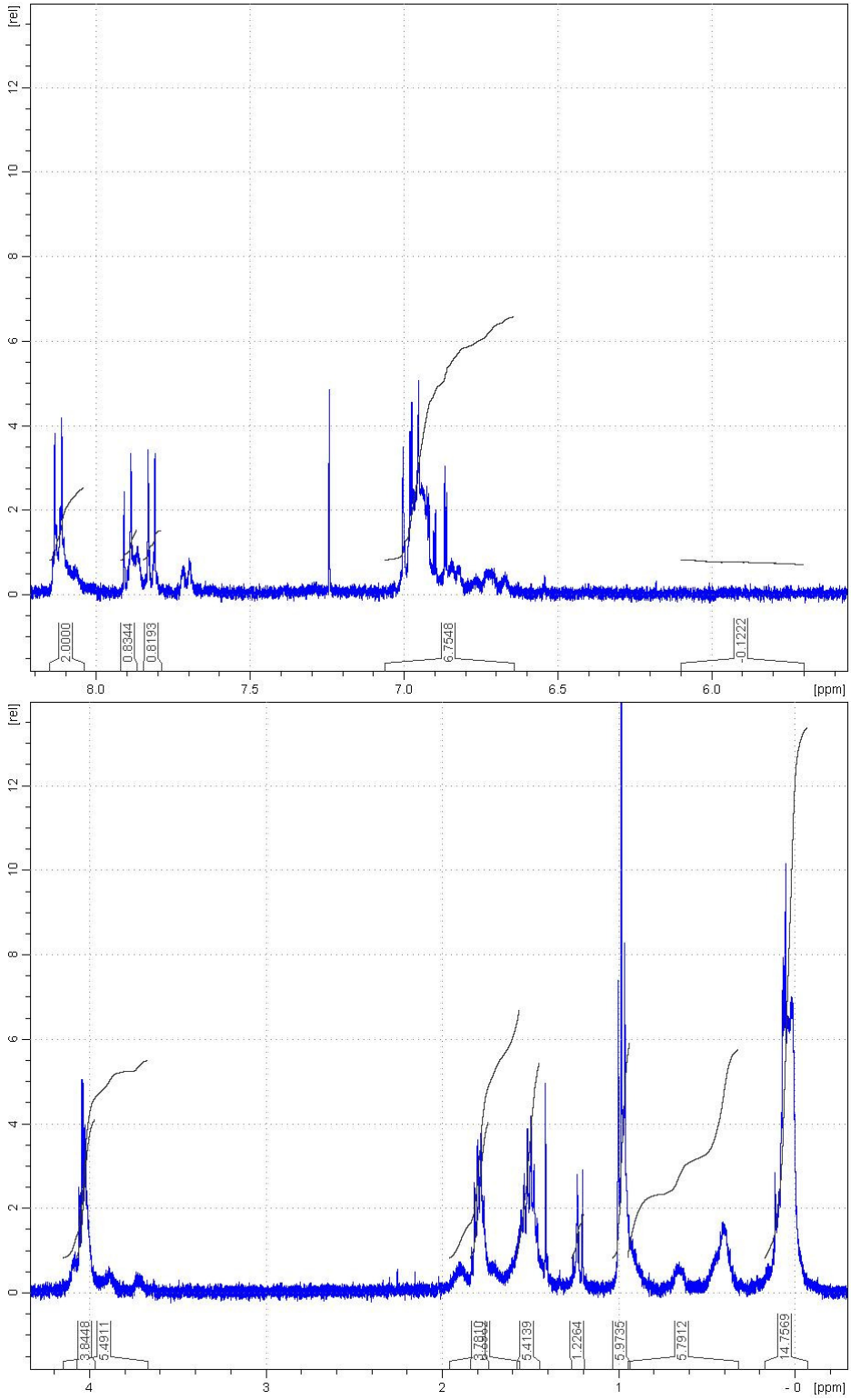

Figure 2-11. ^{1}H NMR spectrum for **6**.

Attachment to PS-PVMS-PS (8)

8 mL of toluene was added to 1.9988 g of **4**. A second solution was made by adding 3 mL of toluene and 10 drops (~0.2 mL) of Pt(0)-1,3-divinyl-1,1,3,3-tetramethyldisiloxane complex solution in xylene (Pt ~2%) to 0.3383 g of **7**. This solution was added dropwise to the first solution and then stirred over two nights at 60°C under N_2. The toluene was then removed by rotary evaporation, and the resulting brown **8** was re-dissolved in 10 mL of THF and precipitated in 100 mL of methanol. The solid **8** was filtered, and the dissolution and precipitation procedure was repeated, and then it was repeated twice more but with 20 mL of THF and 80 mL of methanol. The final product was dried with rotary evaporation to produce 1.1014 g of solid brown **8**. ^{1}H NMR in Figure 2-12 confirmed the complete disappearance of the vinyl peak for an attachment of 100%, and the GPC trace in Figure 2-13 showed the complete shift of the MW. All of the molecular weight measurements and calculations are in Table 2-2. ^{1}H NMR (Figure 2-12): δ 8.12 (br. s, -O_2C-Ar$H_2$$H_2$-O-bu), 7.90 (br. s, -$N_2$-Ar$H$$H_2$-$O_2$C), 7.82 (br. s, bu-O-Ar$H_2$$H_2$-$N_2$(Z to spacer)), 7.2-6.2 (m, bu-O-Ar$H_2$$H_2$-$N_2$- bu-O-Ar$H_2$$H_2$-$N_2$(E to spacer) -$N_2$-Ar$H$$H_2$-$O_2$C- -$O_2$C-Ar$H_2$$H_2$-O-bu Ar-PS), 4.15-3.67 (br. s, -O-C$H_2$$CH_2CH_2CH_3$ -O-C$H_2$$CH_2CH_2$-Si-), 2.0-1.1 (br. m, -O-CH_2C$H_2$$CH_2$-Si- -O-$CH_2CH_2$$CH_2CH_3$ -O-CH_2CH_2C$H_2$$CH_3$ -O-CH_2CH_2CH_2-Si- CH_2-CH-PS), 1.05-0.7 (br. s, -O-$CH_2CH_2CH_2$CH_3), 0.94-0.32 (br. m, -O-Si-$(CH_3)_2$-CH_2CH_2-Si(CH_3)-O-), 0.17--0.07 (br. m, -Si(CH_3)).

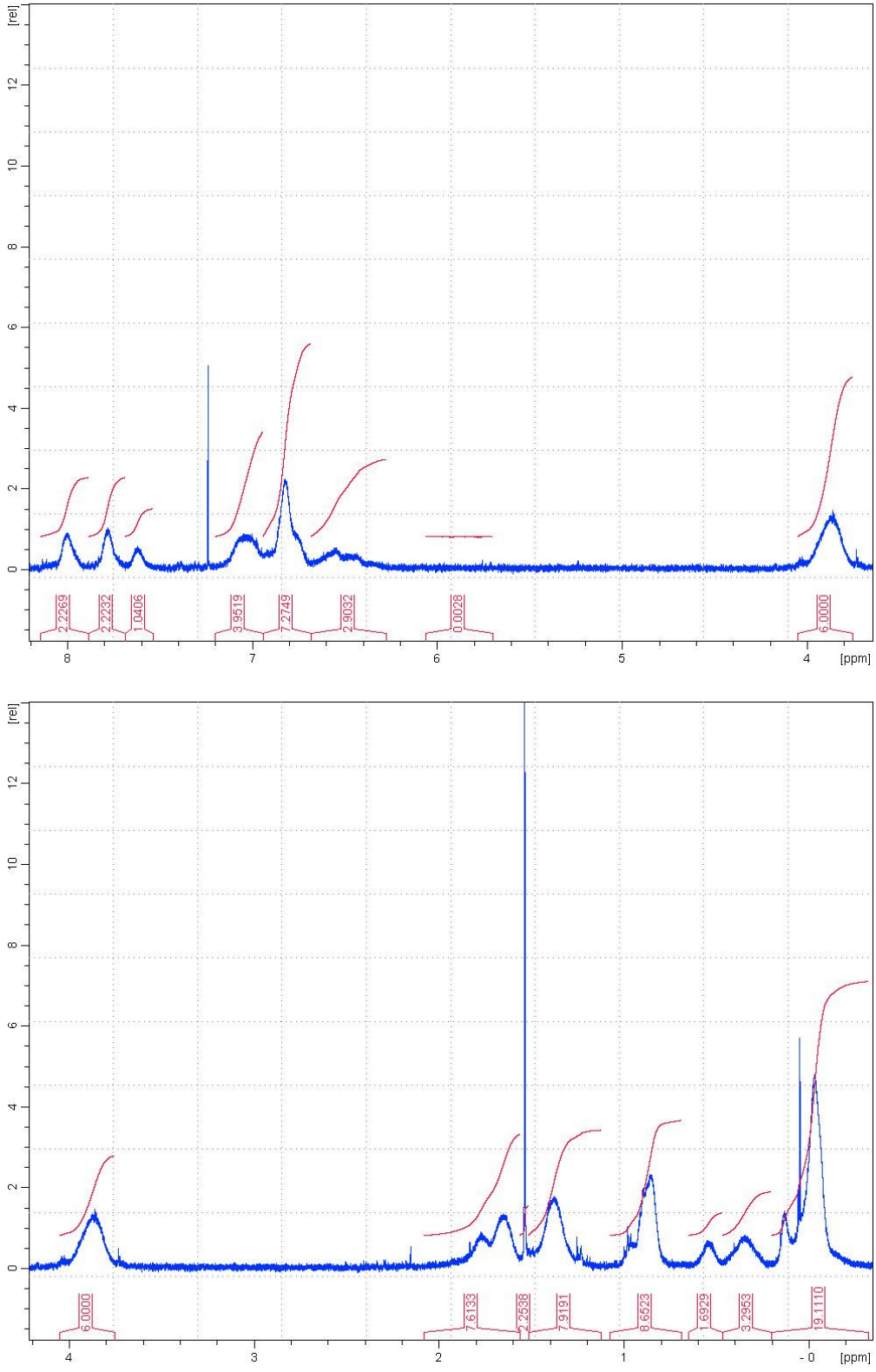

Figure 2-12. ^{1}H NMR spectrum for **8**.

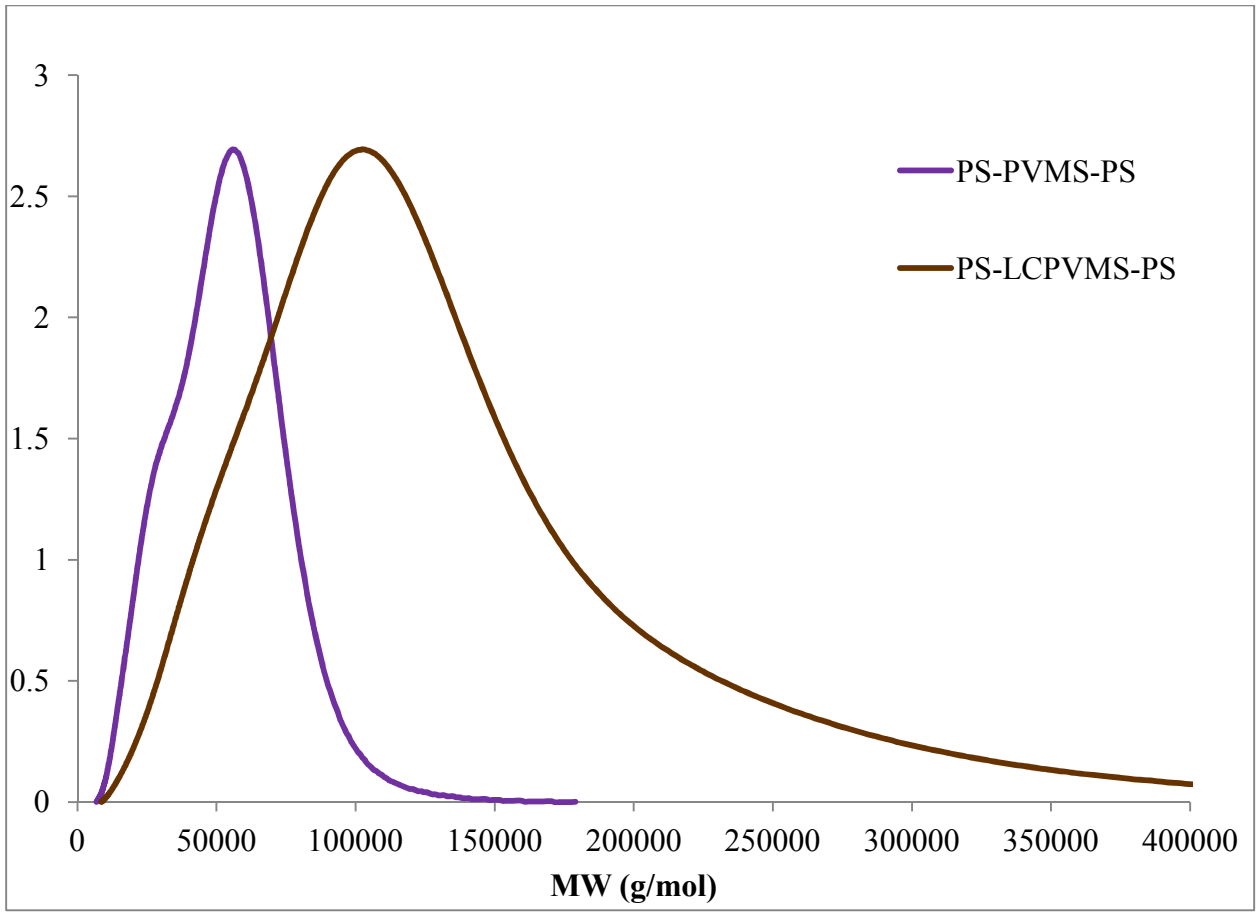

Figure 2-13. MW traces from the GPC of the LC attachment to the PS-PVMS-PS TBCP.

Table 2-2. MW and PDI of the LC attachment to the PS-PVMS-PS TBCP. [a] denotes GPC data, and [b] denotes ^{1}H NMR data.

Polymer	Mn [a] (10^3 g/mol)	Mp [a] (10^3 g/mol)	PDI [a]	PS ratio [b]	Mn [b] (10^3 g/mol)
PS-PVMS-PS (7)	35.4	56.0	1.29	0.00	54.2
PS-LCPVMS-PS (8)	68.8	103.0	1.47	0.91	111.6

3. Photo-responsive LCP Characterization

3.1. Instrumentation.

Differential Scanning Calorimetry (DSC) on a Thermal Advantage (TA) Instruments DSC Q1000 was used to measure the various transition temperatures of the material. Small Angle X-ray Scattering (SAXS) on a Micro MAX Rigoko SAXS System with a Cu Kα source was used to help identify the LC phase. Polarizing Optical Microscopy (POM) with a Zeiss Axioskop 2 MAT and an AxioCam MRc camera recorded with CamStudio screen-capture software was used to characterize the LC phase, and, during this characterization, UV light centered at 360 nm from a Dymax Blue Wave 200 with a Thorlabs, Inc. FGUV W53199 UV filter was shined on the material. The UV light intensity was measured with a Dymax ACCU-CAL 50 radiometer. Finally, anisotropic spectroscopic ellipsometry on a J.A. Woollam Co., Inc. XLS-100 was used to measure refractive indices and birefringence.

3.2. SCLCP properties and characterization.

The freshly synthesized, solvent-cast, or annealed SCLCP is a dark brown gel-like viscous liquid. After being stretched, spread, or strained in any way or after sitting for a few days to a week at room temperature, the SCLCP turns into a light brown crystalline solid. This behavior can be explained by the DSC in Figure 3-1, which shows 2 scan cycles for a sample of SCLCP a week after annealing at 100°C. Both cycles show an LC isotropization (T_{iso}) peak at about 73°C, but the first cycle shows an extra crystalline melting peak (T_m) at 42°C. The T_m does not show up on the second cycle because, after the crystalline phase has melted from the first heating cycle, it takes at least several days to reform again. The glass transition temperature (T_g) of the LC-functionalized polysiloxane backbone is approximately -7°C; although higher than that

of most polysiloxanes,[129] this value is quite low compared to that of most photo-responsive SCLCP's and is also well below room temperature.[18, 19, 23-25, 56]

There is also a noticeable difference between the crystalline and the nematic phases in the Small Angle X-ray Scattering (SAXS) data in Figure 3-2. The crystalline phase shows a peak at 1.0 1/nm corresponding to a lattice spacing of 6.1 nm, which is roughly double the length of the LC, as calculated by the Gaussian model in Figure 3-3; on the other hand, the nematic phase shows no peak at 1.0 1/nm. Furthermore, it shows no peak around 2 1/nm either, which is positive evidence against a smectic phase. There is, however, a peak in the Medium Angle X-ray Scattering (MAXS) data in Figure 3-4 at 14 1/nm corresponding to a spacing of 0.43 nm, which is roughly the width of the LC calculated with Gaussian model in Figure 3-3.

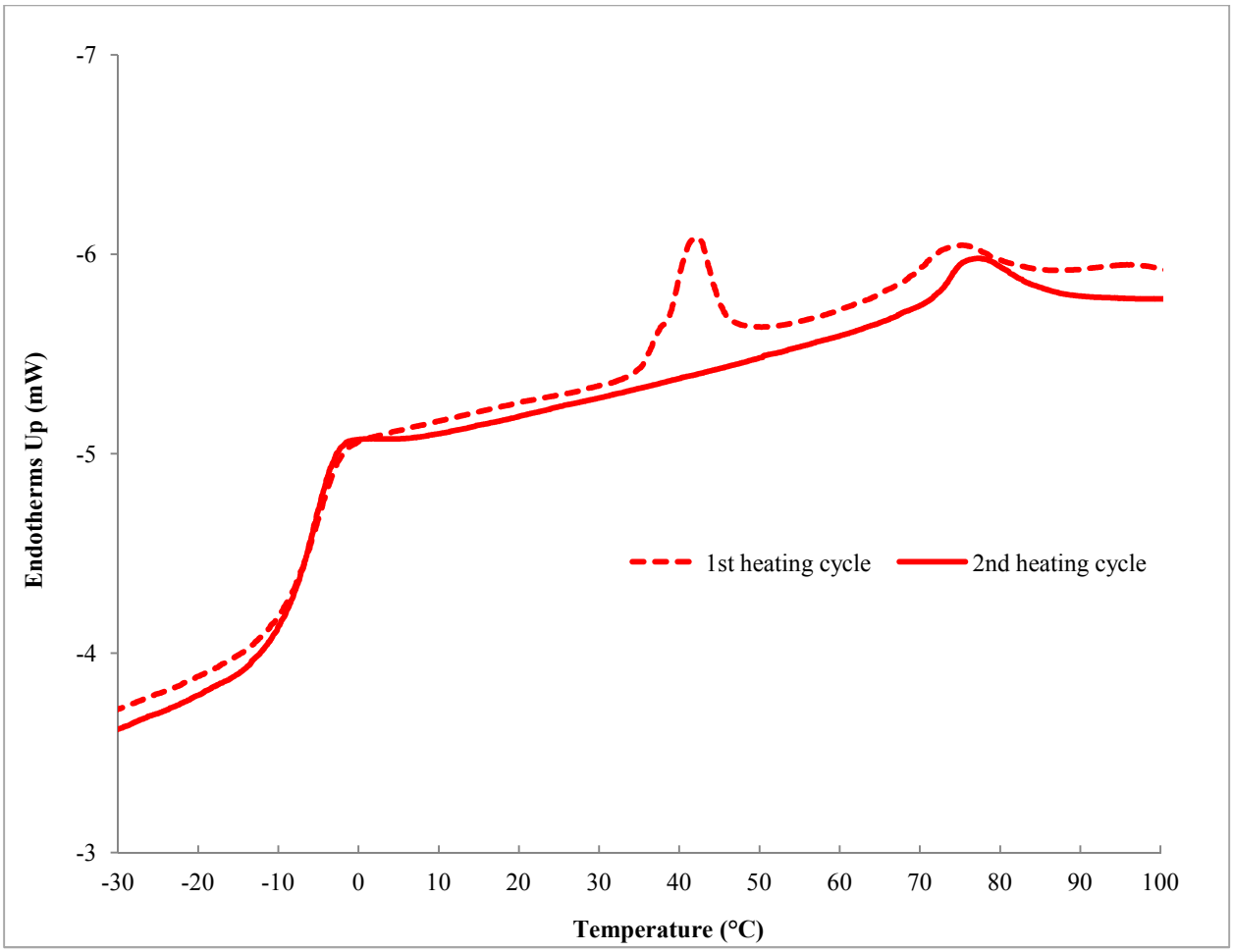

Figure 3-1. Differential Scanning Calorimetry (DSC) at 10 °C/min with 2 cycles on SCLCP 1 week after annealing.

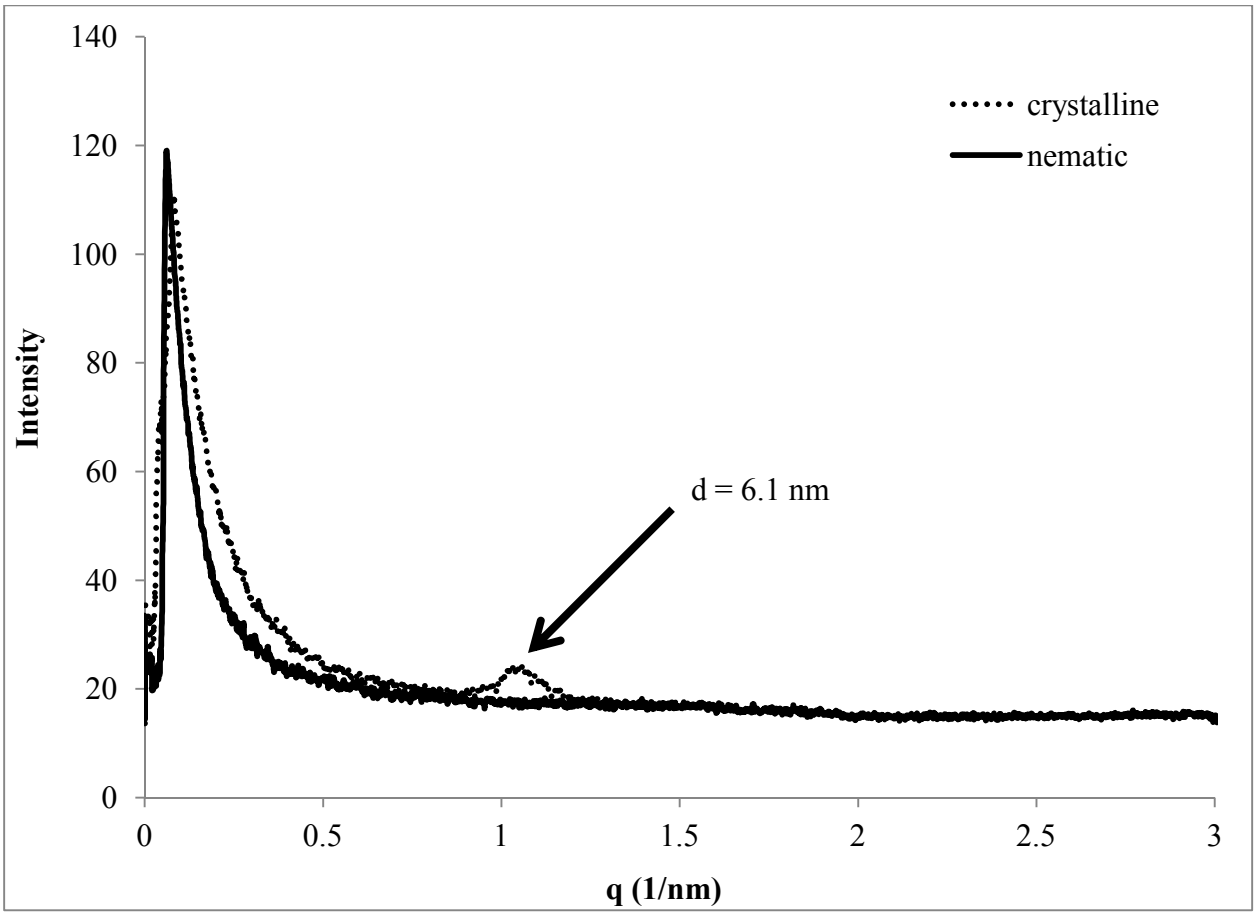

Figure 3-2. Small Angle X-ray Scattering (SAXS) diffractogram of crystalline and nematic samples of SCLCP .

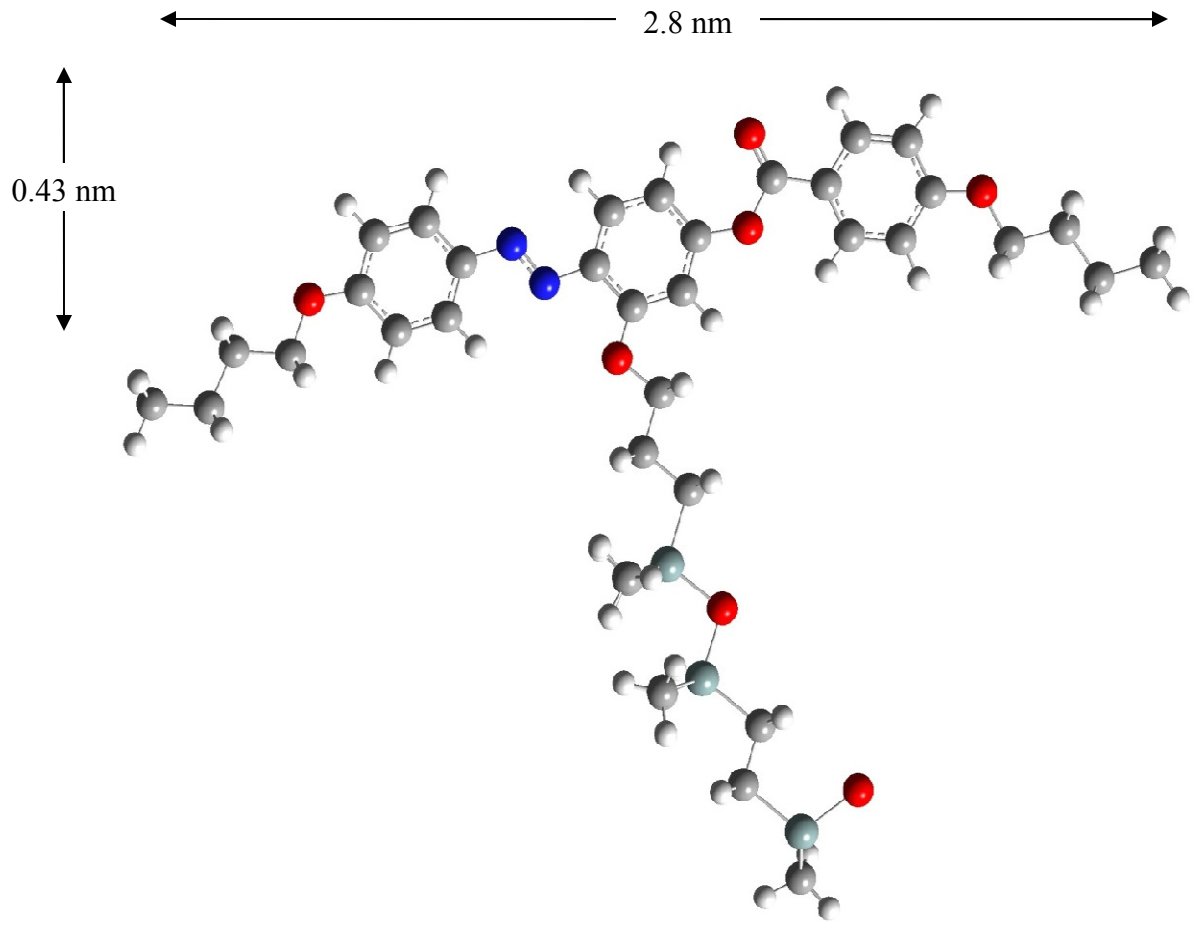

Figure 3-3. Gaussian model of the LCP. Gray is carbon, white is hydrogen, red is oxygen, blue is nitrogen, and blue-gray is silicon. The model is actually a very similar analog of the LCP because there is merely an Si-O single pond as opposed to a polymeric Si-O.

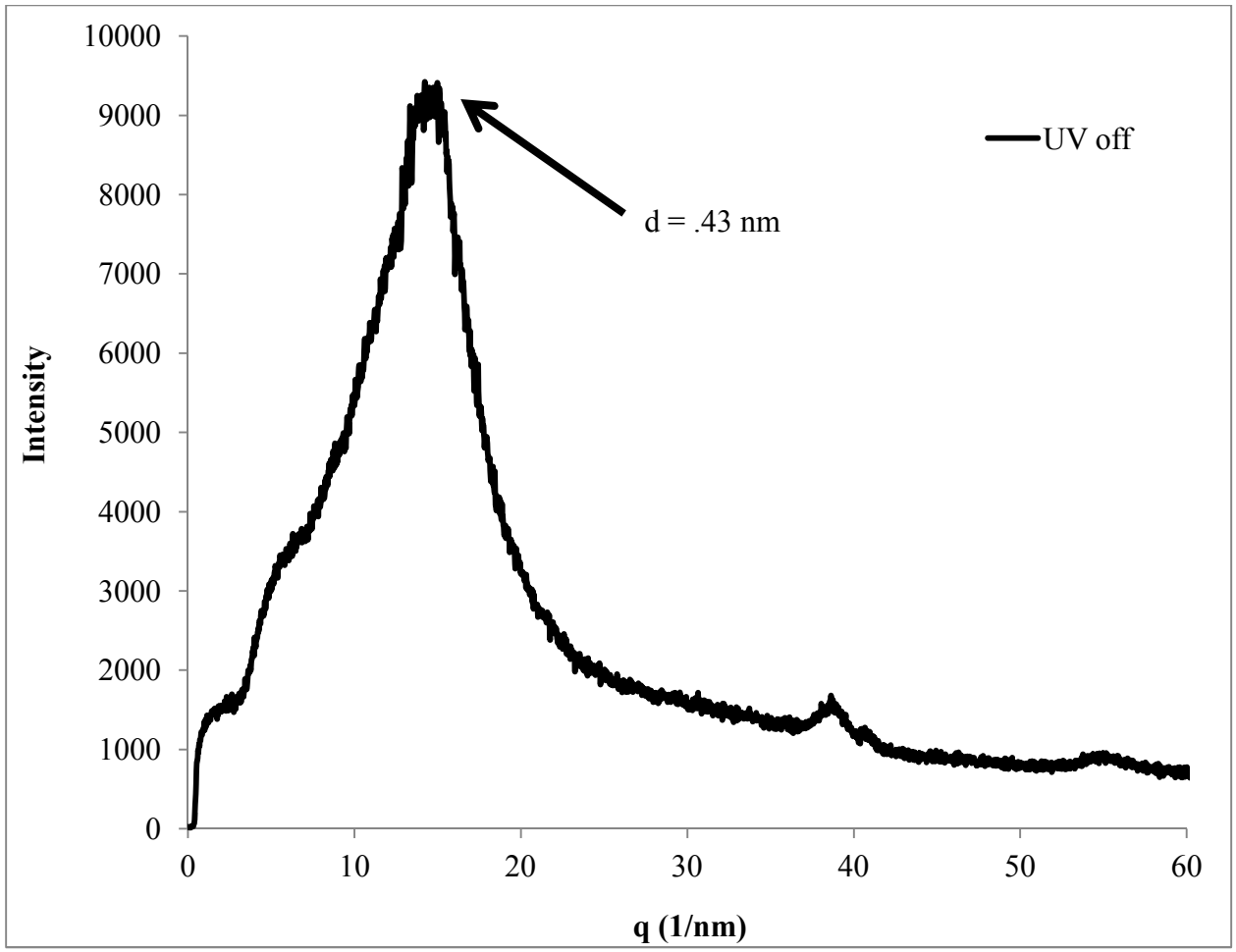

Figure 3-4. Medium Angle X-ray Scattering (MAXS) diffractogram of nematic SCLCP.

As for the LC phase itself, the POM image in Figure 3-5 is pink and green, which is due to the birefringence of an LC phase. It also shows a Schlieren texture with 2- and 3-point disclinations, which is positive evidence for a nematic LC phase. Furthermore, this nematic phase persists down to the T_g because the crystalline phase forms so slowly, thus making it a long-lived metastable phase. Additionally, the ordinary (n_o) and extraordinary (n_e) refractive indices and the birefringence (Δn) of a spin cast sample on glass were measured as 1.59, 1.66, and 0.07, respectively, using the anisotropic ellipsometry data in Figure 3-6 fit with a sample

thickness and two perpendicular refractive indices at an angle θ from the source. The parameters of this fit are in Table 3-1.

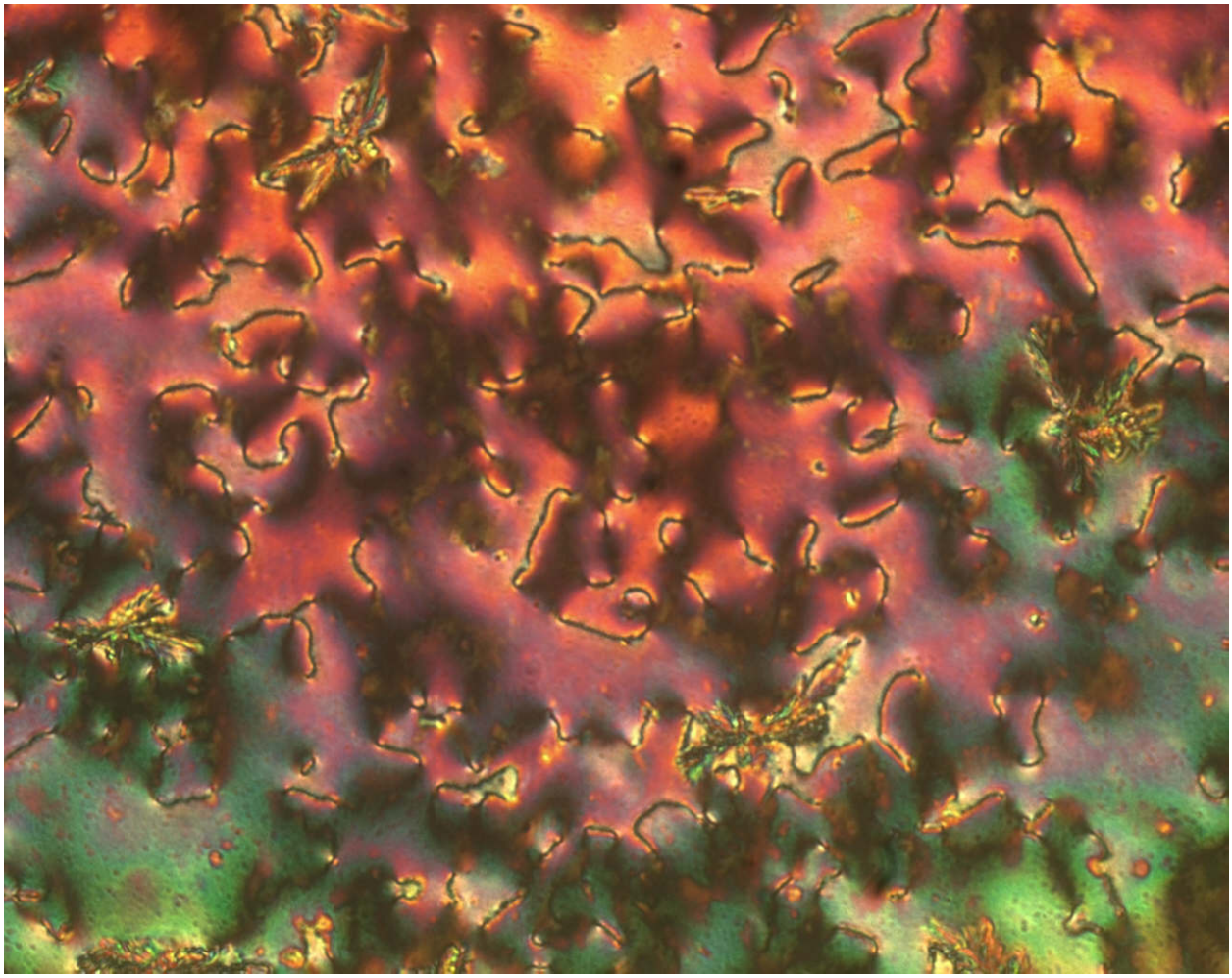

Figure 3-5. Polarizing Optical Microscopy (POM) image of SCLCP at a magnification of x50 showing a Schlieren texture with 2- and 3-point disclinations.

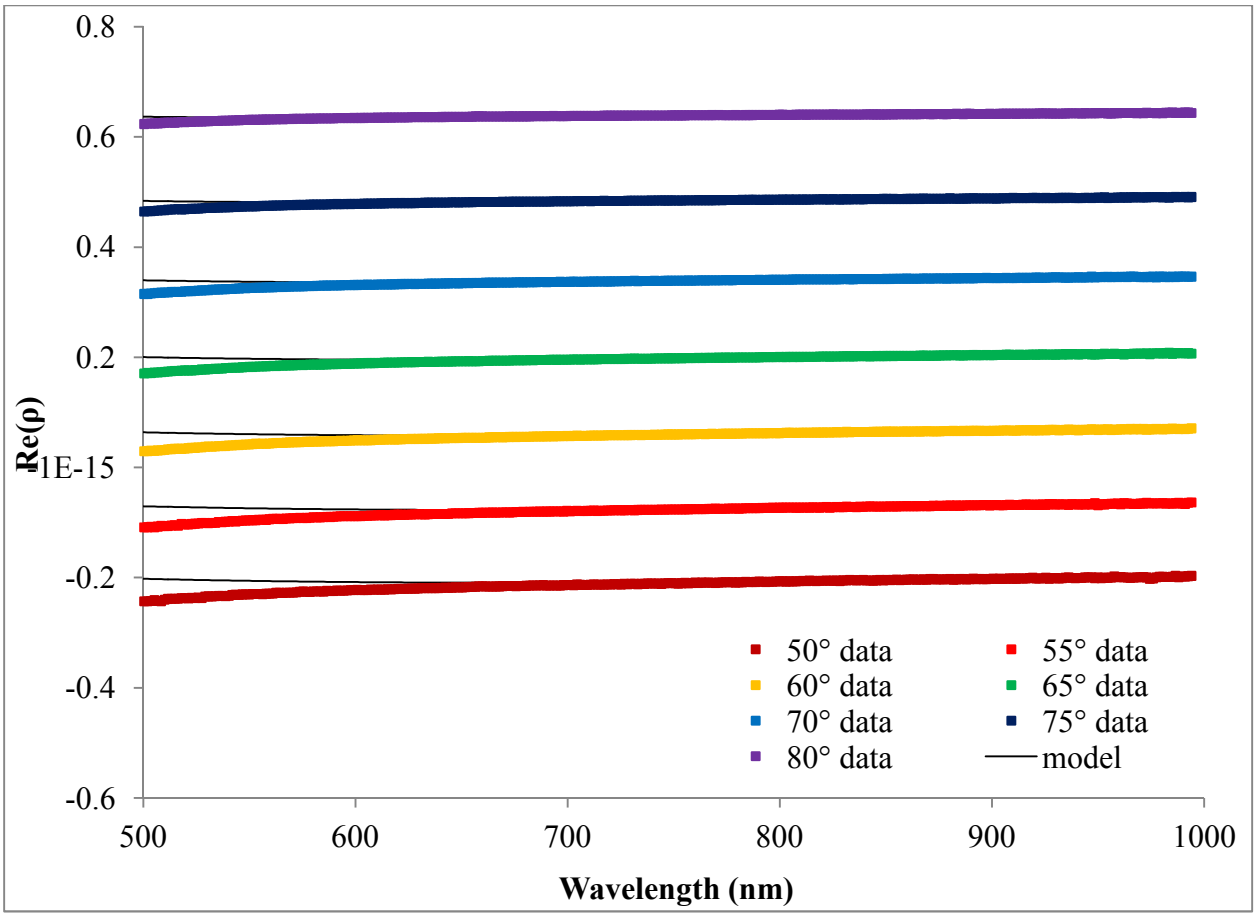

Figure 3-6 Real part of the complex ellipsometric ratio (ρ) fit with the parameters in Table 3-1.

Table 3-1. Fit parameters from ellipsometry data.

	Value	**Error**
n_e	1.6571	$\pm 1.3104 \times 10^{-2}$
n_o	1.5932	$\pm 3.8519 \times 10^{-2}$
thickness	112.8 nm	±2.1769 nm
θ	-1.2802°	±0.42611°
MSE	6.916×10^{-3}	

3.3. Photo-responsive characterization.

The SCLCP is photo-responsive because the azobenzene moiety can absorb a photon to promote an electron from the HOMO π orbital to the LUMO π* orbital, resulting in a conformational change of the azobenzene from the *trans* isomer, which is thermodynamically stable, to the *cis* isomer.[122] Figure 3-7 shows a UV-Visible absorption spectrum for the SCLCP, which has an absorbance peak in the near-UV and visible region from about 306-417 nm corresponding to this π to π* transition.

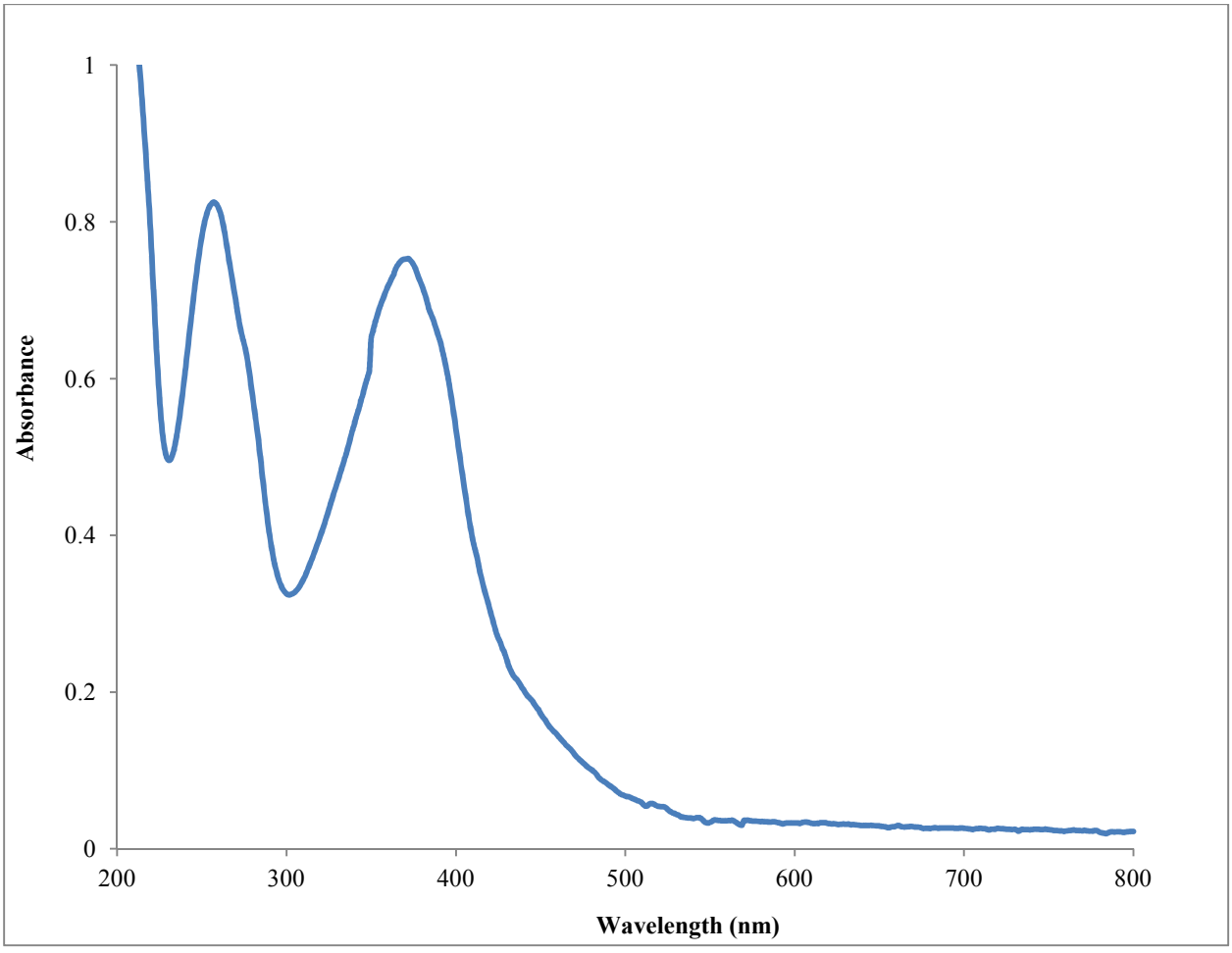

Figure 3-7. UV-Visible absorbance spectrum.

The SCLCP forms a nematic phase because the straight azobenzene and benzoate moieties in the *trans* conformation tend to line up to reduce free volume, as in the first schematic in Figure 3-8. Upon irradiation with UV light in this π to π* region, the azobenzenes' change from *trans* to *cis* disrupts the nematic phase of the SCLCP because, when they change to *cis*, they become bent and, therefore, cannot line up with each other, as in the second schematic in Figure 3-8.

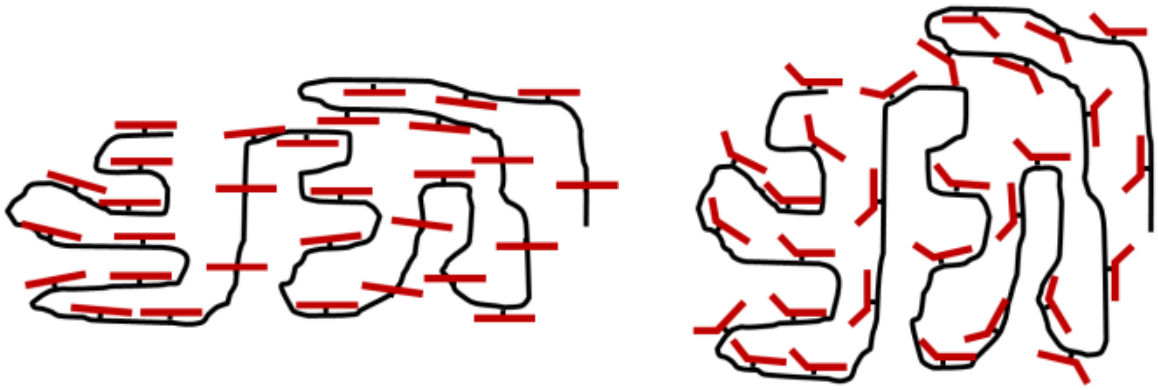

Figure 3-8. *Trans* to *cis* conformation change resulting in the nematic to isotropic phase change.

The effects of this nematic disruption can be seen in the MAXS data in Figure 3-9. With no UV light, it is the same as that in Figure 3-4; specifically, it has a peak at 14 1/nm corresponding to the width of the LC; however, with UV light, the intensity of that peak is reduced because a portion of the LC's are in the *cis* conformation.

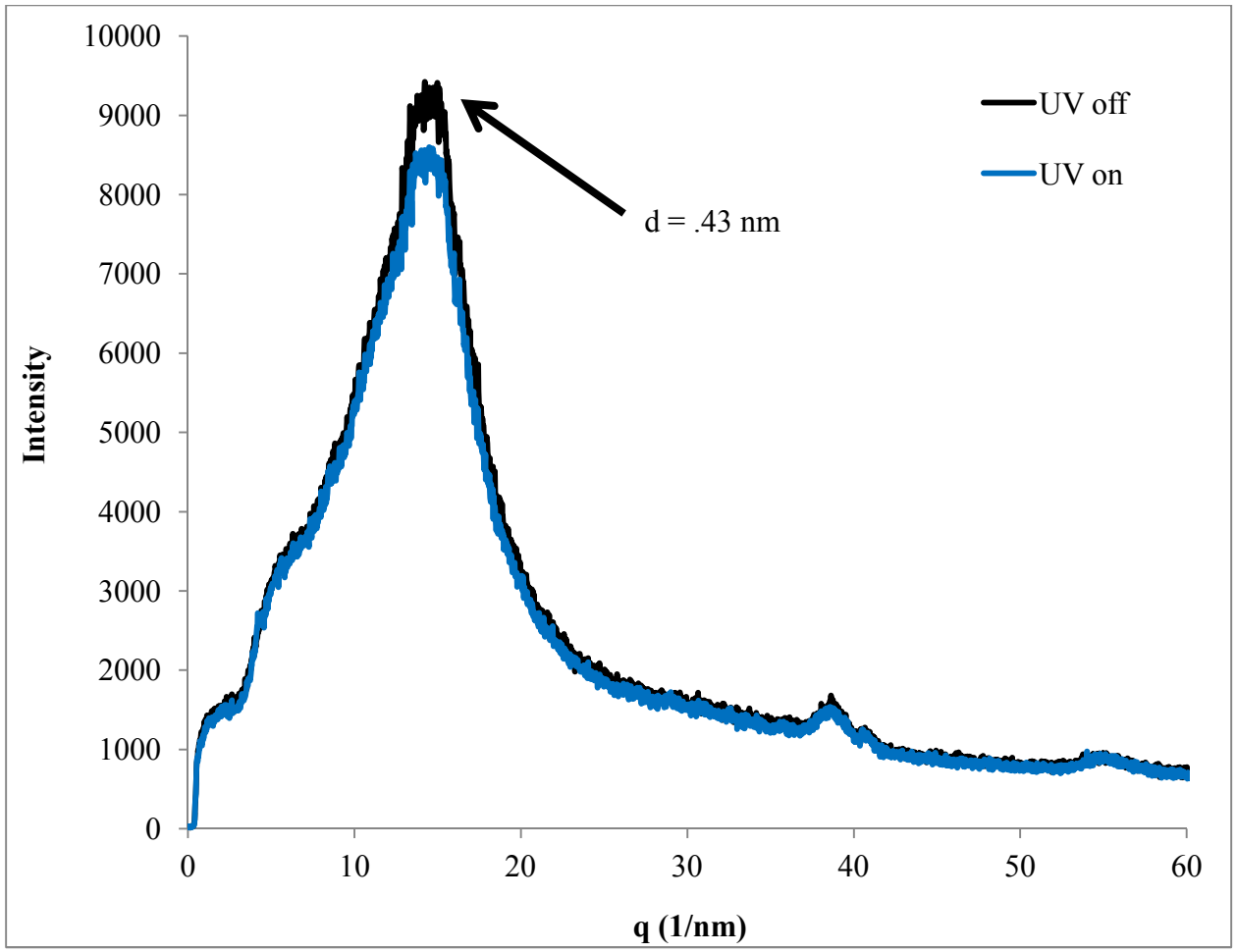

Figure 3-9. Medium Angle X-ray Scattering (MAXS) diffractogram of nematic SCLCP with UV off and UV on.

This nematic disruption was also monitored using POM with in-situ UV irradiation at 60 mW/cm^2. The first image in Figure 3-10 was taken with no UV light. At 0 s, the UV light was turned on, and the Schlieren texture was monitored with screen-capture software that recorded an image every couple of seconds. The last seven images in Figure 3-10 were taken every 5 s and show the disappearance of the birefringent Schlieren texture in the exposed area over a total of about 35 s. For these images, as well as the intermediate ones, the red, green, and blue 24-bit color intensities were evaluated for each pixel and summed over the entire picture for an overall color intensity. This color intensity is plotted as function of time in Figure 3-11. The decrease in

birefringence first exhibits a linear regime, producing data similar to that of previous photo-responsive nematic systems,[81, 130-144] with a rate of 1.0×10^{7} intensity/s and finishes with an exponential regime with a time constant of 4.6 s. The rate in the linear regime can be converted to a traditional rate of 1.9×10^{-11} mol/s by applying Equation 3-1, which uses the initial volume of the film divided by the initial color intensity as a scale factor:

$$r = r_I \frac{A_i h_i}{I_i} \frac{\rho}{M} \qquad 3\text{-}1$$

where r is the rate in mol/s, r_I is the rate in intensity/s, A_i is the initial area of the film calculated as 2.4×10^{-4} cm^2 from the manufacturer's technical data, h_i is the initial height of the film estimated at 13 μm using a Michel-Levy Plot, I_i is the initial intensity of the film found to be 2.1×10^{8}, ρ is the density of the film estimated to be 0.95 g/cm^3, and M is the molar mass of the SCLCP repeat unit calculated to be 753.16 g/mol. The film height was estimated with a Michel-Levy Plot because, even though the film height was uniform in the small viewing window of the microscope, it was non-uniform across the entire sample, so direct measurement in the specific area of the POM images would have been difficult. Basically, a Michel-Levy Plot is a graphical link between film thickness, birefringence, and viewed POM color. Given two of these, the third can be estimated.

It was a somewhat counterintuitive result to have two regimes for the SCLCP's isotropization. Because the azobenzene's isomerization is uni-molecular, it is expected to follow 1st-order kinetics with rates on the order of minutes to hours,[145] and indeed, this was, most likely, the case given the previous photochemical characterization of the LC.[52] However, the SCLCP's isotropization is not necessarily linearly correlated with the azobenzene's isomerization. The bent *cis* LC moieties act as bulky impurities in the nematic phase to lower its T_{iso} [64] and to effectively destroy it at a given temperature below the original T_{iso}. Once the UV light was

introduced, the nematic phase was destabilized, and the linear regime followed by the exponential regime is consistent with the kinetics of a nematic phase with a distribution of domain sizes that is supersaturated with *cis* azobenzene impurities.[126, 127] Figure 3-10 actually shows isotropization starting from the domain boundaries and moving inward, leading to linear kinetics, followed by convergence of the growing isotropic domains – ie., disappearance of the nematic domains – leading to exponential kinetics. Because there is a distribution of nematic domain sizes in the beginning, the individual domains disappear at different times, smaller ones followed by larger ones. Coincidentally, the camera is centered on a cluster of smaller domains, which disappear faster and produce the artifact of isotropization seeming to start in the center of the screen. The fourth image in Figure 3-10 then shows some of the smaller nematic domains in the center as they disappear, signifying the transition to the exponential regime whereby the growing isotopic domains begin to coalesce and stop growing. A decreasing number of growing isotropic domains means a decreasing isotropization rate, which corresponds to the exponential kinetics.

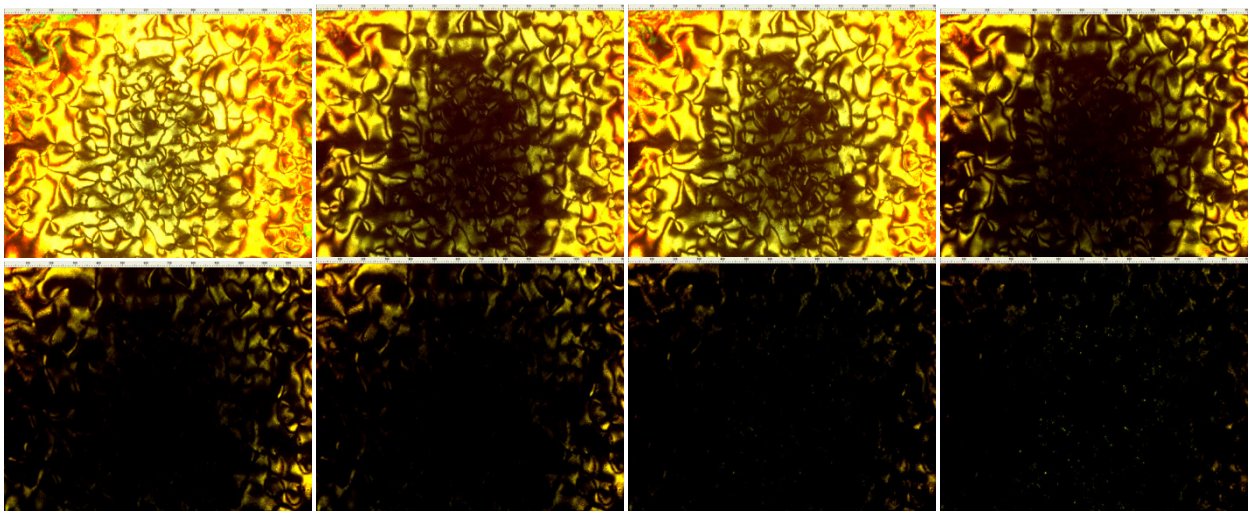

Figure 3-10. Polarizing Optical Microscopy (POM) at a magnification of x50 of SCLCP with UV irradiation. The first picture was taken before the UV light was turned on, and it shows a nematic Schlieren texture with 2-, 3-, and 4-point disclinations. The next pictures are from 5-30 s and show the nematic phase disappearing, and the last picture is at 35 s and shows the nematic phase almost completely gone.

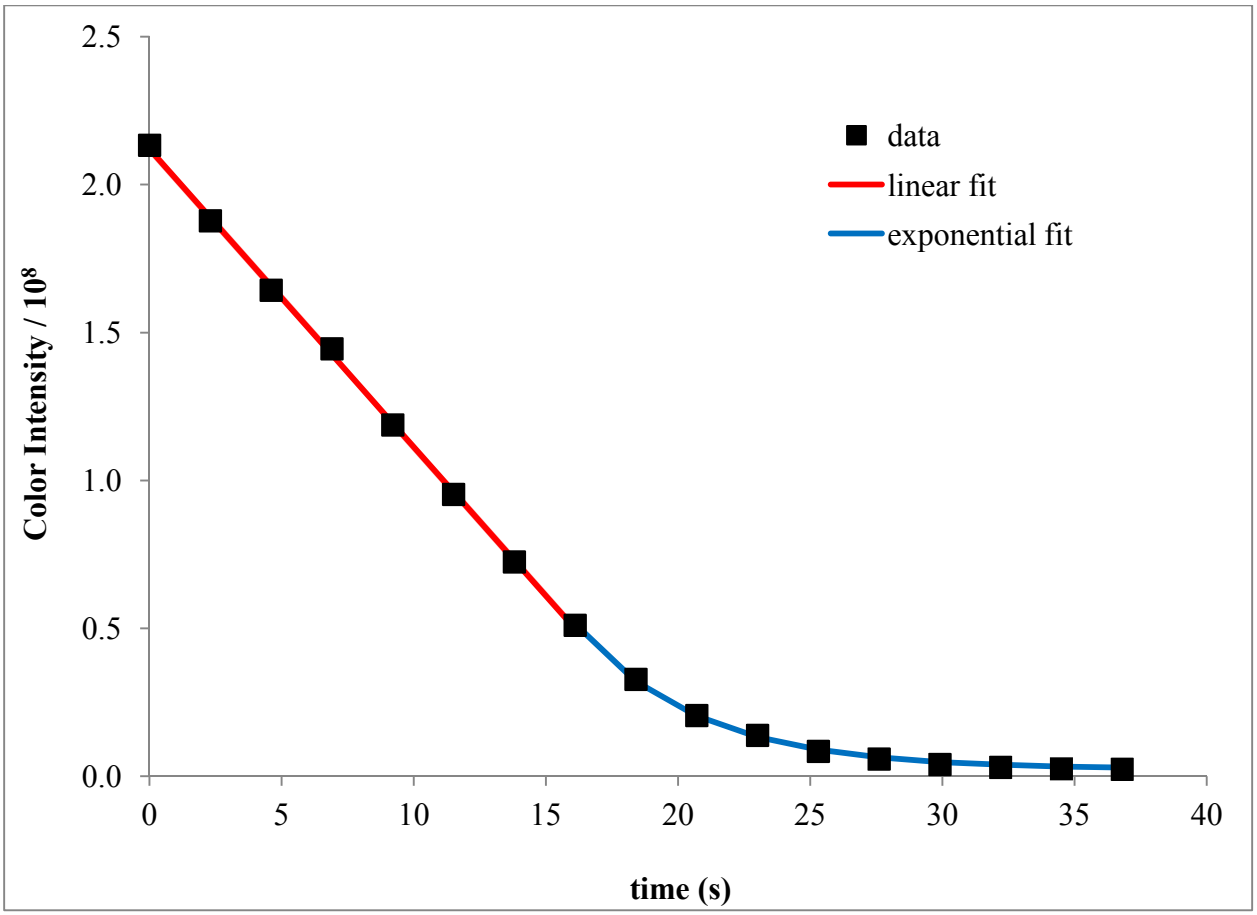

Figure 3-11. Integrated color intensity from Polarizing Optical Microscopy (POM) images. The first portion has a rate of 1.0×10^7 intensity/s and a linear r^2 of 0.9995, and the second portion has an exponential time constant of 4.6 s and an r^2 of 0.998.

4. Oscillatory Shear Rheometry of LCP

4.1. Experimental

Instrumentation

OSR was performed on a Rheometrics ARES strain-controlled rheometer using a parallel plate geometry. The bottom plate was made of copper with a thin chromium-based coating by Micro-E, Electrolizing Inc., and its temperature was controlled by an ARES Peltier control system. The upper plate was an ARES UV Curing accessory, which consists of a 20 mm diameter transparent quartz plate. The plate is housed within a tube containing a 45° mirror onto which light is incident and transmitted to the sample. In situ UV irradiation was carried out with a Dymax Blue Wave 200 with a Thorlabs, Inc. FGUV W53199 UV filter. Finally, UV light intensity was measured with a Dymax ACCU-CAL 50 radiometer.

Procedure

The rheometry experimental apparatus was set up according to the schematic in Figure 4-1. Following that, the UV light was aligned with the mirror on the upper rheometer plate at a gap large enough for the radiometer head to fit (~4 mm), and the intensity of the UV light coming through the quartz plate was measured. The gap was then set to around 0.2 mm, and the UV light was re-aligned. Next, approximately 80 mg of crystalline LCP was placed on the bottom plate at room temperature. The plate was then heated to 80°C for several minutes and sheared to completely melt the crystalline phase of the LCP. Subsequently, the gap was set to 0.28 mm in order to completely fill the parallel plate geometry. Prior to measurement, auto-tension as well as manual gap adjustment were used to minimize tension or compression on the sample. Finally, a series of temperature sweeps, time sweeps, amplitude sweeps, frequency

sweeps, and small angle oscillatory shear (SAOS) experiments, all with UV off and with UV on, were performed.

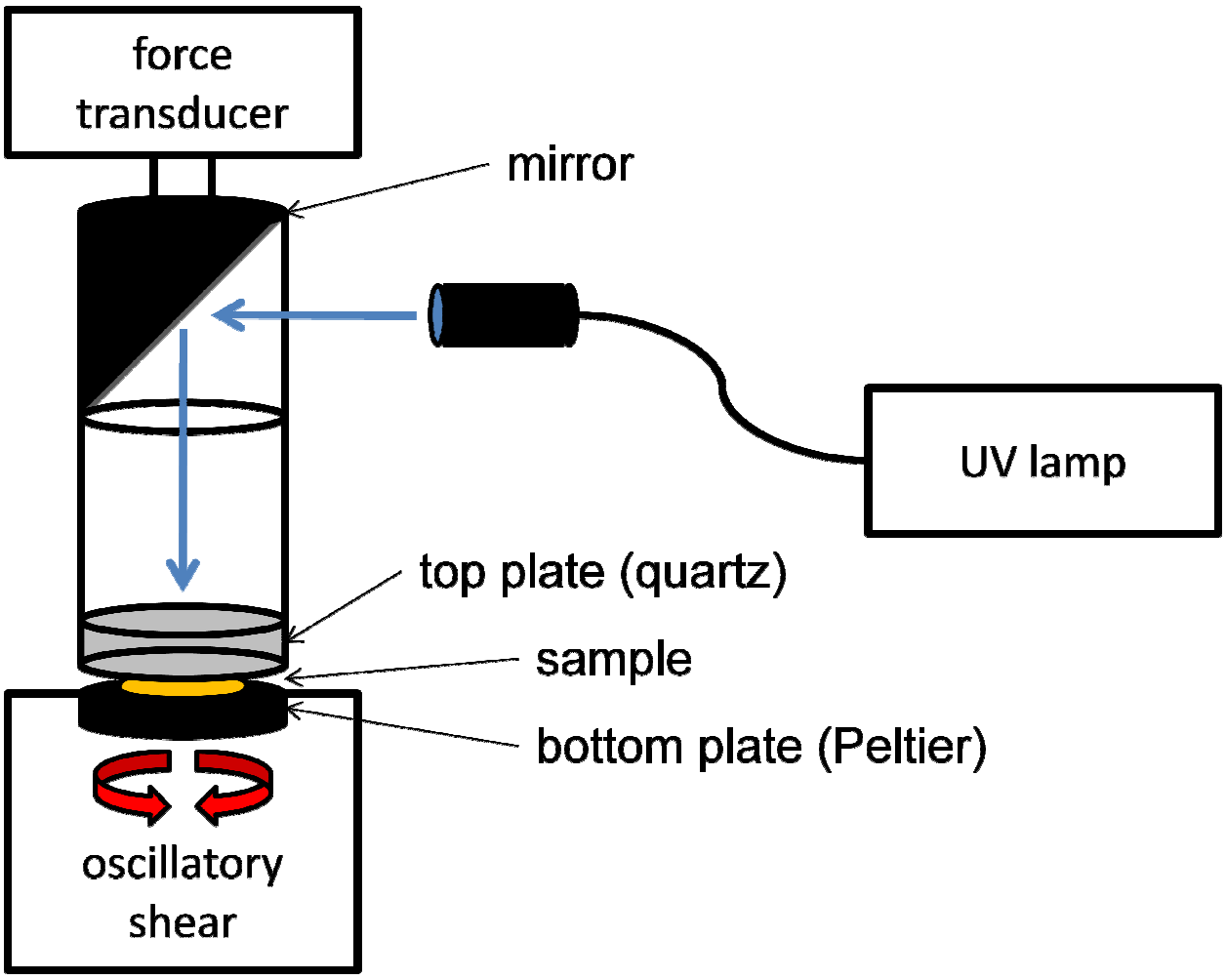

Figure 4-1. Schematic of rheometry experimental apparatus.

4.2. Oscillatory Shear Rheometry Conditions

Parallel plate OSR with in situ UV irradiation was a convenient way to observe the reversible modulus switching in real time. The UV light intensity penetrating the upper quartz plate to the top of the sample was 125 mW/cm^2, which was more than enough to execute the

nematic to isotropization quickly. With the exception of the time sweeps, where the kinetics of isotropization were measured, the various UV off and UV on tests were separated by several minutes in order to ensure the isotropization had reached steady state. Since illumination is controlled independently of the rheometer, the sample temperature as well as the other experimental parameters were easily controlled without having to change any parts or reload the sample.

Still further, the rheometer's gap, and thus the sample's thickness, were easily and precisely controlled. The rheometer gap was between 0.25 and 0.28 mm for all tests studied, which is small enough for appropriate thermal equilibration and UV penetration but large enough to produce a measurable mechanical signal. Still, the transducer's signal range represented the range of accessible experimental conditions. At higher temperatures, lower frequencies, or lower strains, the torque minimum of the transducer was approached or passed, and at lower temperatures, higher frequencies, or higher strains, excessive compliance was approached or exceeded. Excessive compliance occurs when the transducer's strain is more than 70% of the total strain, thus limiting the actual strain attained by the sample as well as adding error to the data due to the low signal coming from the sample.

4.3. Linear Viscoelastic Strain Regime Determination

Strain amplitude sweeps were used to establish the linear visco-elastic strain regime (LVE) of the material under the given conditions. Figure 4-2 shows amplitude sweeps at a) 50 ºC, b) 25 ºC,[†] c) 5 ºC, and d) 0 ºC. For all cases above 0 ºC, regardless of whether the UV irradiation is present, G" is constant over the entire range of strains probed, and at 0 ºC, G" is relatively constant with some fluctuations due to the corresponding low strains values. As for G',

[†] The data in b) is from a different day and with about half the sample gap as the rest of the data in the paper.

in Figure 4-2a and Figure 4-2b, it is also relatively constant with some fluctuations at low strains until it smoothes out at moderate strains and then starts to decrease at about 2% strain in Figure 4-2a and 1.5% strain in Figure 4-2b. In Figure 4-2c, G' is constant across all of the strains achieved by the transducer, and in Figure 4-2d, G' is constant with some fluctuations up to about .084%.

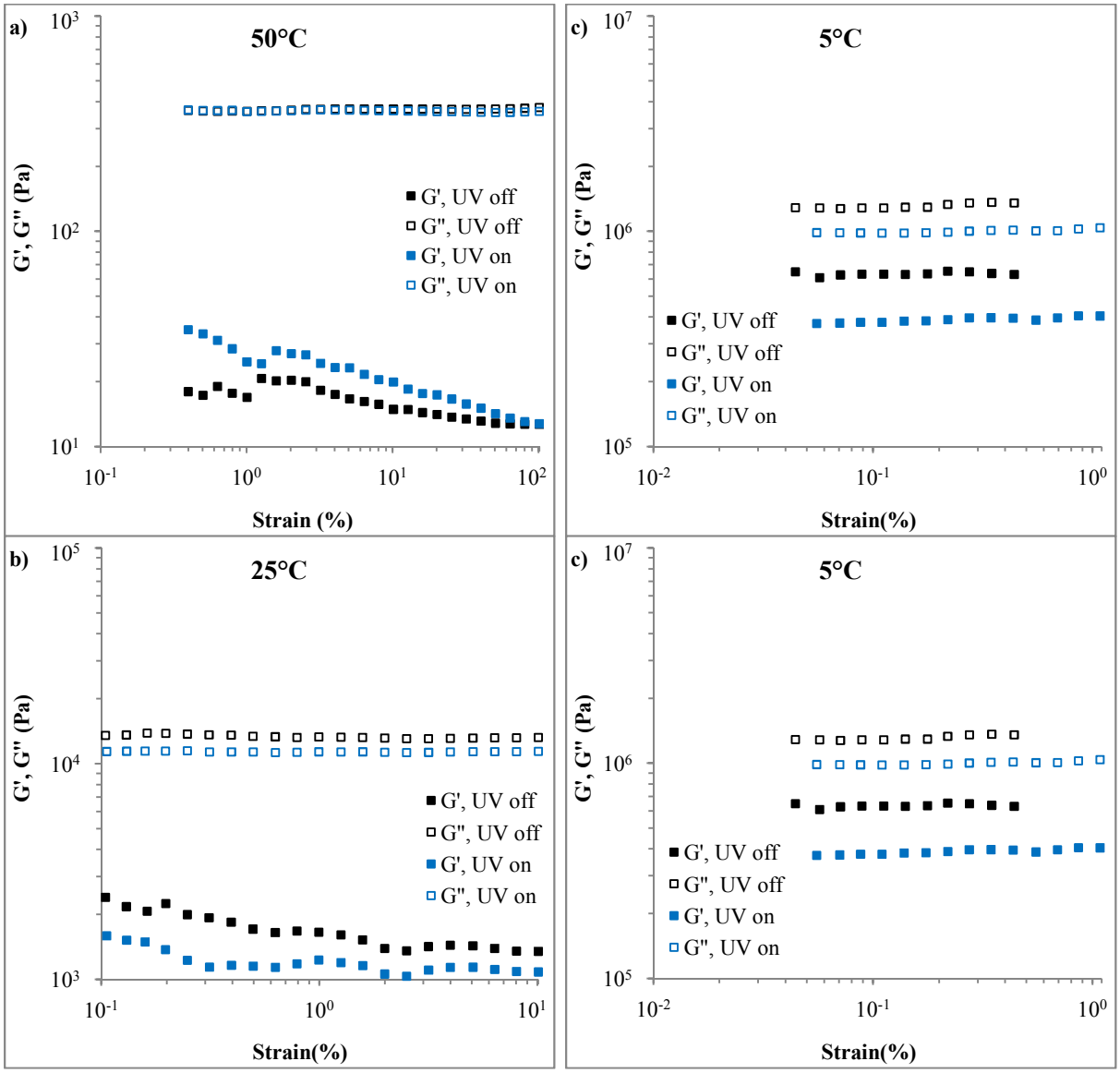

Figure 4-2. Amplitude sweeps with both UV off and UV on at 10 rad/s and a) 50ºC, b) 25ºC,† c) 5ºC, and d) 0ºC. In a), the G" values for UV off are covered by those for UV on because they are very close.

From the amplitude sweeps, the LVE regime was established, and linearity in G' and G" was confirmed with the Lissajous plots in Figure 4-3. Figure 4-3a was at 50°C and 1% commanded strain, Figure 4-3b was at 25°C and 1% commanded strain, Figure 4-3c was at 5°C and .437% commanded strain, and Figure 4-3d was at 0°C and .084% commanded strain. Under all of the conditions tested and for both UV off and UV on, the Lissajous plots were elliptical, which is more evidence that the material is, in fact, in the LVE regime. Furthermore, the plots in Figure 4-3a and Figure 4-3b are dominated by the viscous component, that is they are mostly round and show little linear character. The plots in Figure 4-3c and, even more so, in Figure 4-3d have a strong elastic component, that is the ellipse is tilted due to the strong linear contribution.

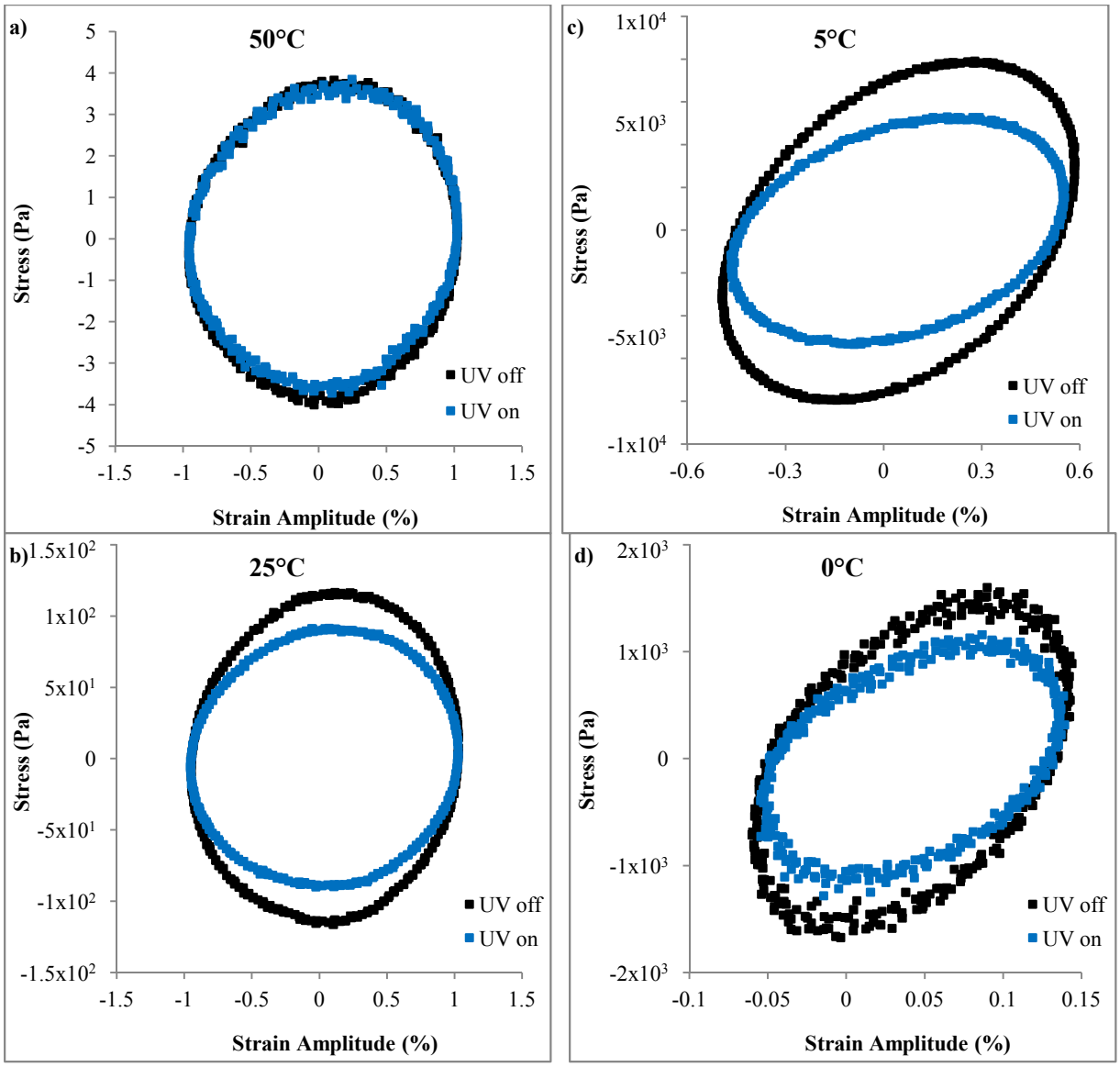

Figure 4-3. Lissajous Plots for both UV off and UV on at 10 rad/s and a) 50ºC, b) 25ºC, c) 5ºC, and d) 0ºC. The elliptic forms in all of the plots are evidence that the material is in the LVE strain regime.

4.4. Thermal and Temporal Characterization

With the LVE strain regime established within the functional temperature range of the material, thermal and temporal characterization was performed with temperature and frequency sweeps, respectively. Figure 4-4 reports temperature sweep data with both UV off and UV on

from -5 °C to 80 °C at 5 °C/min and an applied frequency and strain amplitude of 10 rad/s and 1%, respectively. Even though 1% strain was commanded, the actual strain was reduced at the lowest temperatures because of instrument compliance. The data over temperatures ranging from T_g to T_{iso} (Figure 4-4a) exhibit moduli (G' and G") which vary by 6 orders of magnitude due to the concomitant increase in free volume of the LCP. At high temperatures (T > 50 °C), the material exhibits liquid-like behaviour with G' > G", and the moduli are nearly independent of temperature. In this regime, the difference in G" between UV off and UV on is quite small, due to relatively less order in the nematic phase near T_{iso}.[64, 79] Between 50°C and around 2°C, the viscosity of the material increases significantly, as G" and G' increase by 4 orders of magnitude (Figure 4-4a). At room temperature and below, a significant difference in moduli between UV off and UV on develops (Figure 4-4b). These differences in G' and G" achieve maximal values of 44% and 23% at 4.7°C and 5.6°C, respectively. In this temperature range, a crossover to solid-like behaviour with G' > G" is observed with decreasing temperature as the material transitions from a viscous liquid to a glassy solid. Defining T_g as the crossover in G' and G", we find values for T_g of 2.2 °C and 0.3 °C for UV off and UV on, respectively. At even lower temperatures G" goes through a maximum at 0.6°C and -1.6°C for UV off and UV on, respectively, and decreases as the material is cooled further. These results show that UV light significantly decreases the T_{iso} of the LCP so that, under ambient temperature conditions, the application of UV light destroys the nematic phase of the LCP. Finally, below -2.5°C, the difference between G' for UV off and UV on again vanishes, demonstrating that, below T_g, the polymer chains are insufficiently mobile to rearrange upon UV irradiation.

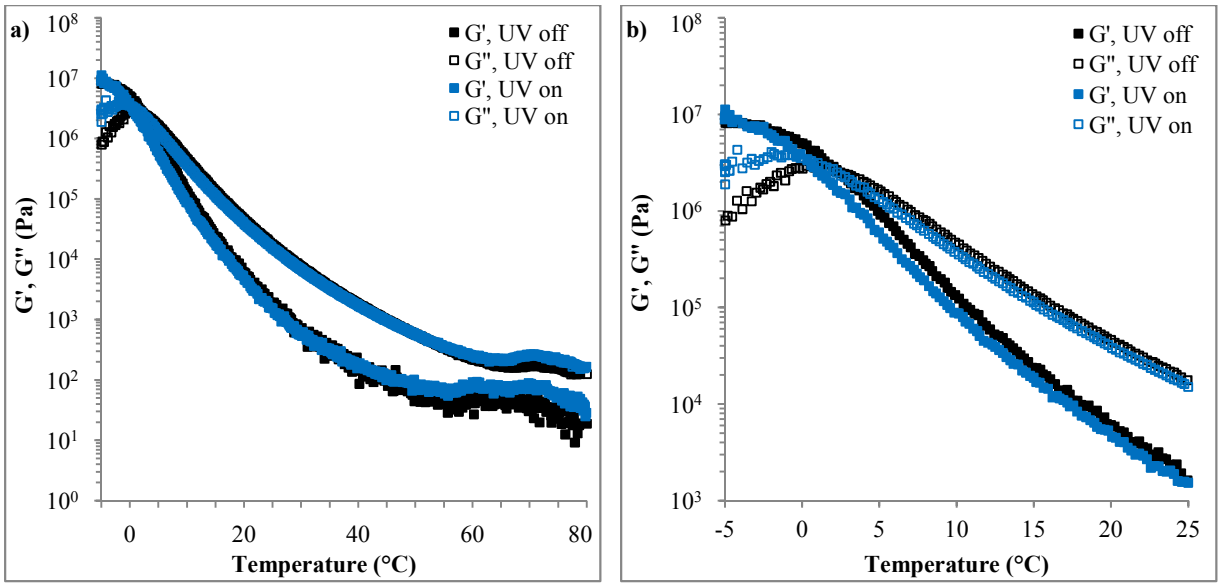

Figure 4-4. Temperature sweeps with both UV off and UV on at 5°C/min, 10 rad/s, and 1% commanded strain a) from 80ºC to -5ºC and b) zoomed in from 25ºC to -5ºC.

The results of the temporal characterization fit nicely with that of the thermal characterization and the principle of time-temperature superposition.[146] Figure 4-5 shows a series of frequency sweeps in the LVE strain regime at a) 50°C, b) 25°C, c) 5°C, and d) 0°C for both UV off and UV on. At 50°C and 25°C and above 1 rad/s, G' and G" for UV off and UV on exhibit power law behaviour, as in Equation 4-14-14-14-14-14-14-1,

$$\log G = m \log \omega + b \qquad 4\text{-}1$$

where ω is the frequency of oscillation and m and b are the slope and intercept, respectively, of the linear fit on log-log axes. Table 4-1 lists the parameters from all of the power fits. The slopes and intercepts for UV off and UV on were almost identical; however, temperature affected the slopes for G'. At 50°C the slopes were below 1, but at 25°C, the slopes were above 1. On the other hand, all the slopes for G" were nearly 1. As the temperature continues to decrease toward the T_g, as in Figure 4-5c, G' and G" for UV off and UV on still increase qualitatively as a power

law at low frequencies but become concave downward at high frequencies. In addition, G" goes through a maximum at 50 rad/s and 63 rad/s for UV off and UV on, respectively, and the material itself goes through a glass transition of sorts, where G' and G" cross, at 32 rad/s and 50 rad/s for UV off and UV on, respectively. Finally, Figure 4-5d at 0°C shows all the same trends as Figure 4-5c but shifted to lower frequencies because of the lower free volume in which the chains can rearrange upon deformation. There is the low frequency linear increase in G' and G", the higher frequency concave downward segment for G' and G", the G" maximum at 7.9 rad/s for both UV off and UV on, and the glass transition frequency at 4.0 rad/s and 6.3 rad/s for UV off and UV on, respectively. It is important to note that the glass transition frequency is greater than 10 rad/s at 5°C and less than 10 rad/s at 0°C because 10 rad/s was the condition used in all of the other OSR tests; this is why the T_g observed by OSR was between 0°C and 5°C.

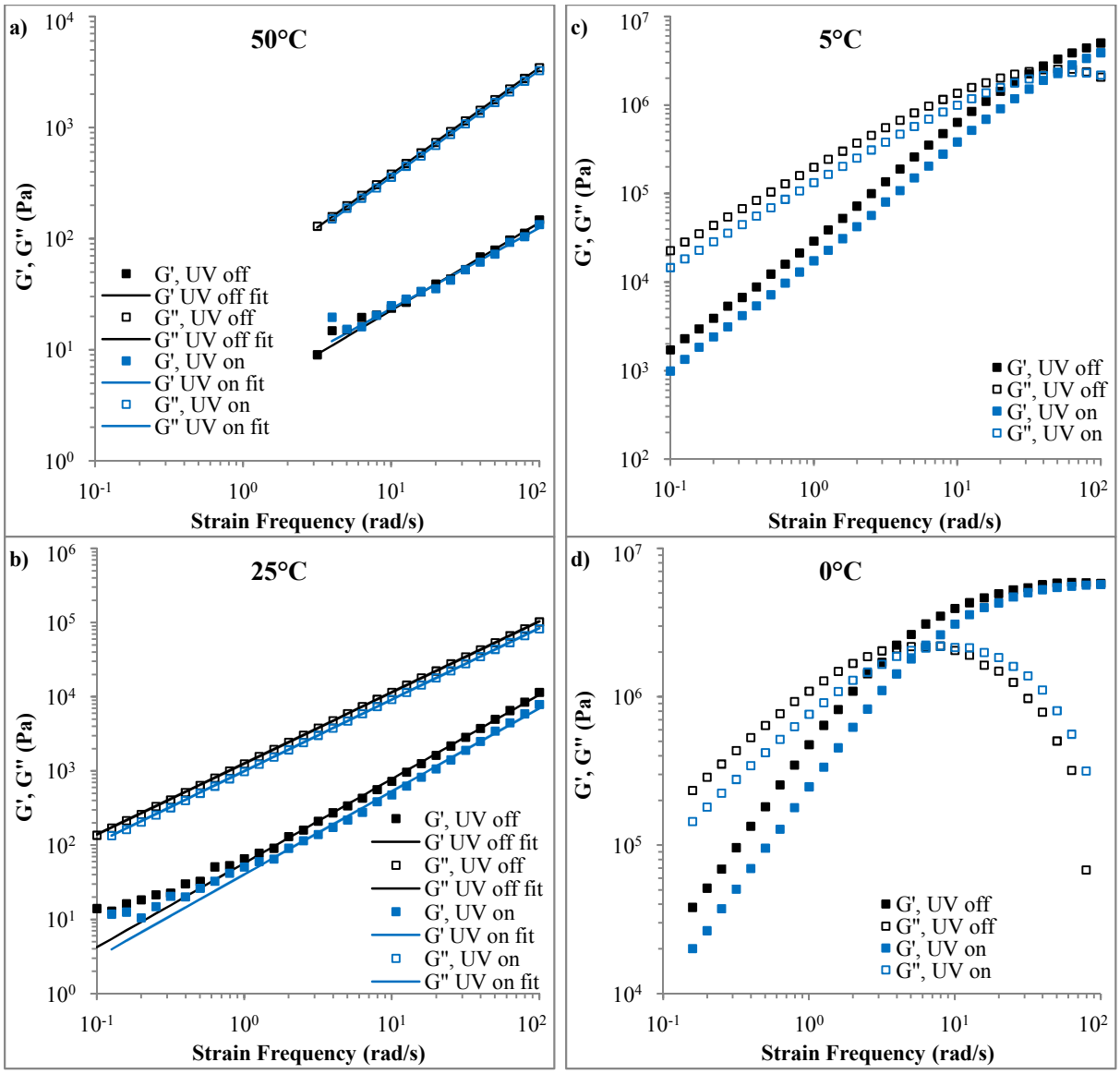

Figure 4-5. Frequency sweeps with both UV off and UV on in the LVE strain regime at a) 50ºC, b) 25ºC, c) 5ºC, and d) 0ºC. Both G' and G" in a) and b) were fit individually with the power law in Equation 4-1, the parameters for which are in Table 4-1.

Table 4-1. G' and G" power law fit parameters for 50°C and 25°C.

		50°C		25°C	
		UV off	**UV on**	**UV off**	**UV on**
G'	**m**	0.789	0.728	1.13	1.12
	b	0.6	0.6	1.8	1.6
G"	**m**	0.959	0.960	0.958	0.964
	b	1.6	1.6	3.1	3.0

To further demonstrate the equivalent thermal and temporal effects, time-temperature superposition was performed with the frequency sweeps in Figure 4-5 to produce Figure 4-6. G' and G" were shifted by eye with a single shift factor to 25°C for both UV off and UV on, and these shift factors are shown in Figure 4-7. They were then fit with the WLF equation shown in Equation 4-2 [146]

$$\log a_T = \frac{-C_1(T - T_{ref})}{C_2 + (T - T_{ref})} \qquad 4\text{-}2$$

where a_T is the shift factor at temperature T, C_1 and C_2 are the WLF constants, and T_{ref} is the reference temperature to which the data is shifted. To compare to other polymers, these 25°C WLF constants can be transferred to the UV off and UV on T_g's of the LCP using Equation 4-3 and Equation 4-4

$$C_1' = C_1 + \log a_{T_g} \qquad 4\text{-}3$$

$$C_2' = C_2 + (T_g - T_{ref}) \qquad 4\text{-}4$$

where C_1' and C_2" are the transferred WLF constants. Table 4-2 lists all the WLF constants as well as the T_g's from the Figure 4-4 and the shift factors used in the calculations. Compared to other polymers, C_1' is in between that of polydimethylsiloxane (PDMS) and the universal C_1', and C_2' is below that of PDMS and very slightly below the universal C_2'.[147]

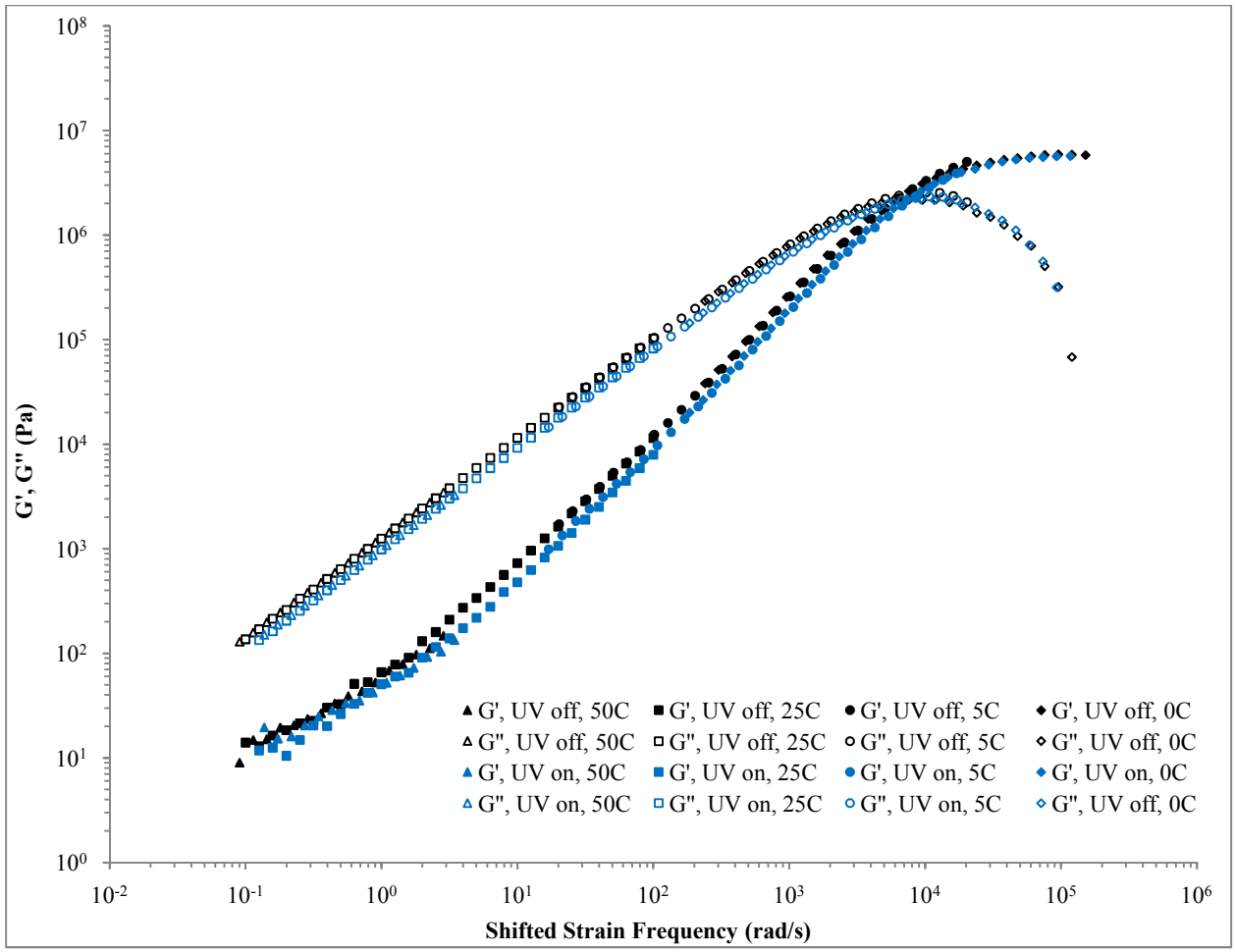

Figure 4-6. Time-temperature superposition of frequency sweeps shifted by eye to 25°C. Each of the four temperatures has a different symbol.

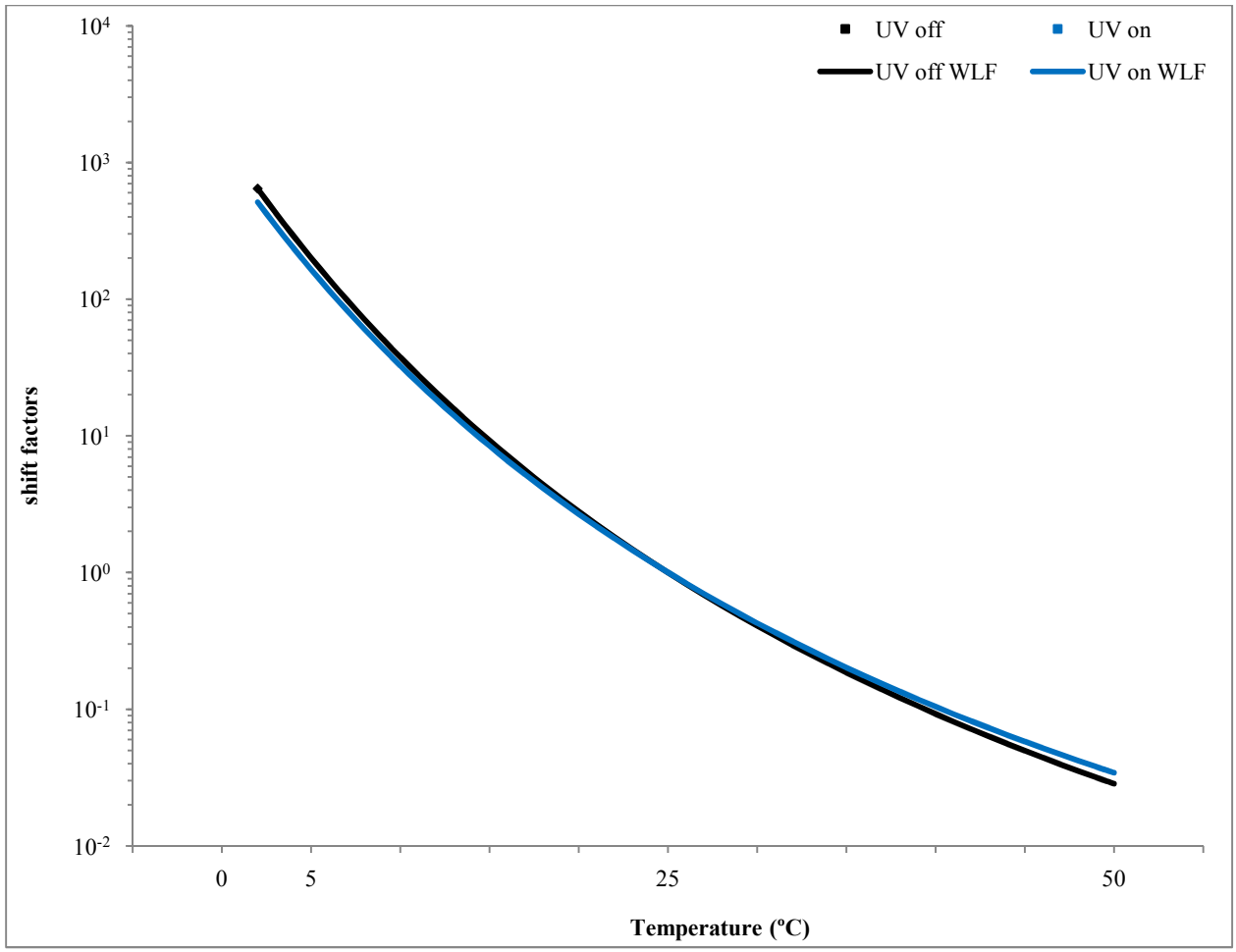

Figure 4-7. Shift factors from time-temperature superposition of frequency sweeps fit with the WLF equation in Equation 4-2.

Table 4-2. WLF parameters at 25°C from fitting of shift factors in Fig. 5 and WLF parameters translated to T_g.

	T_{ref} = 25°C		T_{ref} = T_g	
	UV off	**UV on**	**UV off**	**UV on**
C_1	6.00	5.60	8.77	8.62
C_2 (ºC)	72.2	70.5	49.4	45.9
Tg (ºC)	2.2	0.3	2.2	0.3
log a_{T_g}	2.77	3.01	0	0

4.5. UV Modulus Switching

With an understanding of the linear viscoelastic behaviour of the material, and the effects of photoresponsive behaviour on its temperature-dependent rheology, transient measurements involving UV switching were performed to understand the kinetics of the photoresponsive behavior. Figure 4-8 shows a series of time sweeps within the LVE strain regime at 10 rad/s and a) 60°C, b) 50°C, c) 25°C, d) 5°C, e) 0°C, and f) -5°C. Throughout each time sweep, the UV light was successively turned on and off, as indicated by the arrows in Figure 4-8, to observe the modulus switching. The data at 60 °C and at -5 °C shows no discernible response in G' or G" to UV light because they are too close to the T_{iso} and the T_g, respectively, of the material as well as because the torque and the strain on the material are outside the limits of the rheometer, illustrated by the large amount of scatter in the data. On the other hand, the data at all of the temperatures in between shows some response in G' and/or G". In particular, G" decrease significantly upon UV irradiation at 25°C, and both G' and G" show their largest decreases of 35% and 21%, respectively, at 5°C. This observation is in good accordance with the temperature sweeps in Figure 4-8, which also show maximum modulus differences around 5°C. Moving to the lowest responsive temperature, there is something interesting to point out in the response at 0°C. G' decreases significantly upon UV irradiation, just like at the other temperatures, but G" increases slightly; however, this can be easily explained by the previous thermal characterization. The complex shear modulus (G*) still does decrease, but the contribution from G" increases because 0°C is slightly below the T_g of the UV off material but slightly above the T_g of the UV on material, shown in Figure 4-4. Therefore, at 0°C, UV irradiation changes the material from a glassy solid to a viscous liquid.

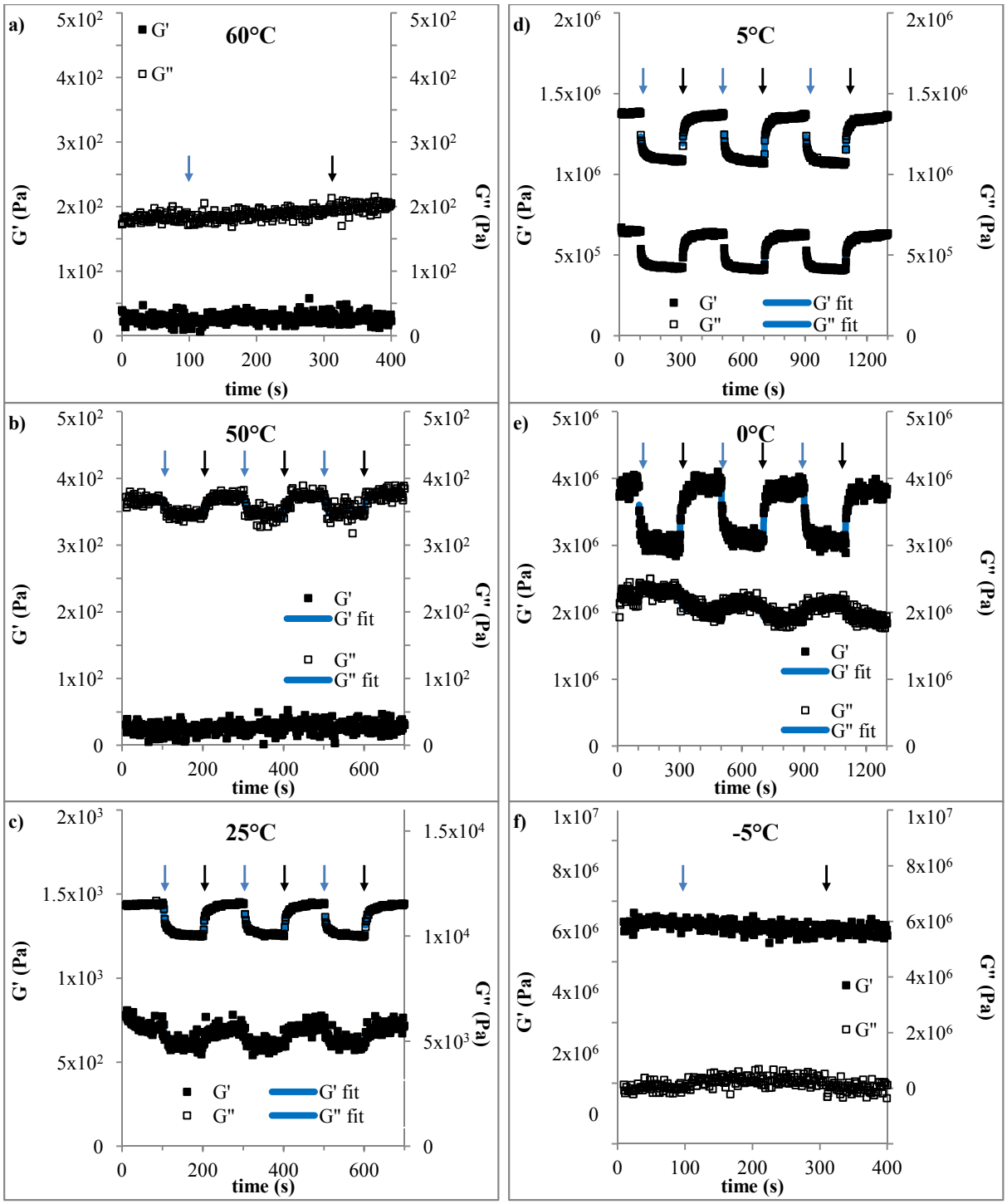

Figure 4-8. Time sweeps with UV modulus switching in the LVE strain regime at 10 rad/s and a) 60ºC, b) 50ºC, c) 25ºC, d) 5ºC, e) 0ºC, and f) -5ºC. The UV light was off at 0 seconds and successively switched on and and off again. Blue arrows indicate when the UV light was turned on, and black arrows indicated when the UV light was turned back off.

The final aspect of the UV modulus switching is the kinetics with which it occurs. UV irradiation lowers G' and G" because the azobenzene's *trans* to *cis* isomerization destabilizes the nematic phase of the material;[79] therefore, the kinetics is characteristic of a distribution of time constants. G' and G" in Figure 4-9b, Figure 4-9c, Figure 4-9d, and Figure 4-9e were fit with the stretched exponential in Equation 4-5 below:

$$\frac{G(t)-G_f}{G_i-G_f}=\exp\left(\left(\frac{t-t_s}{\tau}\right)^n\right) \qquad 4\text{-}5$$

where G is either G' or G", G_f is the steady state modulus long after the UV switch, G_i is the initial modulus before the UV switch, t is the time, t_s is the time of the UV switch, τ is the time constant of the photo-responsive transition, and n is the stretch factor. The data in Figure 4-9 were fit to Equation 4-5, as follows. First, G' and G" were averaged from the last 10 s before each UV switch. Second, each switch event was fit with τ, n, and t_s as adjustable parameters because the switching was done manually. Third, at each temperature, the data was split into three UV on segments and three UV off segments. Fourth, the three UV on segments were re-fit for overall τ_{on} and n_{on} values keeping the t_s values, and the three UV off segments were re-fit for overall τ_{off} and n_{off} values keeping the t_s values. The results of this fitting, in Figure 4-9, demonstrate how fast the modulus switching occurs because both the τ_{on} and τ_{off} values are quite small, though τ_{on} is less than τ_{off} at all temperatures because the UV on reaction is photo-driven but the UV off reaction is thermally driven. Moreover, the τ values start higher at 50°C and then decrease at 25°C and 5ºC before they increase again at 0ºC because, mathematically, the τ values are higher but the n values are lower at lower temperatures. As for the n values in Figure 4-9b, they are highest and closest to 1 at 50°C with n_{on} and n_{off} at 1.18 and 0.78, respectively, but then

they drop to between 0.38 to 0.54 at the lower temperatures, which is similar to other nematic LCPs,[79, 148-152] signifying a larger distribution of the τ's. Because the size of the distribution is changing, the average time constant of the distribution, rather than the τ from the fit, should be used to compare the τ's at different temperatures. This average time constants were calculated using Equation 4-6 and are shown in Figure 4-10

$$\tau_{avg} = \frac{\tau}{n}\Gamma\left(\frac{1}{n}\right) \qquad 4\text{-}6$$

where τ_{avg} is the average τ in the distribution of τ's. In Figure 4-10, τ_{on} is still less than τ_{off}, but both τ_{on} and τ_{off} increase monotonically with decreased temperature.

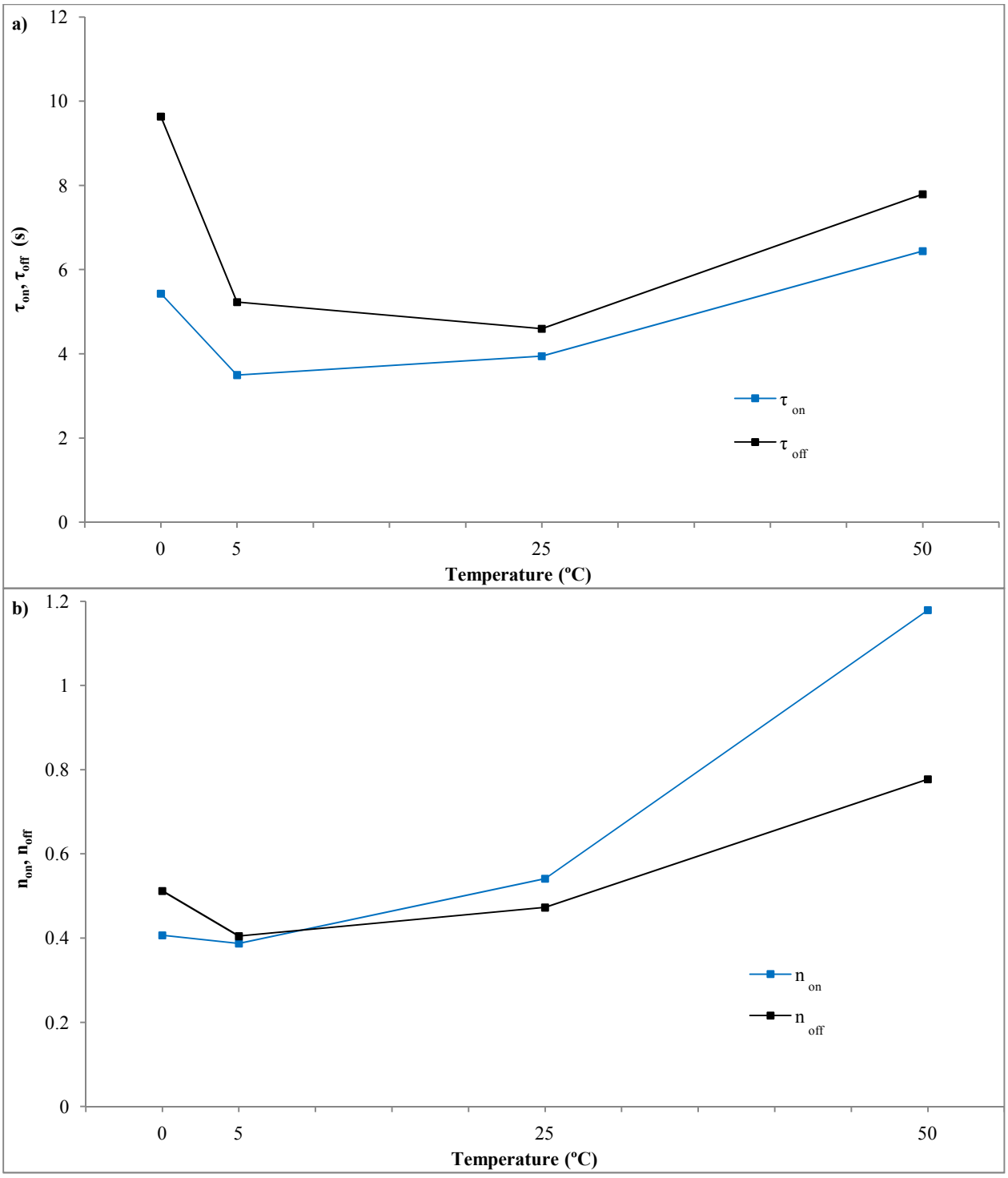

Figure 4-9. Stretched exponential a) τ and b) n parameter values from fitting of moduli cycles in UV switching experiments using . τ_{on} and n_{on} correspond to the modulii drops when the UV light was turned on, and τ_{off} and n_{off} correspond to the moduli recoveries when the UV light was turned back off. The points have been connected to aid the eye.

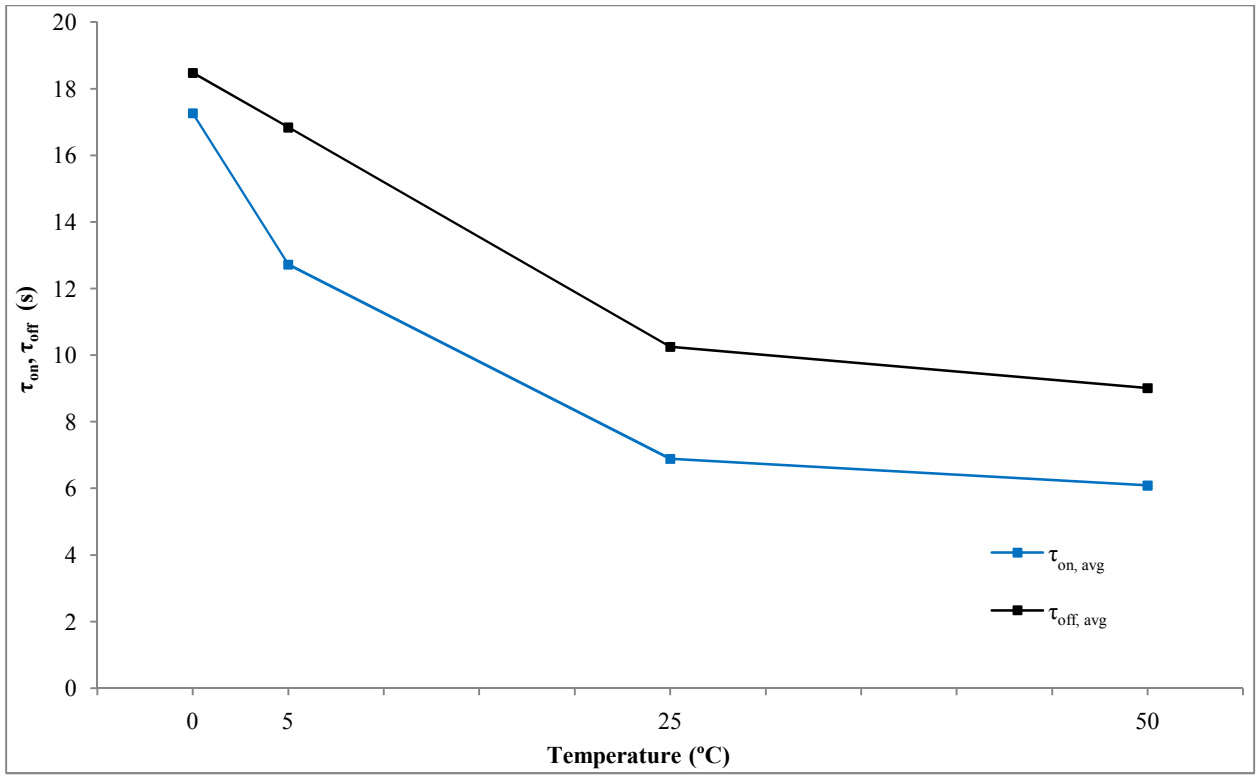

Figure 4-10. Average τ's calculated from stretched exponential fitting of moduli cycles in UV switching experiments.

5. Photo-responsive Liquid Crystal Triblock Copolymer Characterization

5.1. Instrumentation

Transmission Electron Microscopy (TEM) on a JEOL JEM2000FX was used to visualize the BCP morphologies. Small Angle X-ray Scattering (SAXS) on a Micro MAX Rigoko SAXS System with a Cu Kα source was used to identify BCP morphologies and to measure their characteristic spacings. Differential Scanning Calorimetry (DSC) on a Thermal Advantage (TA) Instruments DSC Q1000 was used to measure the various thermal transitions of the materials. Dynamic Mechanical Analysis (DMA) on a TA Q800-DMA with a tension film clamp was used to measure the mechanical properties of the materials as well as to make dimension measurements below 0.1 mm, and Mitutoyo digital calipers were used to measure dimensions above 0.1 mm. In situ UV irradiation was carried out with a Dymax Blue Wave 200 with a Thorlabs, Inc. FGUV W53199 UV filter. Finally, UV light intensity was measured with a Dymax ACCU-CAL 50 radiometer.

5.2. Material Design

The LCP described in Chapters 3 and 4 is important in that it shows significant and rapid photo-responsive behavior around room temperature, and it can be used to understand the switching behavior of the photo-induced nematic to isotropic transition at a fundamental level. Still, it is not sufficient, in and of itself, as a photo-responsive material under most circumstances because it is a very viscous liquid with very little mechanical integrity and because it is not elastomeric, which would be needed for an actuator.

To solve these two problems, PS end blocks were added to the LCP to produce a new photo-responsive liquid crystal triblock copolymer (LC-TBCP). The synthesis of the precursor PS-PVMS-PS TBCP was non-trivial and is described in Section 2.4. PS was chosen because the PS blocks would sufficiently segregate from the LC-PVMS block, and the T_g of PS is around 100°C allowing the PS blocks to act as the physical crosslinks in the resulting elastomeric material. Furthermore, LC-BCP's of PS-PVMS have been synthesized previously.[40, 41, 45, 46] In addition, the specific MW's of each block were chosen such that, once the LC was added to the PVMS, the resulting LC-TBCP would form a morphology with PS spheres in an LC-PVMS matrix. Again, these spheres can act as physical crosslinks to make the material a thermoplastic elastomer, which is also an advantage over conventional chemically crosslinked photo-responsive elastomers because it can be melted or dissolved and then reformed into different shapes.

Still, the LC-TBCP described above, even if it is an elastomer, is not quite enough to make an actuator. Once the material is synthesized, it is necessary to align the LC domains, and this can be achieved by simply stretching a heated strip of the material. As alluded to in Section 3.3, the LC's tend to line up in a nematic phase, which not only reduces the free volume but also stretches the polymer backbone from its unfunctionalized equilibrium confirmation, as shown in the first schematic in Figure 5-1. When the nematic LC phase is irradiated with UV light, it disorders, which allows the polymer to contract back to its original conformation, as shown in the second image in Figure 5-1. If the director of the nematic domains is random, then the material will merely expand a little in all directions upon irradiation with UV light because each polymer is contracting in a different direction and the overall system is gaining a little free volume. However, if the nematic domains are aligned, all the polymers will contract in the same

direction resulting in a macroscopic contraction of the material in one direction and compensatory expansion in the other two. This constitutes a photo-actuator.

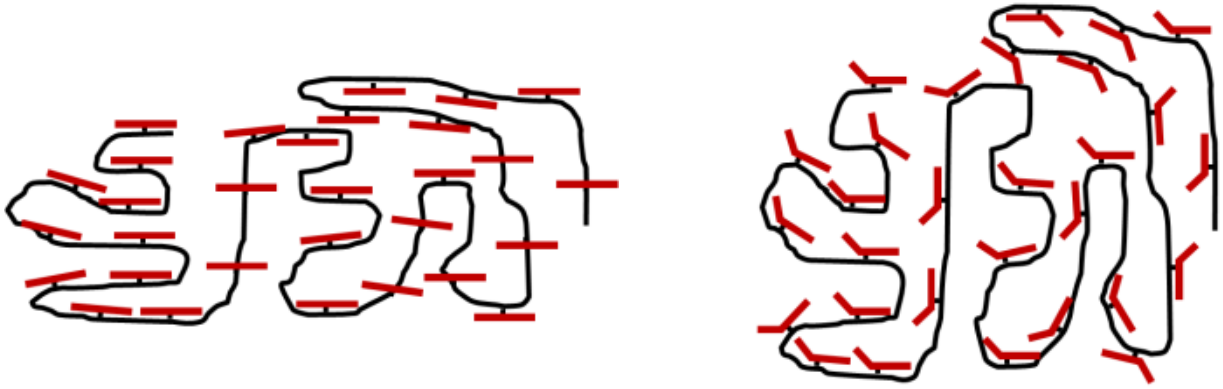

Figure 5-1. Schematic of an LC domain that stretches the polymer backbone and contraction of that backbone in response to UV light due to disruption of the LC phase.

5.3. PS-PVMS-PS TBCP Characterization

First, the PS-PVMS-PS TBCP itself was characterized. A very thin sample was spin coated from toluene onto a TEM grid with a holey carbon support film and then vacuum annealed at 120°C for two hours. The TEM images attained from this sample, with dark PVMS and light PS, are in Figure 5-2 and show that the TBCP has a lamellar morphology. To confirm and measure these lamellae, a thick sample was solvent cast from toluene and then annealed at 120°C for two hours to produce a clear brittle film for SAXS. The TBCP in this film again formed a lamellar phase with a characteristic spacing of 27.5 nm as shown by the large peak and its second and third reflections in the SAXS diffractogram in Figure 5-3.

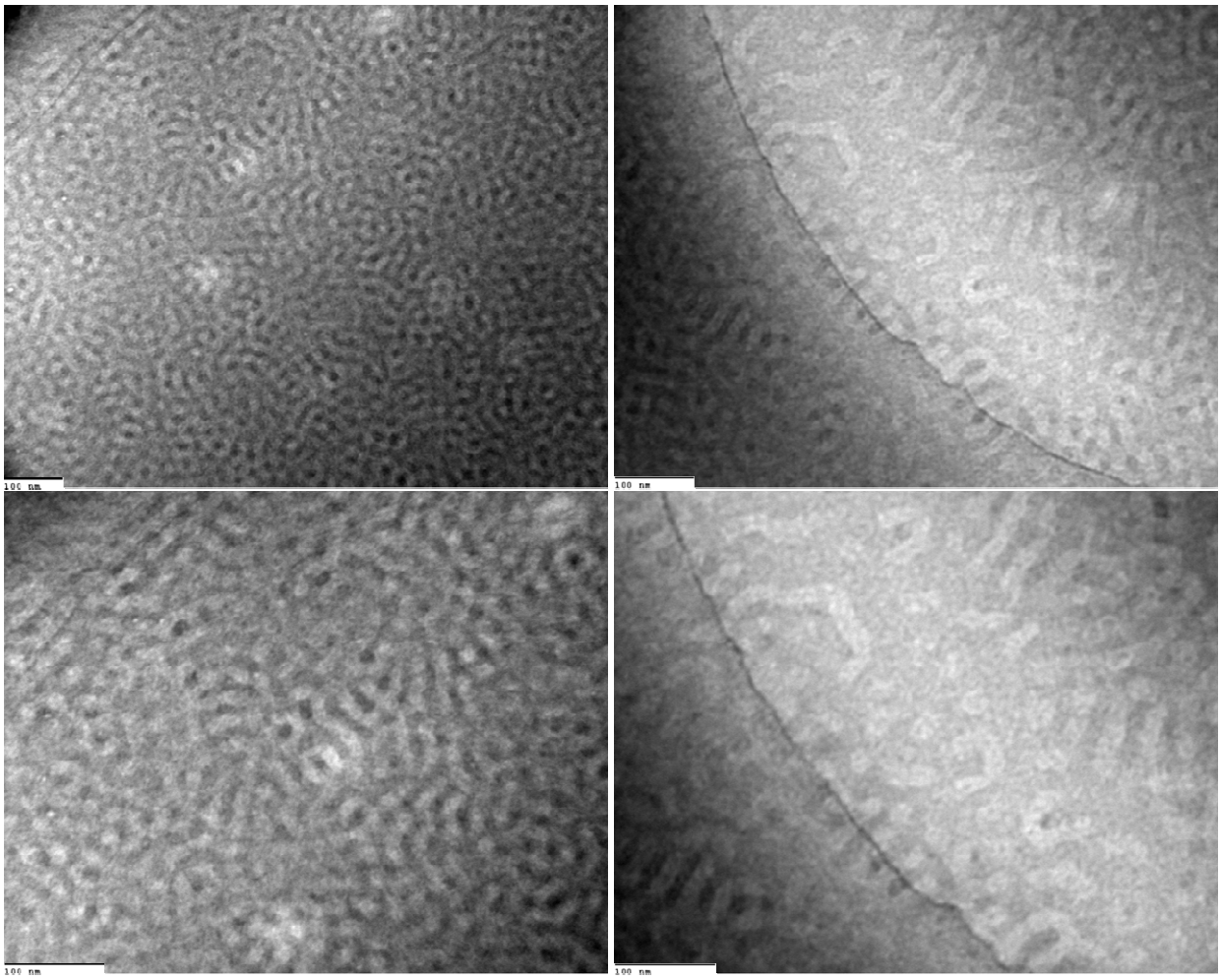

Figure 5-2. TEM images of the PS-PVMS-PS TBCP lamellar morphology. The dark regions are PVMS, and the light regions are PS. Also, the 100 nm scale is marked, and the large curved lines are the edge of the carbon support.

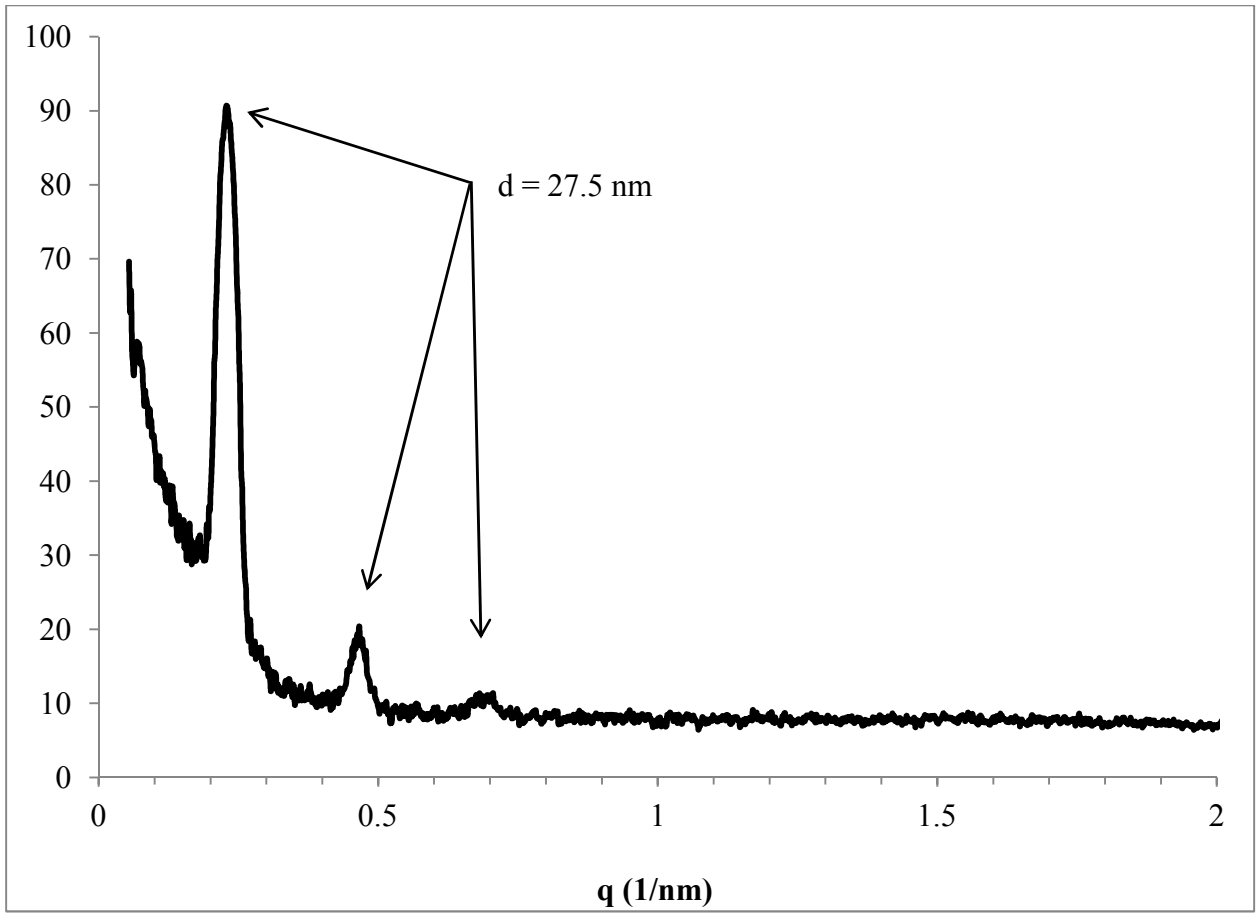

Figure 5-3. Small Angle X-ray Scattering (SAXS) diffactorgram of PS-PVMS-PS TBCP. The large first peak corresponds to the 27.5 nm lamellar spacing, and the other marked peaks are 2nd and 3rd reflections.

Also observable in the PS-PVMS-PS, during both heating and cooling, is the T_g of PS at 96°C, as shown by the inflection in the DSC trace in Figure 5-4. Figure 5-4 also shows a small peak during cooling at -11°C, which is probably due to crystallization of the PVMS.[129] On the other hand, it does not show the T_g of PVMS because it, as with that for most polysiloxanes, is around -100°C.[129]

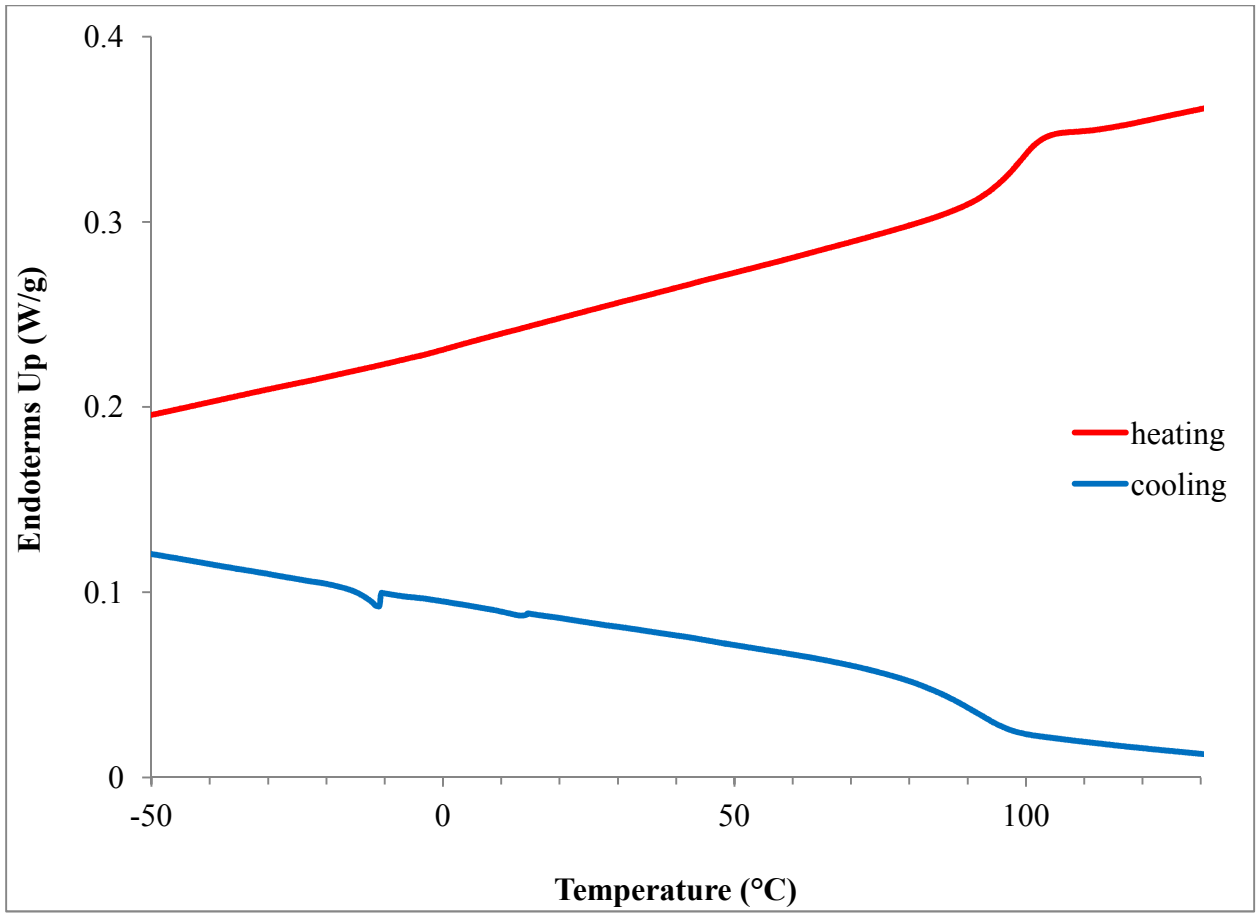

Figure 5-4. Differential Scanning Calorimetry (DSC) at 10°C/min of PS-PVMS-PS. The cooling cycle has been shifted up 0.3 W/g for viewing convenience.

The mechanical properties of the PS-PVMS-PS TBCP follow the observations in the thermal characterization. The Storage Young's Modulus (E') and the tangent of the phase angle (tan δ) from the DMA are shown in Figure 5-5. The condition of 10 Hz corresponds to the OSR characterization of the LCP in Chapter 4, and the strain amplitude is close to that determined to be within the LVE strain regime of the LCP in Section 4.3. In Figure 5-5 at low temperatures, E' starts at 406 MPa, which is an order of magnitude lower than that for glassy PS,[129] because, although it is above the T_g of PS, it is below the T_g of PVMS. Then E' sharply decreases as it passes through the T_g of PS,[129] from around 87°C to 112°C. In addition, this transition to a

rubbery material is seen in the peak in tan δ, also around 102°C, in Figure 5-5. Finally, continued heating after the T_g of PS results in irreversible stretching until it completely yields.

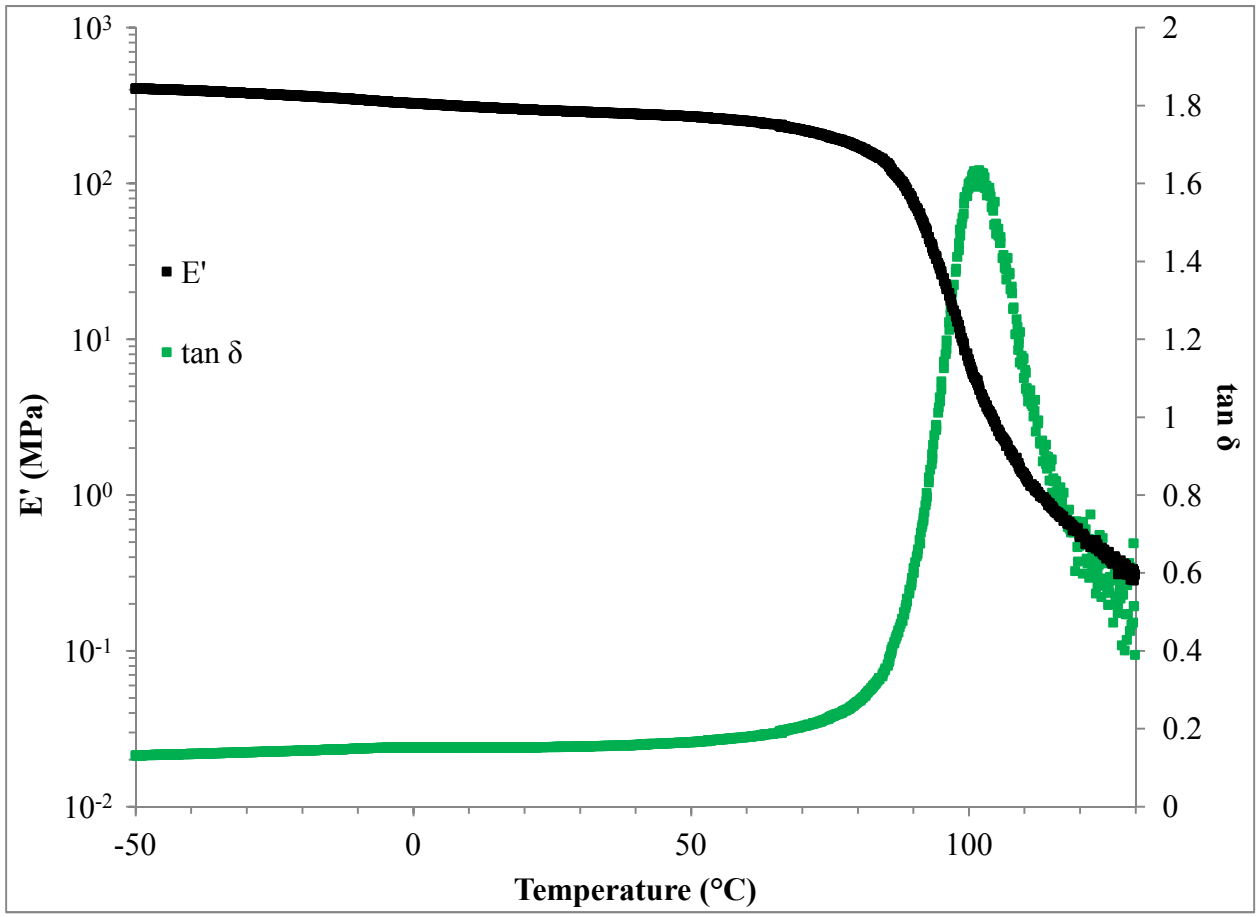

Figure 5-5. Dynamic Mechanical Analysis (DMA) at 3 °C/min, 10 Hz, and 0.1% strain amplitude of a 18.7x8.8x0.6 mm annealed strip of TBCP.

5.4. Liquid Crystal Triblock Copolymer Characterization

After production of the PS-PVMS-PS TBCP, a new batch of the LC (same as that for the LCP) was attached to produce the LC-TBCP. Again, a very thin sample was spin coated from toluene onto a TEM grid with a holey carbon support film and then vacuum annealed at 120°C for two hours. The TEM images attained from this sample, with dark LC-PVMS and light PS,

are in Figure 5-6 and show that the LC-TBCP has a spherical morphology. Even though, the PS-PVMS-PS TBCP was lamellar, the addition of the LC to the PVMS swelled it in relation the PS to produce a morphology with spheres of PS in matrix of LC-PVMS. However, beyond that, these spherical PS domains do not appear to occupy any discernible lattice. Furthermore, again to confirm and measure the spacing of these spheres, a thick sample was solvent cast from toluene and then annealed at 120°C for two hours to produce a brown rubbery film for SAXS. The SAXS diffractogram for this film, shown in Figure 5-7, measures the characteristic spacing between the spherical domains as 40.6 nm, plus there are no discernible reflections of an ordered lattice.

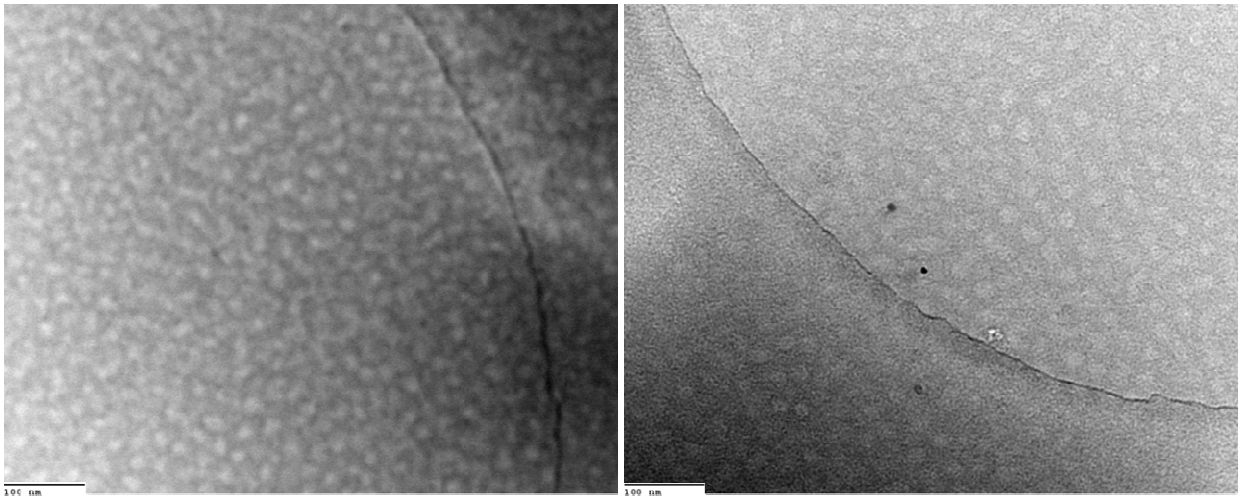

Figure 5-6. Transmission Electron Microscopy (TEM) images of the LC-TBCP spherical morphology. The dark regions are LC-PVMS, and the light regions are PS. Also, the 100 nm scale is marked, and the large curved lines are the edge of the carbon support.

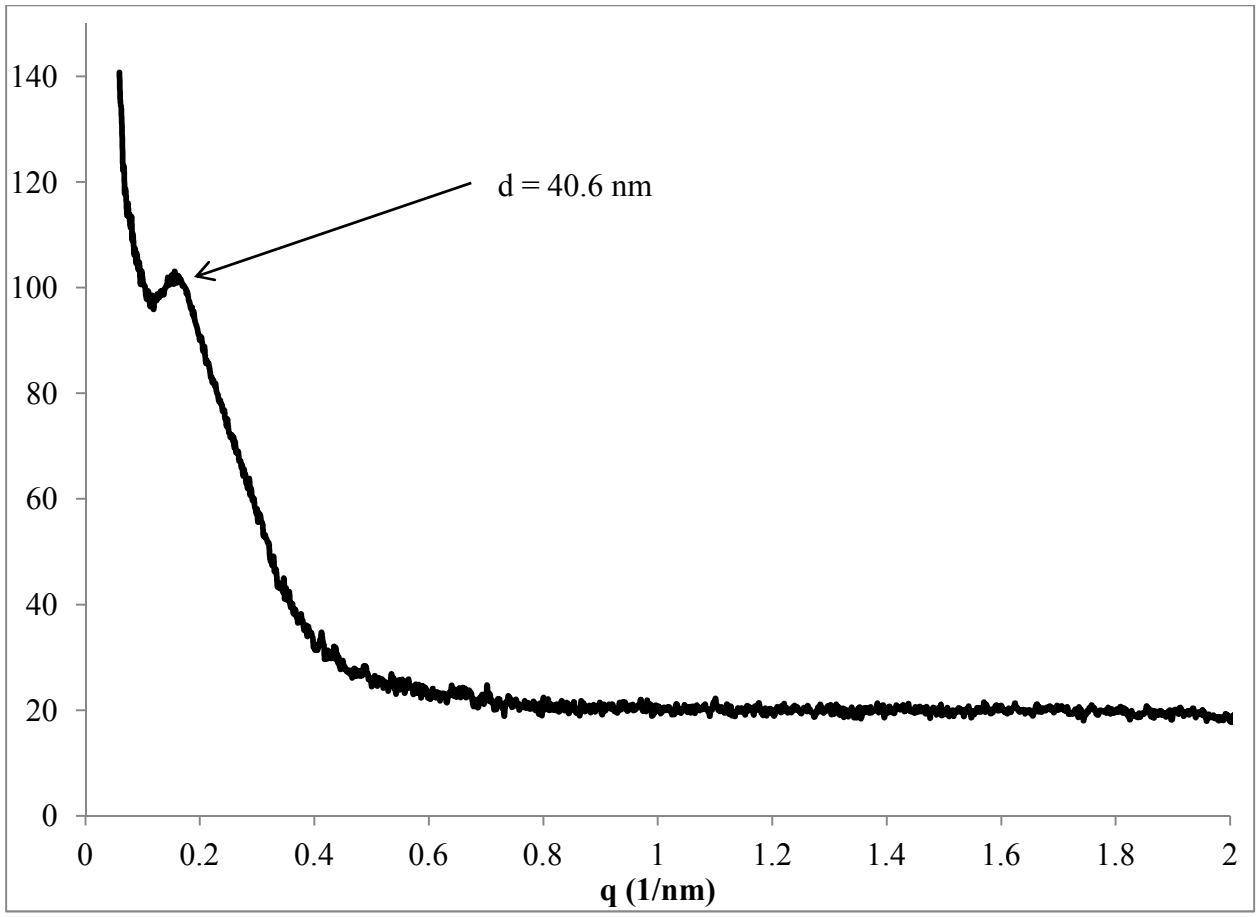

Figure 5-7. Small Angle X-ray Scattering (SAXS) diffactorgram of the LC-BCP. The large peak corresponds to the 40.6 nm spherical spacing.

As for the thermal transitions, shown in the DSC trace in Figure 5-8, they appear to be similar to those of the TBCP but with some extra features. There is no PVMS crystallization, but there is a strong inflection during both heating and cooling at 15°C, corresponding to the T_g of the PVMS backbone, and this T_g is 22°C higher than that of the original LCP. Also, at 100°C, there is a peak, not just an inflection, during both heating and cooling, corresponding to the T_{iso} of the LC, as shown by the loss of birefringence in Figure 5-9. Figure 5-9a shows a bright yellow Schlieren texture, similar to that for the LCP in Figure 3-5, due to the birefringent nematic phase,

and Figure 5-9b is almost completely black, due to the loss of birefringence in the isotropic phase.

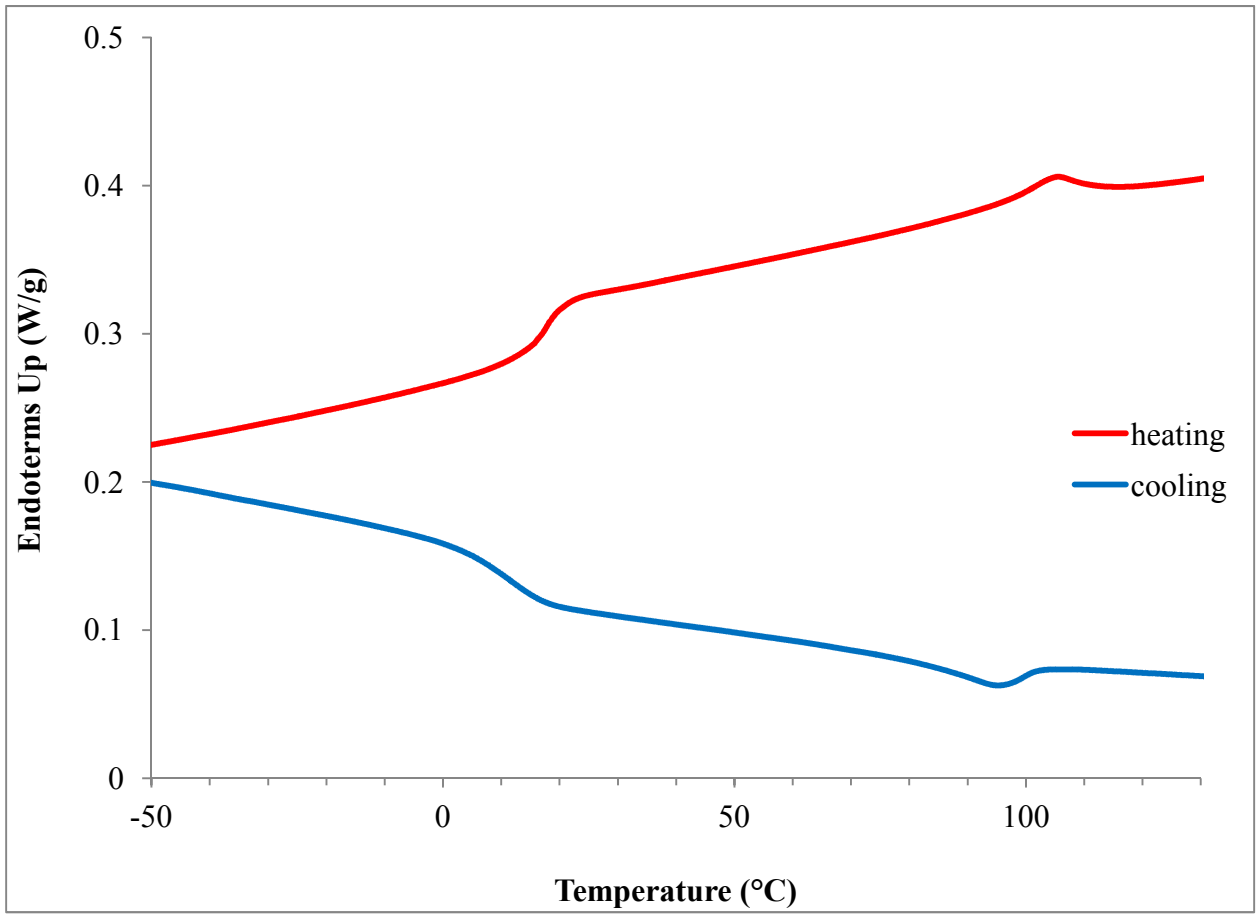

Figure 5-8. Differential Scanning Calorimetry (DSC) at 10°C/min of LC-TBCP. The cooling cycle has been shifted up 0.35 W/g for viewing convenience.

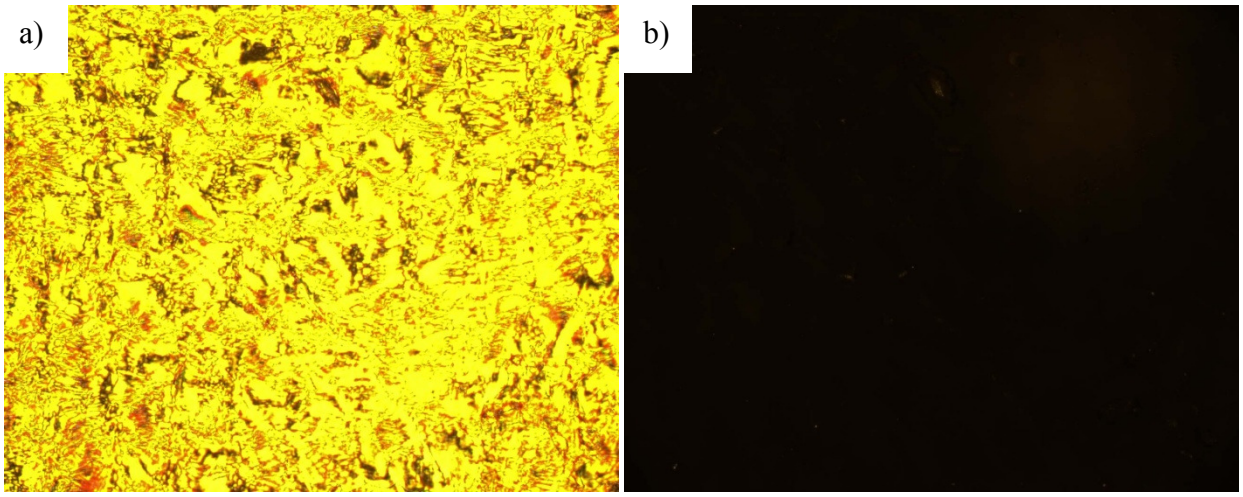

Figure 5-9. Polarized Optical Microscopy (POM) images of the LC-TBCP at a magnification of x10 at a) 100°C and b) 120°C.

Again, the mechanical properties of the LC-TBCP relate to its thermal properties. Figure 5-10 shows E' and tan δ as functions of temperature as measured by DMA at 10 Hz and 0.1% strain, corresponding to the conditions in Sections 4.3 and 5.3. E' starts with a glassy value of 640 MPa at low temperatures and then slowly decreases until it passes through the PVMS backbone's T_g and begins to decrease rapidly around 23°C. Above the T_g of the backbone, it continues to decrease, though at a slower rate, rather than level at a rubbery plateau, because the nematic LC is losing order with increased temperature. Once it reaches its T_{iso}, around 109°C, and the LC-PVMS is completely isotropic, then E' reaches a true rubbery plateau. At this point, unlike the TBCP, the LC-TBCP never yielded because, although this range was above the T_g of PS, it was below the T_{ODT},[46] so the spherical morphology remained as soft physical crosslinks. Even though they are soft, they are stiffer than the very soft isotropic LC-PVMS, which reversibly accommodates the strain of the DMA. Still further, these two features, the T_g of the PVMS backbone and the T_{iso} of the LC, can be easily seen in the underlying peaks tan δ as well.

Finally, it is worth noting that the scatter in the data increases with temperature, especially toward the end of the temperature range because the LC-TBCP is so soft that it is approaching the stiffness resolution limit of the instrument.

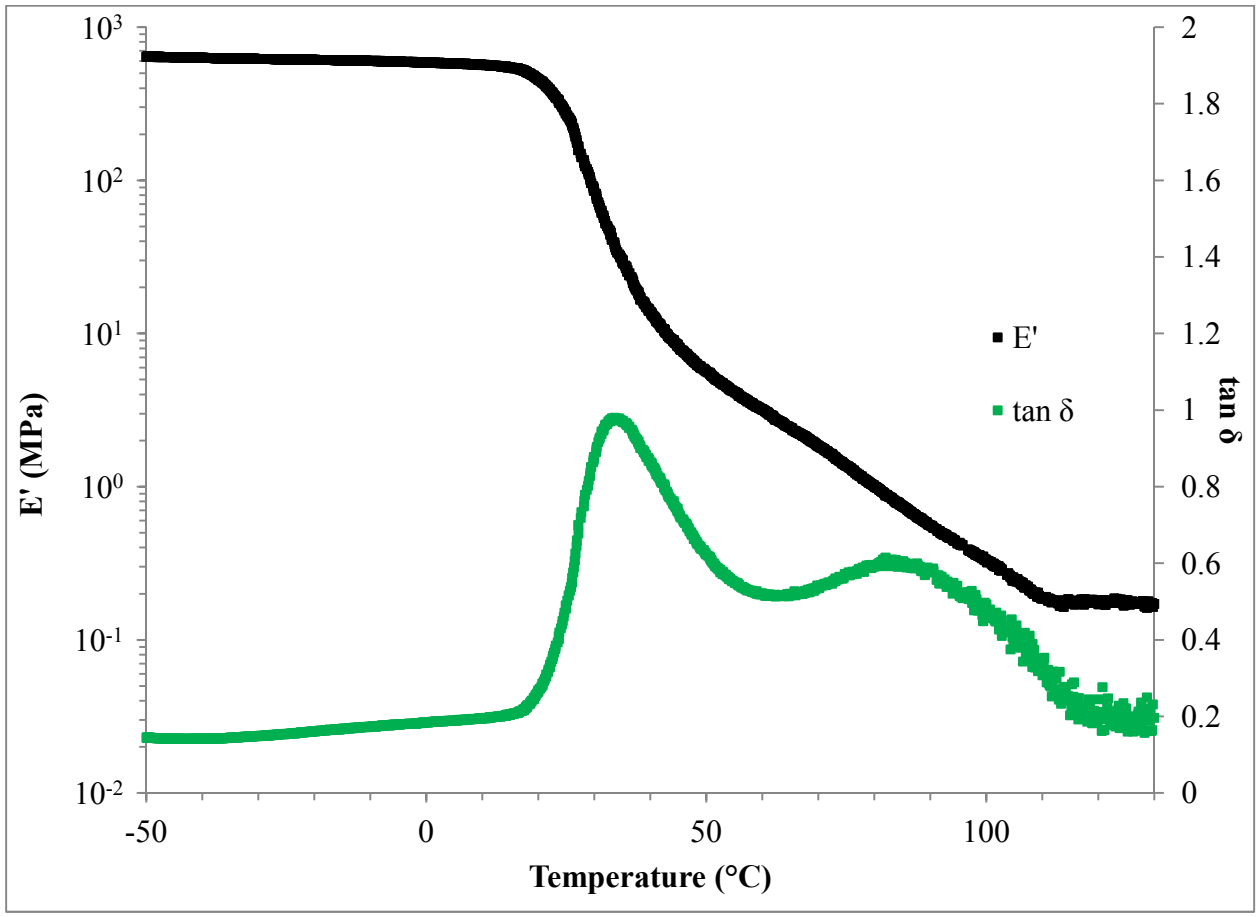

Figure 5-10. Dynamic Mechanical Analysis (DMA) at 3 °C/min, 10 Hz, and 0.1% strain amplitude of a 10.8x7.6x1.7 mm annealed strip of LC-TBCP.

5.5. Photo-responsive Thermoplastic Elastomer Actuation

The final and most important test of the LC-TBCP is to show that it is, in fact, an elastomer that actuates in response to UV light. To do so, a thin film was again cast from toluene and annealed at 120°C, and then it was cut into a thin strip, heated, manually stretched, and

cooled to align the LC. This strip was loaded onto the open DMA and held with 11 mN of tension, and the UV light was placed about 5 cm away from the sample. Under this 11 mN of tension, the UV light was successively turned on and off, and the length of the LC-TBCP strip was monitored and then translated into the extension ratio (λ) of the strip. Figure 5-11, which plots λ as a function of time, shows that, upon UV irradiation, the strip does reversibly contract by about 3.3% in a matter of seconds. The UV cycles were fit with lag time (τ_{lag}) and another stretched exponential (Equations 4-5 and 4-6) and averaged to produce values of 3.9 s, 2.1 s, 1.14, 2.0 s for τ_{lag}, τ, n, and τ_{avg}, respectively, and these results signify a fast switching time of about 6 s. As for the expansion when the UV light is turned off, it takes about 2 s to reach the original length, which is too fast to model the kinetics with the data in Figure 5-11.

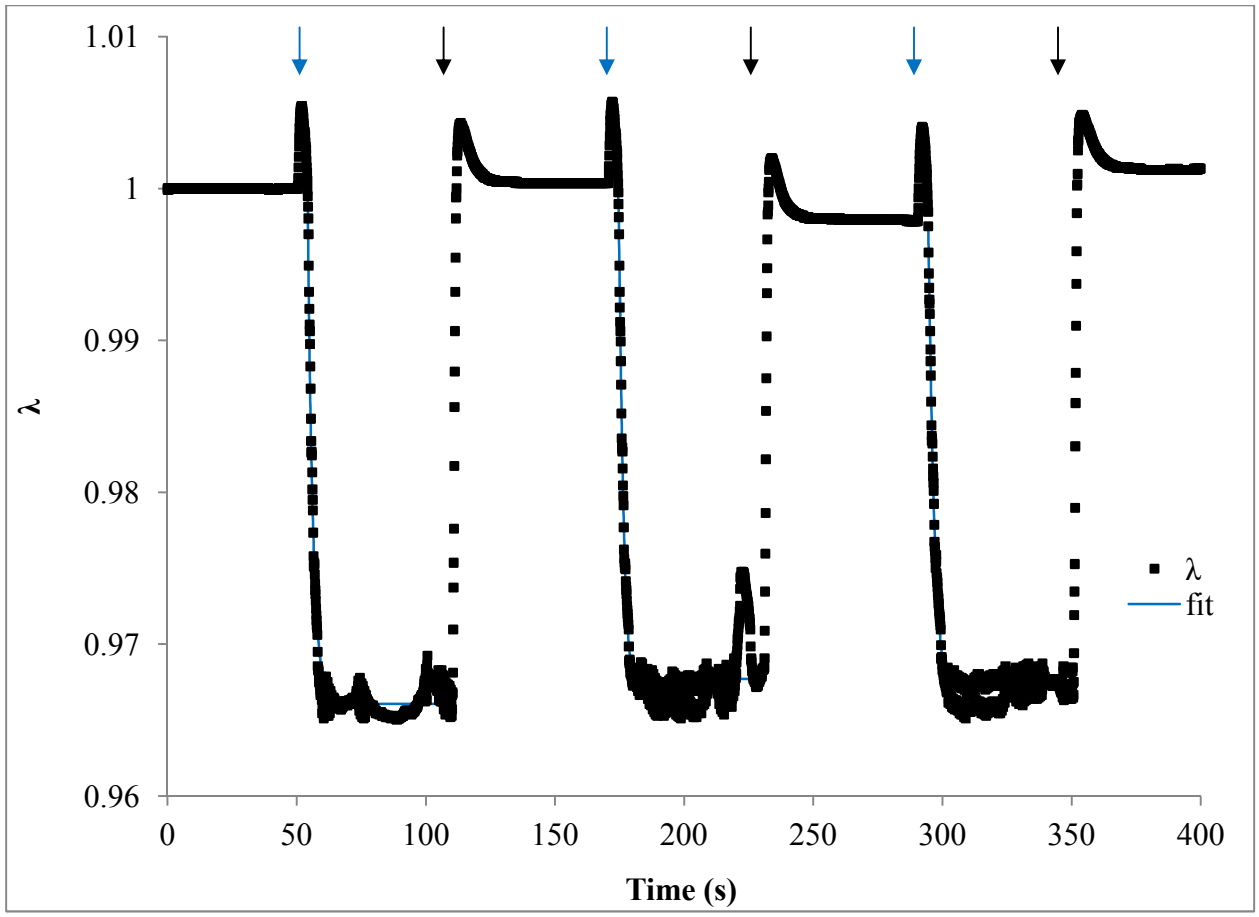

Figure 5-11. UV contraction of a stretched 11.6x6.8x0.0629 mm strip of LC-TBCP against a 11 mN force supplied by the DMA instrument. Blue arrows indicate times when the UV light was switched on, and black arrows indicate times when the UV light was switched off. The UV on switches were fit with lag time followed by a stretched exponential producing average τ_{lag}, τ, n, τ_{avg} , and contraction percent values of 3.9 s, 2.1 s, 1.14, 2.0 s, and 3.3%, respecitively.

Along with the contractions and relaxations in Figure 5-11, there are a few artifacts in the UV switching. The first is the scatter in λ, corresponding to the DMA's length measurement, when the UV light is on and the strip is contracted, and this is due to rippling to accommodate the film's contraction, as shown in Figure 5-12. The second is the initial increase in λ when the UV light is turned and the overshoot in λ when the UV light is turned off, and this is due to

softening of the material under irradiation. The aligned LC-TBCP contracts upon UV irradiation because the LC's nematic phase stretches the polymer backbone, and the UV light disrupts the LC's nematic phase allowing the polymer to contract back to its equilibrium conformation. Concurrent with this nematic to isotropic transition is a decrease in modulus, and in this case, because the LC-TBCP is under 11 mN of tension, it stretches a little before it contracts, when the UV light is turned on, and its extension overshoots its original λ before it again reaches its steady state. The last and most interesting point to make is that the material is actually contracting against an applied 11 mN of tension, which corresponds to 25.7 kPa of stress. Most other materials either show mechanical contraction or developed contractional stress, but few show both, as this does, which will be necessary for its future use an actuator.

Figure 5-12. Picture of LC-TBCP after use in photo-contraction experiments.

6. Conclusion

6.1. Summary of Thesis Contributions

The work described in this thesis serves to advance the fields of photo-responsive LCP's, photo-actuation, anionic synthesis of functional block copolymers, and functional thermoplastic elastomers. The first contribution was the synthesis of a new photo-responsive SCLCP, which has a low T_g backbone and a low T_{iso} LC to address the need for a rapid bulk photo-response at room temperature. The second contribution was the full characterization of this new LCP, its physical and rheological properties, and, in particular, a thorough characterization of its photo-induced nematic to isotropic transition. The third contribution is the synthesis of the PS-PVMS-PS TBCP, which is important because the PVMS has a very low T_g and a functionalizable backbone and the PS end blocks make the material a thermoplastic elastomer. The final contribution is the production of a photo-responsive LC-TBCP thermoplastic elastomer actuator, which rapidly and reversibly contracts at room temperature upon UV irradiation.

6.2. Suggested Future Work

When it comes to transitioning the materials produced and studied in this thesis as well as in the field of photo-actuators, there are still some major hurdles to overcome for them to become useful materials. The work in this thesis outlines the development of a rapid room temperature photo-actuator, but there is much room for improvement by optimizing it for the best MW's and attachment percents as well as the addition of another smectic LC to produce larger and potentially faster photo-responses and more robust materials. From a more general perspective, an external UV light is an impractical and energetically inefficient means to deliver UV light to a photo-responsive material, so the field at large could benefit from a better

engineered delivery system. Tangentially, the field itself should and is looking for alternative triggers to actuation to improve both the practicality and the utility of elastomeric actuators. In particular, a chemical vapor triggered isotropic to LC transition could be useful for protection against that chemical vapor.

6.3. References

1. Chandrasekhar, S., *Liquid crystals*. 2nd ed.; Cambridge University Press: Cambridge [England] ; New York, NY, USA, 1992; p xv, 460 p.

2. Collings, P. J., *Liquid crystals : nature's delicate phase of matter*. Princeton University Press: Princeton, N.J., 1990; p xiii, 222 p., [8] p. of plates.

3. Collings, P. J.; Hird, M., *Introduction to liquid crystals : chemistry and physics*. Taylor & Francis: London ; Bristol, PA, 1997; p xi, 298 p.

4. Gennes, P.-G. d.; Prost, J., *The physics of liquid crystals*. 2nd ed.; Clarendon Press ; Oxford University Press: Oxford
New York, 1995; p xvi, 597 p.

5. Gray, G. W., *Molecular structure and the properties of liquid crystals*. Academic Press: London, New York,, 1962; p 314 p.

6. Gray, G. W.; Society of Chemical Industry (Great Britain), *Thermotropic liquid crystals*. Published on behalf of the Society of Chemical Industry by Wiley: Chichester [East Sussex] ; New York, 1987; p xii, 178 p.

7. Gray, G. W.; Winsor, P. A., *Liquid crystals & plastic crystals*. E. Horwood; Halsted Press: Chichester [Eng.]
New York,, 1974; p 2 v.

8. Collings, P. J., *Liquid crystals : nature's delicate phase of matter*. Princeton University Press: Princeton, N.J., 1990; p xiii, 222 p., [8] p. of plates.

9. Dierking, I., *Textures of liquid crystals*. Wiley-VCH: Weinheim, 2003; p xi, 218 p.

10. Robinson, P.; Davidson, M., *Nikon Microscopy U* **2000-2010**.

11. Bates, F. S.; Fredrickson, G. H., *Annual Review of Physical Chemistry* **1990,** *41*, 525-557.

12. Hadjichristidis, N.; Pispas, S.; Floudas, G., *Block copolymers : synthetic strategies, physical properties, and applications*. Wiley-Interscience: Hoboken, N.J., 2003; p xx, 419 p.

13. Matsen, M. W.; Bates, F. S., *Macromolecules* **1996,** *29* (23), 7641-7644.

14. Odian, G. G., *Principles of polymerization*. 4th ed.; Wiley-Interscience: Hoboken, N.J., 2004; p xxiv, 812 p.

15. Bezou, P.; Pacreau, A.; Vairon, J. P.; Lacoudre, N.; Friedrich, C.; Noel, C., *Polymers for Advanced Technologies* **1997,** *8* (2), 63-74.

16. Percec, V.; Zheng, Q., *Journal of Materials Chemistry* **1992,** *2* (10), 1041-1047.

17. Zhu, Z. G.; Zhi, J. G.; Liu, A. H.; Cui, J. X.; Tang, H.; Qiao, W. Q.; Wan, X. H.; Zhou, Q. F., *Journal of Polymer Science Part a-Polymer Chemistry* **2007,** *45* (5), 830-847.

18. Anthamatten, M.; Wu, J. S.; Hammond, P. T., *Macromolecules* **2001,** *34* (24), 8574-8579.

19. Anthamatten, M.; Zheng, W. Y.; Hammond, P. T., *Macromolecules* **1999,** *32* (15), 4838-4848.

20. Itoh, T.; Yamada, M.; Hirao, A.; Nakahama, S. I.; Watanabe, J., *Molecular Crystals and Liquid Crystals* **2000,** *347*, 455-464.

21. Yu, H. F.; Okano, K.; Shishido, A.; Ikeda, T.; Kamata, K.; Komura, M.; Iyoda, T., *Advanced Materials* **2005,** *17* (18), 2184-2188.

22. Mao, G. P.; Wang, J. G.; Clingman, S. R.; Ober, C. K.; Chen, J. T.; Thomas, E. L., *Macromolecules* **1997,** *30* (9), 2556-2567.

23. Ahn, S. K.; Deshmukh, P.; Kasi, R. M., *Macromolecules* **2010,** *43* (17), 7330-7340.

24. Gabert, A. J.; Verploegen, E.; Hammond, P. T.; Schrock, R. R., *Abstracts of Papers of the American Chemical Society* **2006,** *231*, -.

25. Noirez, L.; Ungerank, M.; Stelzer, F., *Macromolecules* **2001,** *34* (22), 7885-7893.

26. Donnio, B.; Buathong, S.; Bury, I.; Guillon, D., *Chemical Society Reviews* **2007,** *36* (9), 1495-1513.

27. Clarke, S. M.; Terentjev, E. M., *Physical Review Letters* **1998,** *81* (20), 4436-4439.

28. Clarke, S. M.; Terentjev, E. M.; Kundler, I.; Finkelmann, H., *Macromolecules* **1998,** *31* (15), 4862-4872.

29. Donnio, B.; Wermter, H.; Finkelmann, H., *Macromolecules* **2000,** *33* (21), 7724-7729.

30. Finkelmann, H.; Garcia-Amoros, J.; Velasco, D., *Journal of Materials Chemistry* **2011,** *21* (4), 1094-1101.

31. Finkelmann, H.; Kock, H. J.; Rehage, G., *Makromolekulare Chemie-Rapid Communications* **1981,** *2* (4), 317-322.

32. Finkelmann, H.; Komp, A., *Macromolecular Rapid Communications* **2007,** *28* (1), 55-62.

33. Finkelmann, H.; Nishikawa, E.; Pereira, G. G.; Warner, M., *Physical Review Letters* **2001,** *8701* (1), -.

34. Finkelmann, H.; Rehage, G., *Makromolekulare Chemie-Rapid Communications* **1980,** *1* (1), 31-34.

35. Gallot, B.; Galli, G.; Ceccanti, A.; Chiellini, E., *Polymer* **1999,** *40* (10), 2561-2568.

36. Gleim, W.; Finkelmann, H., *Makromolekulare Chemie-Macromolecular Chemistry and Physics* **1987,** *188* (6), 1489-1500.

37. Jiang, T. Y.; Zhang, B. Y.; Tian, M.; Wang, Y., *Journal of Applied Polymer Science* **2003,** *89* (10), 2845-2851.

38. Meng, F. B.; Cui, Y.; Chen, H. B.; Zhang, B. Y.; Jia, C., *Polymer* **2009,** *50* (5), 1187-1196.

39. Merekalov, A. S.; Finkelmann, H., *Macromolecular Chemistry and Physics* **1996,** *197* (7), 2325-2330.

40. Moment, A.; Hammond, P. T., *Polymer* **2001,** *42* (16), 6945-6959.

41. Moment, A.; Miranda, R.; Hammond, P. T., *Macromolecular Rapid Communications* **1998,** *19* (11), 573-579.

42. Sanchez-Ferrer, A.; Finkelmann, H., *Molecular Crystals and Liquid Crystals* **2009,** *508*, 357-366.

43. Sanchez-Ferrer, A.; Finkelmann, H., *Macromolecular Rapid Communications* **2011,** *32* (3), 309-315.

44. Tajbakhsh, A. R.; Terentjev, E. M., *European Physical Journal E* **2001,** *6* (2), 181-188.

45. Verploegen, E.; Tian, L.; McAfee, L. C.; Verploegen, D.; Hammond, P. T., *Abstracts of Papers of the American Chemical Society* **2006,** *231*, -.

46. Verploegen, E.; Zhang, T.; Murlo, N.; Hammond, P. T., *Soft Matter* **2008,** *4* (6), 1279-1287.

47. Zentel, R.; Ohm, C.; Brehmer, M., *Advanced Materials* **2010,** *22* (31), 3366-3387.

48. Zhang, S. J.; Terentjev, E. M.; Donald, A. M., *Macromolecules* **2004,** *37* (2), 390-396.

49. Rousseau, I. A.; Mather, P. T., *Journal of the American Chemical Society* **2003,** *125* (50), 15300-15301.

50. Verploegen, E.; Boone, D.; Hammond, P. T., *Journal of Polymer Science Part B-Polymer Physics* **2007,** *45* (24), 3263-3266.

51. Verploegen, E.; McAfee, L. C.; Tian, L.; Verploegen, D.; Hammond, P. T., *Abstracts of Papers of the American Chemical Society* **2005,** *230*, U3673-U3673.

52. Li, M. H.; Auroy, P.; Keller, P., *Liquid Crystals* **2000,** *27* (11), 1497-1502.

53. Li, M. H.; Keller, P., *Philosophical Transactions of the Royal Society a-Mathematical Physical and Engineering Sciences* **2006,** *364* (1847), 2763-2777.

54. Li, M. H.; Keller, P.; Li, B.; Wang, X. G.; Brunet, M., *Advanced Materials* **2003,** *15* (7-8), 569-572.

55. Naciri, J.; Srinivasan, A.; Jeon, H.; Nikolov, N.; Keller, P.; Ratna, B. R., *Macromolecules* **2003,** *36* (22), 8499-8505.

56. Chang, S.; Han, C. D., *Macromolecules* **1996,** *29* (6), 2103-2112.

57. Burke, K. A.; Mather, P. T., *Journal of Materials Chemistry* **2010,** *20* (17), 3449-3457.

58. Buguin, A.; Li, M. H.; Silberzan, P.; Ladoux, B.; Keller, P., *Journal of the American Chemical Society* **2006,** *128* (4), 1088-1089.

59. Cotton, J. P.; Hardouin, F., *Progress in Polymer Science* **1997,** *22* (4), 795-828.

60. Barrett, C. J.; Mamiya, J. I.; Yager, K. G.; Ikeda, T., *Soft Matter* **2007,** *3* (10), 1249-1261.

61. Cviklinski, J.; Tajbakhsh, A. R.; Terentjev, E. M., *European Physical Journal E* **2002,** *9* (5), 427-434.

62. Garcia-Amoros, J.; Finkelmann, H.; Velasco, D., *Chemistry-a European Journal* **2011,** *17* (23), 6518-6523.

63. Harris, K. D.; Cuypers, R.; Scheibe, P.; van Oosten, C. L.; Bastiaansen, C. W. M.; Lub, J.; Broer, D. J., *Journal of Materials Chemistry* **2005,** *15* (47), 5043-5048.

64. Hogan, P. M.; Tajbakhsh, A. R.; Terentjev, E. M., *Physical Review E* **2002,** *65* (4).

65. Hrozhyk, U.; Serak, S.; Tabiryan, N.; White, T. J.; Bunning, T. J., *Optics Express* **2009,** *17* (2), 716-722.

66. Ikeda, T.; Kondo, M.; Mamiya, J.; Kinoshita, M.; Yu, Y. L., *Molecular Crystals and Liquid Crystals* **2007,** *478*, 1001-1013.

67. Ikeda, T.; Okano, K.; Shishido, A., *Advanced Materials* **2006,** *18* (4), 523-+.

68. Ikeda, T.; Okano, K.; Shishido, A., *Molecular Crystals and Liquid Crystals* **2007,** *478*, 1015-1025.

69. Ikeda, T.; Shimamura, A.; Hiraoka, T.; Kondo, M.; Kubo, S.; Mamiya, J.; Shishido, A., *Molecular Crystals and Liquid Crystals* **2010,** *529*, 53-59.

70. Ikeda, T.; Yamada, M.; Kondo, M.; Miyasato, R.; Mamiya, J.; Kinoshita, M.; Yu, Y. L.; Barrett, C. J., *Molecular Crystals and Liquid Crystals* **2009,** *498*, 65-73.

71. Ikeda, T.; Yamada, M.; Kondo, M.; Miyasato, R.; Naka, Y.; Mamiya, J.; Kinoshita, M.; Shishido, A.; Yu, Y. L.; Barrett, C. J., *Journal of Materials Chemistry* **2009,** *19* (1), 60-62.

72. Ikeda, T.; Yamada, M.; Okutsu, R.; Mamiya, J.; Kinoshita, M.; Yu, Y. L., *Molecular Crystals and Liquid Crystals* **2007,** *470*, 93-100.

73. Ikeda, T.; Yoshino, T.; Kondo, M.; Mamiya, J.; Kinoshita, M.; Yu, Y. L., *Advanced Materials* **2010,** *22* (12), 1361-+.

74. Ikeda, T.; Yoshino, T.; Mamiya, J.; Kinoshita, M.; Yu, Y. L., *Molecular Crystals and Liquid Crystals* **2007,** *478*, 989-999.

75. Ikeda, T.; Yu, Y. L.; Maeda, T.; Mamiya, J., *Angewandte Chemie-International Edition* **2007,** *46* (6), 881-883.

76. Lee, K. M.; Koerner, H.; Vaia, R. A.; Bunning, T. J.; White, T. J., *Macromolecules* **2010,** *43* (19), 8185-8190.

77. Matejka, L.; Ilavsky, M.; Dusek, K.; Wichterle, O., *Polymer* **1981,** *22* (11), 1511-1515.

78. Orsi, D.; Cristofolini, L.; Fontana, M. P.; Pontecorvo, E.; Caronna, C.; Fluerasu, A.; Zontone, F.; Madsen, A., *Physical Review E* **2010,** *82* (3).

79. Sanchez-Ferrer, A.; Merekalov, A.; Finkelmann, H., *Macromolecular Rapid Communications* **2011,** *32* (8), 671-678.

80. Serak, S. V.; Tabiryan, N. V.; White, T. J.; Bunning, T. J., *Optics Express* **2009,** *17* (18), 15736-15746.

81. Tsutsumi, O.; Shiono, T.; Ikeda, T.; Galli, G., *Journal of Physical Chemistry B* **1997,** *101* (8), 1332-1337.

82. Verploegen, E.; Soulages, J.; Kozberg, M.; Zhang, T.; McKinley, G.; Hammond, P., *Angewandte Chemie-International Edition* **2009,** *48* (19), 3494-3498.

83. White, T. J.; Serak, S. V.; Tabiryan, N. V.; Vaia, R. A.; Bunning, T. J., *Journal of Materials Chemistry* **2009,** *19* (8), 1080-1085.

84. White, T. J.; Tabiryan, N. V.; Serak, S. V.; Hrozhyk, U. A.; Tondiglia, V. P.; Koerner, H.; Vaia, R. A.; Bunning, T. J., *Soft Matter* **2008,** *4* (9), 1796-1798.

85. Xu, J. X.; Yu, Y. L.; Yin, R. Y.; Wang, W. R.; Ikeda, T., *Molecular Crystals and Liquid Crystals* **2007,** *470*, 83-91.

86. Yu, H. F.; Ikeda, T., *Advanced Materials* **2011,** *23* (19), 2149-2180.

87. Finkelmann, H.; Nishikawa, E.; Pereira, G. G.; Warner, M., *Physical Review Letters* **2001,** *87* (1).

88. Garcia-Amoros, J.; Finkelmann, H.; Velasco, D., *Journal of Materials Chemistry* **2011,** *21* (4), 1094-1101.

89. Kondo, M.; Mamiya, J.; Kinoshita, M.; Ikeda, T.; Yu, Y. L., *Molecular Crystals and Liquid Crystals* **2007,** *478*, 1001-1013.

90. Mamiya, J. I.; Yoshitake, A.; Kondo, M.; Yu, Y.; Ikeda, T., *Journal of Materials Chemistry* **2008,** *18* (1), 63-65.

91. Naka, Y.; Mamiya, J.; Shishido, A.; Washio, M.; Ikeda, T., *Molecular Crystals and Liquid Crystals* **2010,** *529*, 71-79.

92. Shimamura, A.; Hiraoka, T.; Kondo, M.; Kubo, S.; Mamiya, J.; Shishido, A.; Ikeda, T., *Molecular Crystals and Liquid Crystals* **2010,** *529*, 53-59.

93. Tabiryan, N.; Serak, S.; Dai, X. M.; Bunning, T., *Optics Express* **2005,** *13* (19), 7442-7448.

94. Velasco, D.; Garcia-Amoros, J.; Pinol, A.; Finkelmann, H., *Organic Letters* **2011,** *13* (9), 2282-2285.

95. Warner, M.; Terentjev, E., *Macromolecular Symposia* **2003,** *200*, 81-92.

96. Yamada, M.; Kondo, M.; Mamiya, J. I.; Yu, Y. L.; Kinoshita, M.; Barrett, C. J.; Ikeda, T., *Angewandte Chemie-International Edition* **2008,** *47* (27), 4986-4988.

97. Yamada, M.; Kondo, M.; Miyasato, R.; Mamiya, J.; Kinoshita, M.; Yu, Y. L.; Barrett, C. J.; Ikeda, T., *Molecular Crystals and Liquid Crystals* **2009,** *498*, 65-73.

98. Yamada, M.; Kondo, M.; Miyasato, R.; Naka, Y.; Mamiya, J.; Kinoshita, M.; Shishido, A.; Yu, Y. L.; Barrett, C. J.; Ikeda, T., *Journal of Materials Chemistry* **2009,** *19* (1), 60-62.

99. Yoshino, T.; Kondo, M.; Mamiya, J.; Kinoshita, M.; Yu, Y. L.; Ikeda, T., *Advanced Materials* **2010,** *22* (12), 1361-+.

100. Yu, Y. L.; Maeda, T.; Mamiya, J.; Ikeda, T., *Angewandte Chemie-International Edition* **2007,** *46* (6), 881-883.

101. Yu, Y. L.; Nakano, M.; Ikeda, T., *Nature* **2003,** *425* (6954), 145-145.

102. Bu, H. T.; Kjoniksen, A. L.; Nystrom, B., *Biomacromolecules* **2004,** *5* (2), 610-617.

103. Hosono, N.; Furukawa, H.; Masubuchi, Y.; Watanabe, T.; Horie, K., *Colloids and Surfaces B-Biointerfaces* **2007,** *56* (1-2), 285-289.

104. Hu, J. L.; Meng, H., *Journal of Intelligent Material Systems and Structures* **2010,** *21* (9), 859-885.

105. Hugel, T.; Holland, N. B.; Cattani, A.; Moroder, L.; Seitz, M.; Gaub, H. E., *Science* **2002,** *296* (5570), 1103-1106.

106. Irie, M.; Hirano, Y.; Hashimoto, S.; Hayashi, K., *Macromolecules* **1981,** *14* (2), 262-267.

107. Kumar, G. S.; Depra, P.; Neckers, D. C., *Macromolecules* **1984,** *17* (10), 1912-1917.

108. Lendlein, A.; Jiang, H. Y.; Junger, O.; Langer, R., *Nature* **2005,** *434* (7035), 879-882.

109. Moniruzzaman, M.; Sabey, C. J.; Fernando, G. F., *Macromolecules* **2004,** *37* (7), 2572-2577.

110. Tribet, C.; Pouliquen, G., *Macromolecules* **2006,** *39* (1), 373-383.

111. Lee, C. T.; Smith, K. A.; Hatton, T. A., *Macromolecules* **2004,** *37* (14), 5397-5405.

112. Lemieux, R. P., *Soft Matter* **2005,** *1* (5), 348-354.

113. Tamaoki, N.; Kamei, T., *Journal of Photochemistry and Photobiology C-Photochemistry Reviews* **2010,** *11* (2-3), 47-61.

114. Camacho-Lopez, M.; Finkelmann, H.; Palffy-Muhoray, P.; Shelley, M., *Nature Materials* **2004,** *3* (5), 307-310.

115. Harvey, C. L. M.; Terentjev, E. M., *European Physical Journal E* **2007,** *23* (2), 185-189.

116. Ikeda, T.; Kanazawa, A., *Bulletin of the Chemical Society of Japan* **2000,** *73* (8), 1715-1733.

117. Rochon, P.; Natansohn, A., *Chemical Reviews* **2002,** *102* (11), 4139-4175.

118. Horie, K.; Hirao, K.; Kenmochi, N.; Mita, I., *Makromolekulare Chemie-Rapid Communications* **1988,** *9* (4), 267-273.

119. Yu, H. F.; Kobayashi, T., *Molecules* **2010,** *15* (1), 570-603.

120. Ketner, A. M.; Kumar, R.; Davies, T. S.; Elder, P. W.; Raghavan, S. R., *Journal of the American Chemical Society* **2007,** *129* (6), 1553-1559.

121. Kumar, R.; Ketner, A. M.; Raghavan, S. R., *Langmuir* **2010,** *26* (8), 5405-5411.

122. Rabek, J. F., *Photochemistry and photophysics*. CRC Press: Boca Raton, Fla., 1990; p v. <1-2, 6 >.

123. Bronnikov, S.; Cozan, V.; Nasonov, A., *Phase Transitions* **2007,** *80* (8), 831-839.

124. Bronnikov, S.; Dierking, I., *Physica B-Condensed Matter* **2005,** *358* (1-4), 339-347.

125. Bronnikov, S.; Racles, C.; Nasonov, A.; Cazacu, M., *Liquid Crystals* **2006,** *33* (9), 1015-1019.

126. Dierking, I., *Applied Physics a-Materials Science & Processing* **2001,** *72* (3), 307-310.

127. Stukan, M. R.; Ivanov, V. A.; Muller, M.; Paul, W.; Binder, K., *E-Polymers* **2003**.

128. Bellas, V.; Iatrou, H.; Hadjichristidis, N., *Macromolecules* **2000,** *33* (19), 6993-6997.

129. Brandrup, J.; Immergut, E. H.; Grulke, E. A., *Polymer handbook*. 4th ed.; Wiley: New York, 1999; p 1 v. (various pagings).

130. Bobrovsky, A.; Boiko, N.; Shibaev, V.; Stumpe, J., *Liquid Crystals* **2002,** *29* (11), 1469-1476.

131. Choi, D. H.; Kang, S. H.; Lee, J. Y.; Samui, A. B., *Bulletin of the Korean Chemical Society* **1998,** *19* (11), 1179-1184.

132. Eich, M.; Wendorff, J., *Journal of the Optical Society of America B-Optical Physics* **1990,** *7* (8), 1428-1436.

133. Hasegawa, M.; Yamamoto, T.; Kanazawa, A.; Shiono, T.; Ikeda, T.; Nagase, Y.; Akiyama, E.; Takamura, Y., *Journal of Materials Chemistry* **1999,** *9* (11), 2765-2769.

134. Ikeda, T.; Horiuchi, S.; Karanjit, D. B.; Kurihara, S.; Tazuke, S., *Macromolecules* **1990,** *23* (1), 42-48.

135. Ikeda, T.; Kurihara, S.; Karanjit, D. B.; Tazuke, S., *Macromolecules* **1990,** *23* (17), 3938-3943.

136. Ikeda, T.; Lee, H. K.; Doi, K.; Harada, H.; Tsutsumi, O.; Kanazawa, A.; Shiono, T., *Journal of Physical Chemistry B* **2000,** *104* (30), 7023-7028.

137. Ikeda, T.; Tsutsumi, O.; Sasaki, T., *Synthetic Metals* **1996,** *81* (2-3), 289-296.

138. Kato, T.; Hirota, N.; Fujishima, A.; Frechet, J. M. J., *Journal of Polymer Science Part a-Polymer Chemistry* **1996,** *34* (1), 57-62.

139. Kawanishi, Y.; Tamaki, T.; Ichimura, K., *Journal of Physics D-Applied Physics* **1991,** *24* (5), 782-784.

140. Kurihara, S.; Nomiyama, S.; Nonaka, T., *Chemistry of Materials* **2000,** *12* (1), 9-+.

141. Kurihara, S.; Sakamoto, A.; Yoneyama, D.; Nonaka, T., *Macromolecules* **1999,** *32* (20), 6493-6498.

142. Lee, H. K.; Doi, K.; Kanazawa, A.; Shiono, T.; Ikeda, T.; Fujisawa, T.; Aizawa, M.; Lee, B., *Polymer* **2000,** *41* (5), 1757-1763.

143. Nabeshima, Y.; Shishido, A.; Kanazawa, A.; Shiono, T.; Ikeda, T.; Hiyama, T., *Chemistry of Materials* **1997,** *9* (6), 1480-1487.

144. Tsutsumi, O.; Demachi, Y.; Kanazawa, A.; Shiono, T.; Ikeda, T.; Nagase, Y., *Journal of Physical Chemistry B* **1998,** *102* (16), 2869-2874.

145. Mita, I.; Horie, K.; Hirao, K., *Macromolecules* **1989,** *22* (2), 558-563.

146. Sperling, L. H., *Introduction to physical polymer science*. 3rd ed.; Wiley-Interscience: New York, 2001; p xl, 671 p.

147. Ferry, J., *Viscoelastic properties of polymers*. 3d ed.; Wiley: New York, 1980; p xxiv, 641 p.

148. Berghausen, J.; Fuchs, J.; Richtering, W., *Macromolecules* **1997,** *30* (24), 7574-7581.

149. Fourmaux-Demange, V.; Brulet, A.; Boue, F.; Davidson, P.; Keller, P.; Cotton, J. P., *European Physical Journal E* **2000,** *1* (4), 301-317.

150. Pujolle-Robic, C.; Olmsted, P. D.; Noirez, L., *Europhysics Letters* **2002,** *59* (3), 364-369.

151. Liu, X. P.; Hu, S. R.; Shi, L. H.; Xu, M.; Zhou, Q. F.; Duan, X. Q., *Polymer* **1989,** *30* (2), 273-279.

152. Shi, H. Q.; Chen, S. H.; deRosa, M. E.; Bunning, T. J.; Adams, W. W., *Liquid Crystals* **1996,** *20* (3), 277-282.